Impact Ionization In AlGaAsSb Avalanche Photodiodes

Xiao Jin

SEPTEMBER 21, 2022

A THESIS SUBMITTED FOR THE DEGREEE OF DOCTOR OF PHILOSOPHY
Department of Electronic and Electrical Engineering
The University of Sheffield

Contents

Acknowledgements

I would like to thank my supervisor, Professor John P. R. David, who deserves the highest gratitude for his tremendous advice and support. He has provided guidance and support, without which this work would not have been possible. He has frequently discussed the fundamentals of semiconductors, and particularly of impact ionization theory.

Thanks to Dr. Seunghyun Lee, Bingtian Guo and co-workers for providing the MBE growth and device fabrication, and I also truly appreciate Dr. Shiyu Xie's support. I would like to thank Dr. Yuchen Liu and Dr. Xin Yi for their valuable guidance at the initial stage of the prohect. I would like to thank Mr Harry Lewis for his help during my PhD studies as my mate. In addition, I would like to express my gratitude to Dr. L. W. Lim and Mr. Tarick Osman who guided me through the device fabrication, assistance with the experimental set-up, and numerous discussions.

Thanks for everyone in the Impact ionization group (2018-2022) at the University of Sheffield. I really appreciate their support and help.

Finally, and most significantly, I want to express my gratitude to my parents for their constant financial and moral encouragement.

Abstract

This work aims to demonstrate a separate absorber, charge, multiplication (SACM) avalanche photodiode (APD) with GaAsSb/AlGaAsSb grown on InP. AlAsSb shows very dissimilar ionization coefficients between electrons(α) and holes(β) and extremely low excess noise. The temperature dependence breakdown coefficient (C_{bd}) in AlAsSb was found to be very, small 8.5mV/K in a 1μm p-i-n diode, and the electron and hole impact ionization coefficients increase at about the same rate as the temperature decreases, significantly less so than in InP and InAlAs. However, this material suffers from oxidization and surface leakage current. This is significantly improved by employing the AlGaAsSb quaternary alloy system, enabling low dark current while maintaining low excess noise and a large α/β ratio. The extraction of ionization coefficients from avalanche multiplication measurements has clarified this material's characteristics and optimized the avalanche region thickness in SACM APD design. It is the first report of a room temperature, ultra-high gain (M=278, λ=1550 nm, V=69.5 V, T=296 K) linear mode avalanche photodiode, grown on an InP substrate using a $GaAs_{0.5}Sb_{0.5}/Al_{0.85}Ga_{0.15}As_{0.56}Sb_{0.44}$ separate absorption charge and multiplication (SACM) heterostructure. This design employs a novel GaAsSb absorber that is graded to wider bandgap charge and multiplication layers with several $Al_xGa_{1-x}AsSb$ grading layers. This represents a ~10× gain improvement over commercial, state-of-the-art InGaAs/InP-based APDs (M ~30) operating at 1550 nm. The excess noise factor is extremely low (F<3) at M=70 and this design gives a quantum efficiency of 5935.3% at maximum gain. A 200 μm diameter device gives a capacitance limited 3 dB bandwidth of 0.7 GHz (M=25, V=65 V). Furthermore, this SACM APD shows an extremely low-temperature-dependent breakdown coefficient (C_{bd}) of ~11.83 mV/K, which is ~10× lower than equivalent InGaAs/InP commercial APDs. This demonstration opens a pathway to realize high sensitivity receiver systems at eye-safe, infrared wavelengths (1400 - 1650 nm) for a variety of applications.

Publications

Journal publications

- Jamal Ahmed, Shiyu Xie, Baolai Liang, Xin Yi, **Xiao Jin**, Manoj Kesaria, John P. R. David, "Theoretical Analysis of $AlAs_{0.56}Sb_{0.44}$ Single Photon Avalanche Diodes With High Breakdown Probability," in *IEEE Journal of Quantum Electronics*, vol. 57, no. 2, pp. 1-6, April 2021, Art no. 4500206, doi: 10.1109/JQE.2021.3058356.

- **Xiao Jin**, Shiyu Xie, Baolai Liang, XinYi, Harry I. J. Lewis, Leh W. Lim, Yifan Liu, Beng Koon Ng, Diana L. Huffaker, Chee Hing Tan, Duu Sheng Ong, John P. R. David., "Temperature Dependence of the Impact Ionization Coefficients in AlAsSb Lattice Matched to InP," in IEEE Journal of Selected Topics in Quantum Electronics, vol. 28, no. 2, pp. 1-8, March-April 2022, Art no. 3801208, doi: 10.1109/JSTQE.2021.3099912.

- Bingtian Guo, **Xiao Jin (Shared first author)**, Seunghyun Lee, Sheikh Z. Ahmed, Andrew H. Jones, Xingjun Xue, Baolai Liang, Harry I. J. Lewis, Sri H. Kodati, Dekang Chen, TJ Ronningen, Chris H. Grein, Avik W. Ghosh, Sanjay Krishna, John P. R. David, Joe C. Campbell , "Impact Ionization Coefficients of Digital Alloy and Random Alloy $Al_{0.85}Ga_{0.15}As_{0.56}Sb_{0.44}$ in a Wide Electric Field Range," in Journal of Lightwave Technology, vol. 40, no. 14, pp. 4758-4764, 15 July15, 2022, doi: 10.1109/JLT.2022.3169008.

- Seunghyun Lee, **Xiao Jin (Shared first author)**, Hyemin Jung, Harry I. J. Lewis, Yifan Liu, Bingtian Guo, Sri H. Kodati, Maria Schwartz, Chris H. Grein, TJ Ronningen, John P. R. David, Joe. C. Campbell, and Sanjay Krishna, "High gain, low noise 1550 nm GaAsSb/AlGaAsSb avalanche photodiodes," Optica 10, 147-154 (2023)

- TJ Ronningen, Sri H. Kodati, **Xiao Jin (Shared first author)**, Harry I. J. Lewis, Xiaofeng Tao, Bingtian Guo, Nathan Gajowski, Seunghyun Lee, Piotr Martyniuk, Andrew H. Jones, John P. R. David, Joe C. Campbell, Chris H. Grein, Sanjay Krishna, Impact ionization coefficients in AlInAsSb on InP substrate. **(In preparation)**

- Harry I. J. Lewis, **Xiao Jin (Shared first author)**, Bingtian Guo, Seunghyun Lee, Hyemin Jung, Sri. H. Kodati, Baolai Liang, Sanjay Krishna, Joe C. Campbell and John P. R. David., Excess noise in $Al_{0.85}Ga_{0.15}As_{0.56}Sb_{0.44}$ Avalanche Photodiodes. **(submitted to APL photonics)**

Conference presentations

- **Xiao Jin**, Shiyu Xie, Baolai Liang, Xin Yi, Harry I. J. Lewis, Leh W. Lim, Yifan Liu, Beng Koon Ng, Diana L. Huffaker, Chee Hing Tan, Duu Sheng Ong, John P. R. David, "Comparison of the temperature dependence of impact ionization coefficients in AlAsSb, InAlAs, and InP," Proc. SPIE 11997, Optical Components and Materials XIX, 119970B (4 March 2022); https://doi.org/10.1117/12.2609929

- **Xiao Jin**, Bingtian Guo, Harry I. J. Lewis, SeungHyun Lee, Baolai Liang, Sanjay Krishna, Joe C. Campbell, John P. R. David, "Excess noise measurements in $Al_{0.85}Ga_{0.15}As_{0.56}Sb_{0.44}$ avalanche photodiodes," Proc. SPIE 12139, Optical Sensing and Detection VII, 1213907 (17 May) 2022) https://doi.org/10.1117/12.2624285

- Harry I. J. Lewis, **Xiao Jin**, Bingtian Guo, SeungHyun Lee, Hyemin Jung, Sri H. Kodati, Baolai Liang, Sanjay Krishna, Joe C. Campbell, and John P. R. David Excess noise measurements and impact ionization coefficients in $Al_{0.85}Ga_{0.15}As_{0.44}Sb_{0.56}$ avalanche photodiodes, 64th EMC Columbus, 03/07/2022.

- Harry I. J. Lewis, Liang Qiao, Jeng Shiuh Cheong, Aina N.A.P. Baharuddin, Andrey B. Krysa, Beng Koon Ng, **Xiao Jin**, James E. Green, John P. R. David., Variation in Impact Ionization Coefficients with Alloy Composition in Aluminium-Gallium Containing III-V Compounds, UK semiconductors conference, 06/07/2022

- John P. R. David, **Xiao Jin**, Bingtian Guo, Seunghyun Lee, Harry I. J. Lewis, Hyemin Jung, Sri Harsha Kodati, Baolai Liang, Sanjay Krishna, Joe C. Campbell. Avalanche Multiplication and Excess Noise Characteristics in Antimony Based Avalanche Photodiodes, SPIE Berlin, 09/2022

- Seunghyun Lee, Hyemin Jung, **Xiao Jin**, Harry I. J. Lewis, John P. R. David, and Sanjay Krishna. MBE growth optimization of thick random alloy $Al_{0.85}Ga_{0.15}As_{0.44}Sb_{0.56}$ avalanche photodiodes on InP, ICMBE conference, 09/2022

- Hyemin Jung, Seunghyun Lee, Yifan Liu, **Xiao Jin**, John P. R. David, and Sanjay Krishna, Material growth and device characterization of PIN GaAsSb photodiodes on InP substrate for 1.55 μm wavelength detection, ICMBE conference, 09/2022

Chapter 1:

Introduction

1.1 Overview

A communication system is useful in transmitting information between places which are separated by kilometers, and even for transoceanic distances. An electromagnetic carrier wave can carry information with a frequency of MHz to several hundred THz. Optical communication systems are applied widely, compared to microwave communication systems, because optical communication can be operated in the visible or near-infrared region of the electromagnetic spectrum with a much higher carrier frequency (~100 THz). This provides more transmission bandwidth which enables far more data to be transmitted in less time. Optical fibers are used in fiber optical communications systems. Since 1980, such optical systems have been utilized worldwide[1] and have revolutionized the field of telecommunications. Since then, the global telecommunications system has been accelerated by next-generation telecommunications technology, such as satellite and wireless communication. However, optical fiber communication has advantages because it has high bandwidth, low cost and long-distance capability. Optical fiber communication shows significant advantages compared to microwave communication systems. In the long-haul telecommunication systems, the optical fiber communication low loss windows are at wavelengths of 1.31 and 1.55µm, respectively. At the 1.31µm, optical fibre transmission has low loss (0.6dB/km). This is further reduced to 0.2dB/km for 1.55µm.

Lidar (Laser Imaging Detection and Ranging) is a technology for determining ranges by measuring the time for the light to reflect and return to the detector after a laser pulse. It is commonly used in making high-resolution maps and 3D scanning, but the most transformative application is autonomous vehicles. This system has the capability to detect and recognize objects such as buildings, vehicles and pedestrians during the day and night. Lidar systems can detect objects over 200 meters distance at a typical speed of 75mph [2]. The vehicle can only react and manoeuvre according to any potential obstacle without endangering other vehicles if lidar can detect accurately under various weather conditions. Currently, 0.95µm, 1.31µm and 1.55µm are the wavelengths of interest for lidar applications. It requires high sensitivity photodetector to operate at 1.3µm and 1.55µm, which are considered eye-safe (longer than 1.4µm).

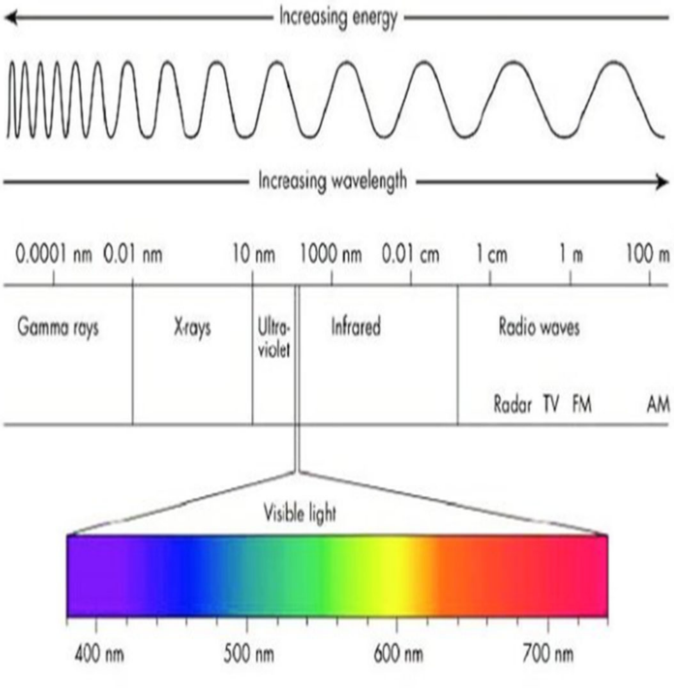

Figure 1.1: Schematic of the electromagnetic spectrum [3]

Photodetectors play a vital role in optical fiber communications and lidar systems when operated in near-infrared regions (0.8µm to 1.6µm). They are also commonly applied in virtually any optoelectronic system and application such as house security systems, CCD cameras and other everyday applications. Semiconductor materials can be used as photodetectors, e.g., Silicon, GaAs, InP, and InAlAs. These semiconductors have different bandgaps (E_g) that vary from a few meV to a few eV, enabling detection in the spectral range from far infrared to ultraviolet. In addition, photodetectors are compact and operate at a low biasing voltage and with high reliability. Photodetectors are solid-state devices that can convert optical signals into electric signals by using photoelectric effect. There are three operation processes for a general semiconductor:

1) Electron-hole generation upon the absorption of incident light.
2) Carrier movement due to diffusion or drift.
3) Carriers are collected by the electric field, providing the output signal.

Photodetectors can demodulate the light signal and convert the optical variations into an electrical signal. Since the photoelectric effect is closely related to the photon energy (hc), the relationship between the bandgap (E_g) and wavelength(λ) can be expressed as follows:

$$\lambda = \frac{hc}{E_g} \tag{1.1}$$

Where h is the Planck constant and c is the light speed.

The photon energy must be larger than the bandgap (E_g), in order to generate an electron and hole pair (EHP). Equation 1.1 shows the maximum wavelength of light that the material can absorb, and the semiconductor materials are chosen and optimized for the wavelength of interest, as shown in Figure 1.1. For example, GaAs is used for applications at 0.9μm, Ge for 1.3μm and InGaAs for 1.55μm. The performance metric of a photodetector can be determined by responsivity, sensitivity, speed, and noise. The background section will discuss these in detail (Chapter 2). There are different photodetectors available including photoconductors, phototransistors, photomultiplier tubes (PMTs), photodiodes and avalanche photodiodes.

1.2 Type of photodetectors

1.2.1 Photoconductors

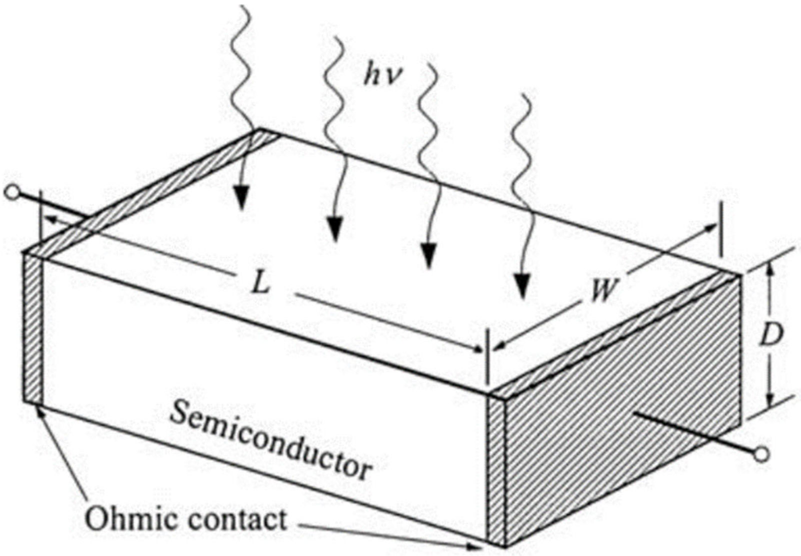

Figure 2.2: A Schematic diagram of photoconductor[4]

The photoconductor is made of a semiconductor slab and has ohmic contacts at each end as shown in Figure 1.2. Carriers are generated by a band-to-band transition mechanism when the light is focused onto the semiconductor. The electrons travel to the anode while holes travel to the cathode. Electrons have shorter transit time than lifetime whereas holes transit time is longer than the lifetime. Due to the difference in electron and hole velocity, electrons are swept out of the detector quickly, but the holes demand charge neutrality and more electrons are supplied from the other electrode. Electrons are going through the detector many loops during the carrier lifetime. This process provides the internal gain for the photoconductor, which can be up to 10^6 [4]. The internal gain can be quantified by measuring the current change at a given voltage. The advantage of a photoconductor is that it has a simple structure and can be fabricated at a low cost. Photoconductors are commonly used in infrared detection but are limited by the slow operating speed since response time is determined by the carrier lifetime.

1.2.2 Phototransistors

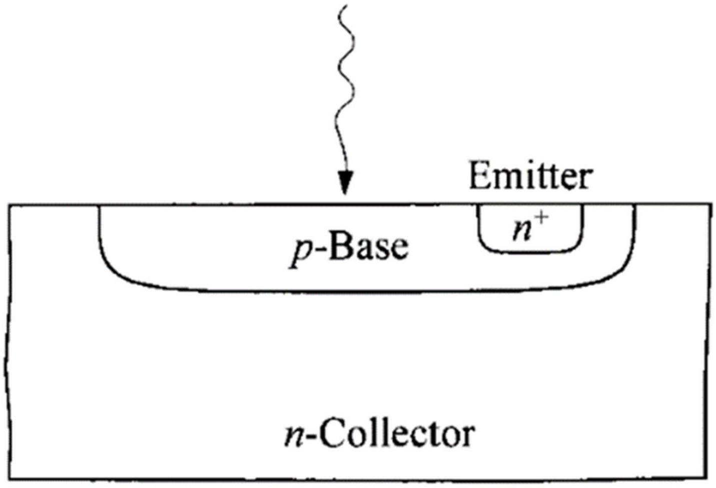

Figure 3.3: A Schematic diagram of photoconductor[4]

Figure 1.3 shows a schematic diagram of phototransistor. The operating principle of phototransistors is to achieve high gain through a bipolar-transistor junction. In an n-p-n phototransistor, the holes in the base/collector depletion region travel to the energy maximum by diffusion and are trapped in the base region. The positive charge accumulated in the base region raises the potential and allows a large current to flow from emitter to collector. The small hole current results in a large electron current, improving the emitter injection efficiency, which is the multiplication mechanism for bipolar transistors and phototransistors. The high injection efficiency heterojunction phototransistor (HPT) with a wider-band gap material emitter has been used in optical fibre communications [5]. HPTs have been recognized as a good candidate for a photodetector for optical fibre communications at 1310nm and 1550nm wavelength in the 1980s [5] since the advantage of HPT is that they have a lower operating voltage than APDs. Moreover, they can achieve high gain values without including multiplication noise. However, the large capacitance at the base-collector junction limits the high frequency response of the phototransistor. To enable phototransistors to pick up sufficient photons, the junction is designed to be large.

1.2.3 Photomultiplier tubes (PMTs)

Photomultiplier tubes are made of a photocathode and an electron multiplier as shown in Figure 1.4. The electron accelerates in the electric field and reaches a dynode when a single photon is injected from the photocathode. New carriers are generated due to the collision between the injected electron and dynode. PMTs can typically generate a gain of ~10^6 by repeating the collision process several times with negligible noise [6]. However, this process highly depends on the electric field across the dynode, and on the number of dynodes. PMTs can be used in photon-starved applications such as single photon detection and have high sensitivity. The major problem with PMTs is operating voltage, which can exceed 1000V. Even though lots of efforts are made to reduce the operating voltage below 1000V [7], the size of PMTs is larger than other photodetectors due to the long vacuum tube required for multiplication. In addition, the fragile nature of PMTs makes them hard to implement in some applications, especially when the trend is to minimize the electronic device size. Additionally, the quantum efficiency of PMTs decreases from 40% at short wavelengths (400nm-700nm) to 2.5% at long wavelengths (900nm-1600nm) [7]. Because of low quantum efficiency in the photocathode, the high-resolution imaging applications of PMTs are limited.

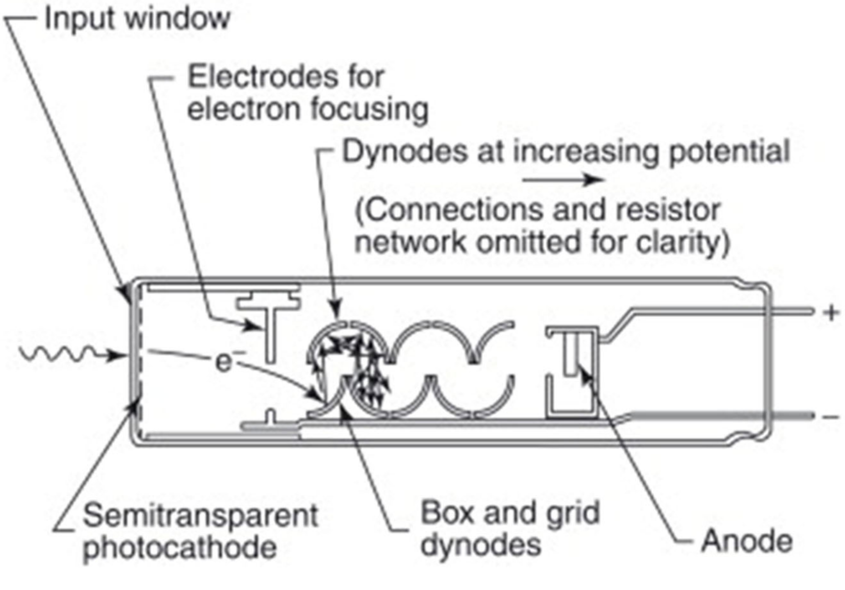

Figure 4.4: A Schematic diagram of Photomultiplier[8]

1.2.4 Photodiode

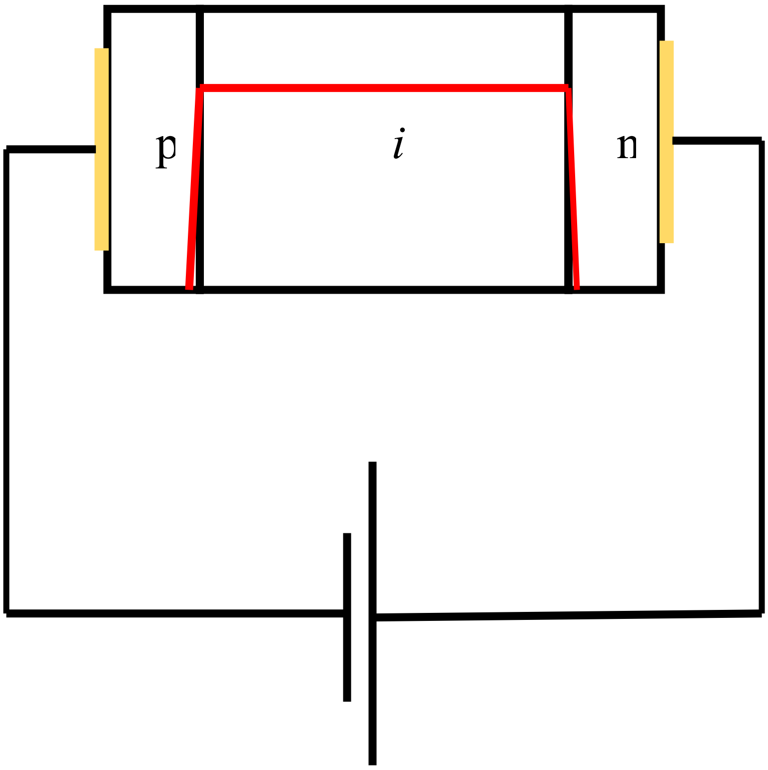

Figure 1.5: A schematic diagram of a p-i-n diode (red lines represents the electric field distribution and yellow bars represents the metal contact)

Photodiode (PDs) have p-n or p-i-n configurations. Figure 1.5 shows that they have a high electric field depleted region to sweep out electron and hole pairs generated by incident photons. The depletion region must be kept thin to reduce the transit time for high-speed operation. However, there is a trade-off since the quantum efficiency requires a thick depletion region to ensure enough electrons hole pairs are generated inside the electric field. This conventional p-n and p-i-n diode can be used in visible and near-infrared detection. Photodiodes are usually reverse biased to increase the drift velocity, reducing the transit time. Photodiodes demonstrate high quantum efficiency and short response times when reverse biased. Because carriers travel at the saturation velocity in the depletion region. The electric field is designed to be low in the *i*-region to avoid triggering impact ionization. A photodiode's sensitivity is lower than an avalanche photodiode's (APD).

1.2.5 Avalanche photodiodes (APDs)

For photon-starved applications, such as free space communication or lidar, it is essential to amplify the signal since the photocurrent level is low. Avalanche photodiodes (APDs) provide internal gain when operating at high electric fields where impact ionization achieves high sensitivity and low noise at high bandwidth. Carriers must gain sufficient energy when accelerating in the electric field to reach the impact ionization's threshold energy (E_{th}). Carriers generated due to the incident of the light can be multiplied through the impact ionization process to produce secondary electrons and holes. The newly created carriers can then travel in the electric field to gain enough energy and cause further cascade impact ionization events, leading to avalanche multiplication (*M*). However, due to the stochastic nature of impact ionization process, there is deviation in the overall multiplication value giving rise to excess noise (*F*), which increases with the increase of multiplication *(M)*. The dark current will increase with reverse voltage bias since the dark current is also multiplied by the internal gain. The overall signal-to-noise ratio (SNR) of the system is therefore given by:

$$\mathrm{SNR} = \frac{I_{ph}}{2q\left(I_{ph}+I_d\right)F(M)B+\sigma_{\mathrm{circuit}}^2/M^2} \tag{1.2}$$

where I_{ph} is photocurrent, I_d is dark current and M is multiplication. B and $\sigma_{\mathrm{circuit}}^2$ are the bandwidth and RMS noise current in an amplifier respectively.

From equation 1.2, the overall SNR improves initially with increasing *M* as the circuit noise can be effectively suppressed by *M*. The excess noise (*F*) is also dependent on *M*. This term will start to dominate the overall SNR for high values of *M*. In other words, the useful multiplication is limited by the excess noise factor, as shown in Figure 1.6.

$$F(M) = k_{eff}M + (1 - k_{eff})\left(2 - \frac{1}{M}\right) \tag{1.3}$$

Where k_{eff} is the ratio of hole ionization coefficient(α) to electron ionization coefficient(β) for electron-initiated impact ionization and $k_{eff} = \alpha/\beta$ for hole-initiated impact ionization event.

The excess noise factor (*F*) is a material-dependent characteristic which increases with increasing *M* at a rate determined by k_{eff}. In order to achieve a low *F(M)* for electron-initiated multiplication, it is crucial to have a material with small k_{eff}. Therefore, it is important to have a good understanding of the excess noise characteristic when designing APDs. A detailed theory of impact ionization and APDs is provided in the next chapter.

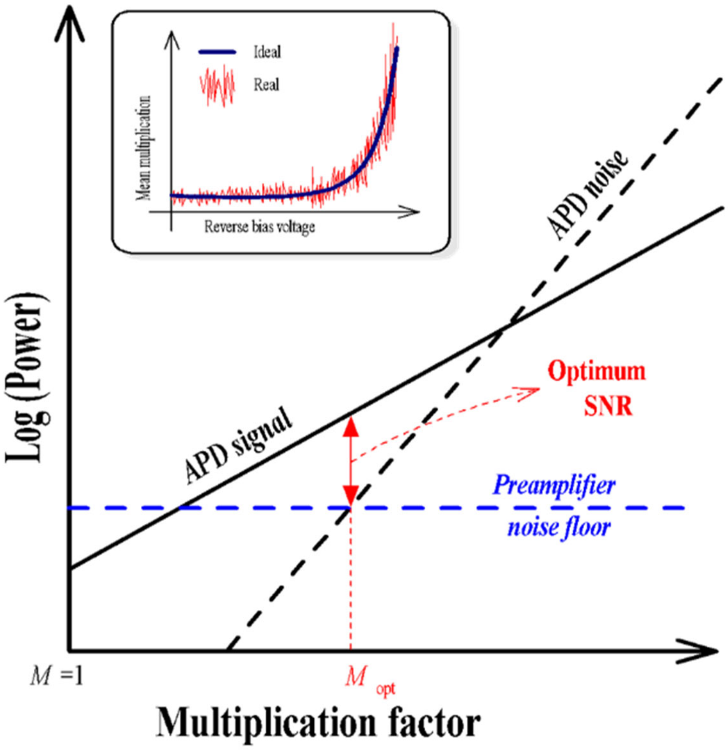

Figure 1.6: A diagram to show signal and noise power variation with different multiplication values.

As shown in equation 1.2, the dark current can also affect the overall signal-to-noise ratio (SNR). The shot noise which arises from generation and recombination current in the depletion region, surface leakage current and tunnelling current needs to be low to achieve a desired level of sensitivity. Guard rings and SU-8 photoresist passivation are used to help reduce the surface leakage of the mesa diode. However, the tunnelling current is always a problem when the electric field is large.

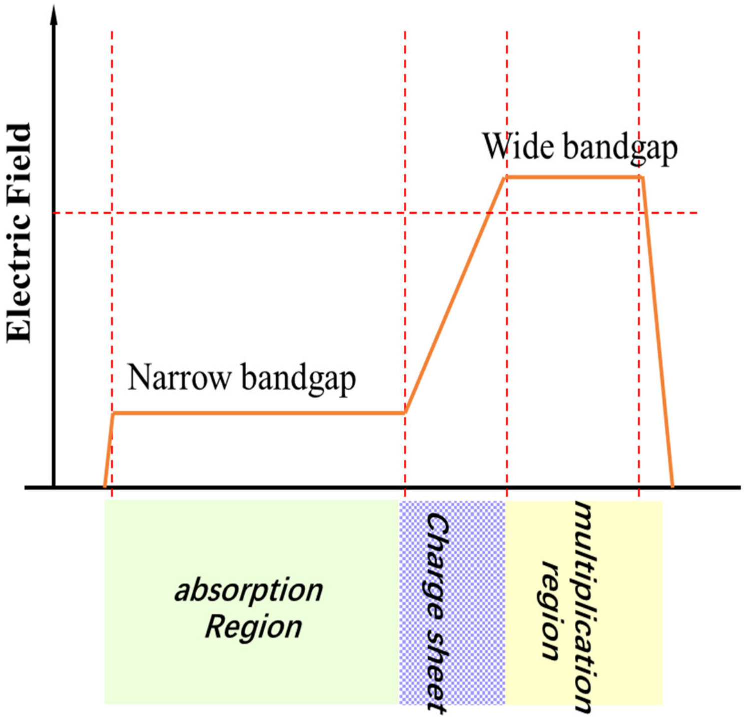

Figure 1.7: SACM APD electric field distribution

Therefore, a type of structure known as the separate absorption, charge and multiplication region (SACM) APD has been used in long wavelength detection (typically 1310nm and 1550nm). Some studies of InP-based APDs show the benefits of this design improving the sensitivity and bandwidth of the optical communication systems [9]–[11].

This design uses a narrow bandgap material such as InGaAs or GaAsSb (lattice matched to InP substrate) as an absorber region to harvest the long wavelength photons and a wide bandgap material to amplify the signal, as shown in Figure 1.4. InP and InAlAs are commonly used as multiplication region materials. The SACM structures are essential in reducing the dark tunnelling current in the narrow bandgap absorber by tailoring the electric field to be low in that region and high in the multiplication region. Because of the small β/α ratio in these materials, the gain-bandwidth (GBP) and sensitivity are limited, resulting in a low bit error rate (BER) when the operating speed increases.

1.3 Competing materials for photodetectors

The performance of photodetectors is highly dependent on material physics. In this section, a literature review of different photodetector materials is provided. Jun-ichi Nishizawa, a Japanese engineer, invented the APD in 1950 [12]. However, some detailed studies on avalanche breakdown and optical detection using p-n junctions in silicon and germanium predate this innovation of APDs. With the growing interest for low noise and high-speed receivers, the focus has been on investigating materials with dissimilar electron and hole ionization coefficients since McIntyre's theory of impact ionization shows a small β/α ratio will yield low excess noise [13]. In addition, Emmons also showed that a small β/α ratio would improve the bandwidth of an APD [14].

Initially, GaAs and silicon with a bandgap (E_g) of 1.42eV and 1.12eV were used to operate at a wavelength between 800nm to 900nm. Silicon has been the desired choice undoubtedly because of the low cost and very dissimilar α and β [15],[16]. Silicon has excellent excess noise characteristics with a k_{eff} value below 0.05 [17], [18]. However, silicon is limited by the detection wavelength, which extends only to the near-infrared region. And the quantum efficiency is low due to the nature of indirect bandgap. Researchers have used SiGe to detect 1550nm wavelength light and have achieved bandwidths of 25Gb/s with a sensitivity of -11.4 dBm[19], [20]. However, the lattice mismatch(dislocation) between the Si and Ge is a problem which leads to high dark current.

The next generation of lightwave communication systems used 1310nm and 1550nm wavelengths to avoid signal degradation by the losses in the fiber. This wavelength range drives the development of III-V material studies to operate in the range of interest for telecommunications. InGaAs (E_g~0.75eV) can operate at both 1310nm and 1550nm, and it is commercially available. The optical absorption is high in the near-infrared region. The maximum electric field that can be applied to InGaAs is limited by the tunnelling current (I_{tunnel}), despite the small β/α and low excess noise existing in this material [21]. This problem has been addressed by using a SACM-APD structure. This configuration is achieved by having a wide band gap material such as GaAs, InP or InAlAs as a multiplication region where tunnelling is inconsequential. The narrow bandgap material in the absorber region operates at a low electric field.

InGaAs-GaAs nanowire APDs can operate in Geiger mode and InGaAs nanopillar growth on GaAs makes the detection of 1300nm and 1550nm practical[22], [23]. APD operates in Geiger mode means that it was biased slightly above the breakdown threshold voltage. Avalanche breakdown will occur when an electron-hole pair generated upon the incident of photon[24]. Then, the current is quenched and ready for another photon detection after avalanche breakdown. Despite nanowire structure can be flexible, InGaAs/GaAs suffers from lattice mismatch. Rather than having GaAs as the multiplication region, there are more studies utilizing InP and InAlAs as multiplication regions since they show a larger difference between α and β. InP/InGaAs SAM-APDs can reach an 80GHz bandwidth at 1550nm with good reliability [25], while InAlAs/InGaAs can reach 23GHz at the multiplied responsivity of 4.06A/W[9]. Although InP/InGaAs is a mature technology for commercial use, the high noise limits the performance in some photo-starved applications. More surprisingly, Xie et al. reported a novel InGaAs/AlGaAsSb APD grown on an InP substrate with a GBP of 424 GHz, the highest value recorded for all InP lattice matched APDs. This material shows the great potential for operating at 10Gb/s or above[26].

Mercury Cadmium Telluride (HgCdTe hereafter) APDs with bandgap (E_g) of ~0.55eV show negligible hole-initiated ionization at room temperature. This yields a very low excess noise factor of ~1.5 in HgCdTe [27], [28]. The HgCdTe offers a tunable bandgap by varying its Hg and Cd compositions to optimize operation at a given wavelength.

This material is targeting for high-specification applications for military and space communication. However, there are some problems with HgCdTe. For example, mercury is toxic and it has to operate at cooled condition due to the high dark current at room temperature. Also, it is challenging to perform epitaxial growth on expensive CdTe or CdZnTe substrate. These issues related to HgCdTe APDs have driven researchers to work on its replacements. Another material that has similar bandgap (~0.34eV) is InAs. InAs APDs show comparable excess noise characteristics (*F*<2) in mesa and planar devices [29], [30]. In addition, it shows the capability of reaching a high gain-bandwidth product(GBP) of 580 GHz[31]. But, InAs shows high-temperature instability and high leakage, making it difficult to apply to practical applications.

1.4 Motivations

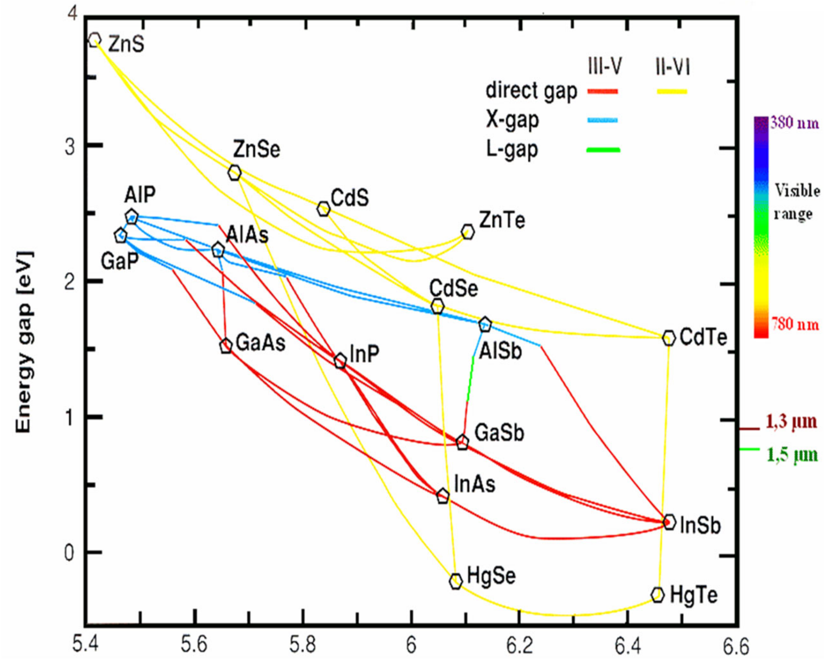

Figure 1.8: Lattice energy diagram of different material alloys[32]

The targets of designing APDs and SAM-APDs are to achieve low dark current, low excess noise factor, high sensitivity, high speed and small β/α ratio. Since the demand for high-speed and high-sensitivity communication is increasing every year, people are looking for an alternative to silicon. This demand has motivated detailed study on III-V materials. Recently, there is a growing interest in studying APD materials lattice-matched to InP substrates and with small β/α ratios. This significantly reduces the cost and growth difficulty compared to InAs and HgCdTe and allows growth lattice matched to InGaAs. As shown in Figure 1.8, there are some combinations of alloys which are lattice matched to InP. For example, Woodson *et al.* [33] from the University of Texas demonstrated a digital alloy $Al_xIn_{1-x}As_ySb_{1-y}$ APD with low excess noise, equivalent to a k_{eff} value of 0.015, with an 890nm *i*-region and high quantum efficiency of 68% at 735nm. The low excess noise factor observed in this material may be due to the reduction in β because of the high photon scattering rate and heavy effective hole mass associated with the large antimony atom. It is also suggested that this may be due to mini-gaps in the valence band [34]. In addition to this, Ren *et al.*[35] performed some further research on the characterization of this alloy system where Al composition=30% to 70%, and a k_{eff} value of 0.01-0.05 been achieved. Moreover, this material has been utilized in a SACM-APD structure with $Al_{0.4}In_{0.6}As_ySb_{1-y}$ as the absorber and $Al_{0.7}In_{0.3}As_ySb_{1-y}$ as the avalanche multiplication region to reduce the dark current while achieving low excess noise performance [36] which is comparable to Si. However, this alloy was grown on GaSb, making it less cost-effective. More recently, Kodati *et al.* [37] showed that a 1µm thick AlInAsSb p-i-n APD grown lattice matched to InP can also give a very low k_{eff} of ~0.02, while a 1µm thick AlInAsSb APD on GaSb [33] exhibits a k_{eff} value of 0.015. However, the excess noise factor increases linearly with multiplication, meaning that the advantage of low excess noise is lost when operating at high gain. Yi *et al.* [38] reported that a 1.55µm thick AlAsSb p-i-n APD showed an extremely low k_{eff} of about 0.005. Despite the very low k_{eff} value observed in AlAsSb, one of this material's biggest problems is that it oxidizes in air rapidly with time and has a high surface leakage current. There are some studies that show that adding gallium can reduce the oxidization in high aluminum containing material[39]. So, there has been some interest in the alloy AlGaAsSb which is significantly more stable in air. There have been some studies on the multiplication and excess noise characteristics of AlGaAsSb with 100nm and 200nm i-region thickness p-i-n APDS, showing k_{eff} values of 0.08 and 0.1 respectively under pure electron injection conditions[40].The low excess noise observed in these thin structure is not necessarily due to the β/α ratio, but may be because they benefit from utilizing the effect of “dead-space” [41]. More recently, Taylor-Mew *et al*.[42] reported excess noise measurements on 600nm thick p-i-n APDs, and a very low excess noise was obtained at M<20. Since the excess noise largely depends on the β/α ratio, and this ratio gets smaller at low electric fields giving lower excess noise, it will be interesting to study the avalanche multiplication and excess noise characteristic between bulk AlGaAsSb structures. It was suggested by Sheikh et al.[34] that as the AlAsSb[43] and AlGaAsSb[44] were grown as a digital alloy (DA hereafter), i.e., as alternating thin layers of AlSb and AlAs (13Å)[45] or GaAlAs/GaAlSb(12.8Å)[44], small mini bands were formed in the conduction bands and valence bands. These mini bands are not significantly affecting the electron ionization behaviours as electrons can easily tunnel across the gaps, but in the valence band the holes, with heavier mass, cannot gain sufficient energy while travelling in the electric field to impact ionize easily. The effect of mini bands on impact ionization behavior is complicated. Some studies have reported that the DA growth technique helps reduce the excess noise in certain materials systems, as in AlInAs [46], [47]. It is worthwhile to investigate the variation in this material's excess noise and avalanche multiplication characteristics between the bulk DA grown and a conventional random alloy (RA) grown p-i-n APD. The AlGaAsSb not only lattice matched to InP but also lattice matched to InGaAs and GaAsSb. All the features make it a good candidate for SACM-APD design and commercial availability because of the low cost.

1.5 Organization of thesis

Chapter 1: This chapter introduced the definition of photodetectors and applications followed by the advantages and disadvantages of various types of photodetectors. In addition, some alternative competing materials have been reviewed and discussed the importance of APDs for free space optical and lidar applications. The motivation for this work is also included in this section.

Chapter 2: This chapter presented the merits of characterizing APDs. It includes a short description of the impact ionization process and simulation model for APDs. Theory on analyzing the multiplication and excess noise measurements and how that relates to impact ionization coefficients.

Chapter 3: In this chapter, the background of the experimental methods were discussed, including capacitance-voltage(C-V) current-voltage(I-V), spectral response, avalanche multiplication and excess noise.

Chapter 4: This chapter presented the detailed temperature dependence multiplication characteristics of AlAsSb from 335K to 210K. The temperature dependence of breakdown coefficients was determined from different thickness *i*-region diodes. The temperature dependent ionization coefficients were extracted from the avalanche multiplication measurements with RPL model.

Chapter 5: This chapter showed avalanche multiplication and excess noise results on AlGaAsSb structures under various injection conditions at room temperature. Impact ionization coefficients of AlGaAsSb were extracted from multiplication measurements results with the help of RPL model. Excess noise measurements were performed on AlGaAsSb and the thickness of avalanche multiplication region was optimized.

Chapter 6: This chapter presented a SACM APD comparable to commercially available 1550nm APDs. A detailed Figure of merits is provided, including avalanche multiplication, noise, EQE and temperature dependence.

Chapter 7: In this chapter, key findings of this project were summarized, along with suggestions for future research. This chapter introduces more work on the current devices and layers but also new research on some new materials.

1.6 Contributions

AlAsSb on InP layers was provided by Baolai Liang from UCLA. And AlGaAsSb on InP and SACM structure studied in Chapter 5 and 6 were grown by Seunghyun Lee in Ohio state university. Fabrication of AlAsSb was performed by Xiao Jin and Dr. L. W. Lim. AlGaAsSb and SACM structure are fabricated between Xiao Jin and Hymin Jung. Xiao Jin performed all the temperature dependence characterizations in Chapter 4. Xiao Jin and Harry Lewis did the multiplication and excess noise measurements jointly shown in Chapter 5. Xiao Jin and Yifan Liu performed the GaAsSb absorption coefficients measurements jointly in Chapter 6. Xiao Jin characterized the SACM structure shown in Chapter 6.

1.7 References

[1] "Photodetectors and Solar Cells," in *Physics of Semiconductor Devices*, John Wiley & Sons, Ltd, 2006, pp. 663–742.

[2] D. Chu, S. Aboujja, and D. Bean, "1550nm Triple Junction Laser Diode Outshines 905nm in Automotive LiDAR Eye safe level of 905nm and 1550nm," pp. 1–7.

[3] C. Secades, B. O'Connor, C. Brown, M. J. Walpole, A. K. Skidmore, and T. Wang, "Review of the use of remotely - sensed data for monitoring biodiversity change and tracking progress towards the Aichi Biodiversity Targets : e-book," 2013.

[4] S. M. Sze, *Physics of semiconductor devices.* Wiley-Blackwell, 2006.

[5] J. C. Campbell, “Chapter 5 Phototransistors for Lightwave Communications,” in *Lightwave Communications Technology*, vol. 22, W. T. B. T.-S. and S. Tsang, Ed. Elsevier, 1985, pp. 389–447.

[6] D. R. Walt, I. Biran, and T. K. Mandal, “Fiber-Optic Chemical Sensors,” R. A. B. T.-E. of P. S. and T. (Third E. Meyers, Ed. New York: Academic Press, 2003, pp. 803–829.

[7] S. V. Polyakov, “Photomultiplier Tubes,” *Exp. Methods Phys. Sci.*, vol. 45, pp. 69–82, 2013, doi: 10.1016/B978-0-12-387695-9.00003-2.

[8] C. Burgess, “OPTICAL SPECTROSCOPY | Detection Devices,” P. Worsfold, A. Townshend, and C. B. T.-E. of A. S. (Second E. Poole, Eds. Oxford: Elsevier, 2005, pp. 438–443.

[9] M. Nada, Y. Muramoto, H. Yokoyama, T. Ishibashi, and S. Kodama, “InAlAs APD with high multiplied responsivity-bandwidth product (MR-bandwidth product) of 168A/W·GHz for 25Gbit/s high-speed operations,” *Electron. Lett.*, vol. 48, no. 7, pp. 397–399, 2012, doi: 10.1049/el.2012.0100.

[10] J. C. Campbell *et al.*, “Recent advances in avalanche photodiodes,” *IEEE J. Sel. Top. Quantum Electron.*, vol. 10, no. 4, pp. 777–787, 2004, doi: 10.1109/JSTQE.2004.833971.

[11] M. Nada, T. Yoshimatsu, Y. Muramoto, H. Yokoyama, and H. Matsuzaki, “Design and performance of high-speed avalanche photodiodes for 100-Gb/s systems and beyond,” *J. Light. Technol.*, vol. 33, no. 5, pp. 984–990, 2015, doi: 10.1109/JLT.2014.2377034.

[12] G. W. A. Dummer, “Electronic inventions and discoveries : electronics from its earliest beginnings to the present day,” p. 233, 1983.

[13] R. J. McIntyre, “Multiplication noise in uniform avalanche diodes,” *IEEE Trans. Electron Devices*, vol. ED-13, no. 1, pp. 164–168, 1966, doi: 10.1109/T-ED.1966.15651.

[14] R. B. Emmons, “Avalanche-Photodiode Frequency Response,” *J. Appl. Phys.*, vol. 38, no. 9, pp. 3705–3714, Aug. 1967, doi: 10.1063/1.1710199.

[15] H. D. E. Man, “Measurement of the ionization rates in diffused silicon p-n junctions,” vol. 13, no. 1, pp. 583–608, 1970.

[16] M. H. Woods, W. C. Johnson, and M. A. Lampert, “Use of a Schottky barrier to measure impact ionization coefficients in semiconductors,” *Solid State Electron.*, vol. 16, no. 3, pp. 381–394, 1973, doi: 10.1016/0038-1101(73)90013-0.

[17] V. M. Robbins, T. Wang, K. F. Brennan, K. Hess, and G. E. Stillman, “Electron and hole impact ionization coefficients in (100) and in (111) Si,” *J. Appl. Phys.*, vol. 58, no. 12, pp. 4614–4617, 1985, doi: 10.1063/1.336229.

[18] T. Kaneda, H. Matsumoto, and T. Yamaoka, “A model for reach-through avalanche photodiodes (RAPD’s),” *J. Appl. Phys.*, vol. 47, no. 7, pp. 3135–3139, 1976, doi: 10.1063/1.323107.

[19] X. Zeng, Z. Huang, B. Wang, D. Liang, M. Fiorentino, and R. G. Beausoleil, “Silicon–germanium avalanche photodiodes with direct control of electric field in charge multiplication region,” *Optica*, vol. 6, no. 6, p. 772, 2019, doi: 10.1364/optica.6.000772.

[20] D. D. Cannon *et al.*, “Tensile strained epitaxial Ge films on Si(100) substrates with potential application in L-band telecommunications,” *Appl. Phys. Lett.*, vol. 84, no. 6, pp. 906–908, 2004, doi: 10.1063/1.1645677.

[21] J. S. Ng, C. H. Tan, J. P. R. David, G. Hill, and G. J. Rees, “Field dependence of impact ionization coefficients in In0.53Ga0.47As,” *IEEE Trans. Electron Devices*, vol. 50, no. 4, pp. 901–905, 2003, doi: 10.1109/TED.2003.812492.

[22] A. C. Farrell *et al.*, “InGaAs-GaAs Nanowire Avalanche Photodiodes Toward Single-Photon Detection in Free-Running Mode,” *Nano Lett.*, vol. 19, no. 1, pp. 582–590, 2019, doi: 10.1021/acs.nanolett.8b04643.

[23] A. C. Farrell *et al.*, “Plasmonic field confinement for separate absorption-multiplication in InGaAs nanopillar avalanche photodiodes,” *Sci. Rep.*, vol. 5, no. November, pp. 1–6, 2015, doi: 10.1038/srep17580.

[24]. J. Kindt and H.W. van Zeijl, “Modelling and Fabrication of Geiger mode Avalanche Photodiodes,” vol. 45, no. 3, 1998.

[25] K.-S. Hyun, Y. Paek, Y.-H. Kwon, I. Yun, and E.-H. Lee, “High-speed and highly reliable InP/InGaAs avalanche photodiode for optical communications,” *Quantum Sens. Evol. Revolut. from Past to Futur.*, vol. 4999, no. July 2003, p. 130, 2003, doi: 10.1117/12.479551.

[26] S. Xie *et al.*, “InGaAs/AlGaAsSb avalanche photodiode with high gain-bandwidth product,” *Opt. Express*, vol. 24, no. 21, p. 24242, 2016, doi: 10.1364/oe.24.024242.

[27] J. Beck *et al.*, “The HgCdTe electron avalanche photodiode,” *J. Electron. Mater. 2006 356*, vol. 35, no. 6, pp. 1166–1173, Jun. 2006, doi: 10.1007/S11664-006-0237-3.

[28] X. Sun, J. B. Abshire, J. D. Beck, P. Mitra, K. Reiff, and G. Yang, “HgCdTe avalanche photodiode detectors for airborne and spaceborne lidar at infrared wavelengths,” *Opt. Express*, vol. 25, no. 14, p. 16589, 2017, doi: 10.1364/oe.25.016589.

[29] A. R. J. Marshall, J. P. R. David, and C. H. Tan, “Impact ionization in InAs electron avalanche photodiodes,” *IEEE Trans. Electron Devices*, vol. 57, no. 10, pp. 2631–2638, 2010, doi: 10.1109/TED.2010.2058330.

[30] P. J. Ker, A. R. J. Marshall, J. P. R. David, and C. H. Tan, “Low noise high responsivity InAs electron avalanche photodiodes for infrared sensing,” *Phys. Status Solidi Curr. Top. Solid State Phys.*, vol. 9, no. 2, pp. 310–313, 2012, doi: 10.1002/pssc.201100277.

[31] A. R. J. Marshall, P. J. Ker, A. Krysa, J. P. R. David, and C. H. Tan, “High speed InAs electron avalanche photodiodes overcome the conventional gain-bandwidth product limit,” *Opt. Express*, vol. 19, no. 23, p. 23341, 2011, doi: 10.1364/oe.19.023341.

[32] G. Brill, “New Material System for 3rd Generation IR Applications New Material System for 3 rd Generation IR Applications by Gregory Brill and Yuanping Chen,” no. May, 2014.

[33] M. E. Woodson, M. Ren, S. J. Maddox, Y. Chen, S. R. Bank, and J. C. Campbell, “Low-noise AlInAsSb avalanche photodiode,” *Appl. Phys. Lett.*, vol. 108, no. 8, 2016, doi: 10.1063/1.4942372.

[34] S. Z. Ahmed, Y. Tan, J. Zheng, J. C. Campbell, and A. W. Ghosh, “APD Performance Enhancement: Minigap Engineering in Digital Alloys,” *31st Annu. Conf. IEEE Photonics Soc. IPC 2018*, vol. 34, no. 2, pp. 1–2, 2018, doi: 10.1109/IPCon.2018.8527250.

[35] M. Ren, S. J. Maddox, M. E. Woodson, Y. Chen, S. R. Bank, and J. C. Campbell, “Characteristics of AlxIn(1−x)As(y)Sb(1−y)(x 0.3− 0.7) Avalanche Photodiodes,” vol. 35, no. 12, pp. 2380–2384, 2017.

[36] M. Ren, S. J. Maddox, M. E. Woodson, Y. Chen, S. R. Bank, and J. C. Campbell, “AlInAsSb separate absorption, charge, and multiplication avalanche photodiodes,” *Appl. Phys. Lett.*, vol. 108, no. 19, 2016, doi: 10.1063/1.4949335.

[37] A. Phys *et al.*, “AlInAsSb avalanche photodiodes on InP substrates AlInAsSb avalanche photodiodes on InP substrates,” vol. 091101, no. February, 2021, doi: 10.1063/5.0039399.

[38] X. Yi *et al.*, “Extremely low excess noise and high sensitivity AlAs0.56Sb0.44 avalanche photodiodes,” *Nat. Photonics*, vol. 13, no. 10, pp. 683–686, 2019, doi: 10.1038/s41566-019-0477-4.

[39] K. D. Choquette *et al.*, “Wet oxidation of AlGaAs vs. AlAs: A little gallium is good,” in *Conference Proceedings LEOS’96 9th Annual Meeting IEEE Lasers and Electro-Optics Society*, 1996, vol. 1, pp. 390–391 vol.1, doi: 10.1109/LEOS.1996.565297.

[40] L. L. G. Pinel *et al.*, “ Effects of carrier injection profile on low noise thin Al 085 Ga 015 As 056 Sb 044 avalanche photodiodes ,” *Opt. Express*, vol. 26, no. 3, p. 3568, 2018, doi: 10.1364/oe.26.003568.

[41] S. A. Plimmer, J. P. R. David, and D. S. Ong, “The merits and limitations of local impact lonization theory,” *IEEE Trans. Electron Devices*, vol. 47, no. 5, pp. 1080–1088, 2000, doi: 10.1109/16.841244.

[42] J. Taylor-Mew, V. Shulyak, B. White, C. H. Tan, and J. S. Ng, “Low Excess Noise of Al0.85Ga0.15As0.56Sb0.44Avalanche Photodiode from Pure Electron Injection,” *IEEE Photonics Technol. Lett.*, vol. 33, no. 20, pp. 1155–1158, 2021, doi: 10.1109/LPT.2021.3110123.

[43] X. Yi *et al.*, “Demonstration of large ionization coefficient ratio in AlAs0.56Sb0.44 lattice matched to InP,” *Sci. Rep.*, vol. 8, no. 1, pp. 8–13, 2018, doi: 10.1038/s41598-018-27507-w.

[44] S. Lee *et al.*, “Low noise Al0.85Ga0.15As0.56Sb0.44avalanche photodiodes on InP substrates,” *Appl. Phys. Lett.*, vol. 118, no. 8, pp. 0–5, 2021, doi: 10.1063/5.0035571.

[45] M. C. Debnath *et al.*, "Optical properties of bimodally distributed InAs quantum dots grown on digital AlAs0.56Sb0.44 matrix for use in intermediate band solar cells," *J. Appl. Phys.*, vol. 121, no. 21, p. 214304, Jun. 2017, doi: 10.1063/1.4984832.

[46] J. Zheng *et al.*, "Digital Alloy InAlAs Avalanche Photodiodes," *J. Light. Technol.*, vol. 36, no. 17, pp. 3580–3585, 2018, doi: 10.1109/JLT.2018.2844114.

[47] A. K. Rockwell *et al.*, "Toward deterministic construction of low noise avalanche photodetector materials," *Appl. Phys. Lett.*, vol. 113, no. 10, pp. 0–5, 2018, doi: 10.1063/1.5040592.

Chapter 2

Background

2.1 Impact ionization and avalanche gain

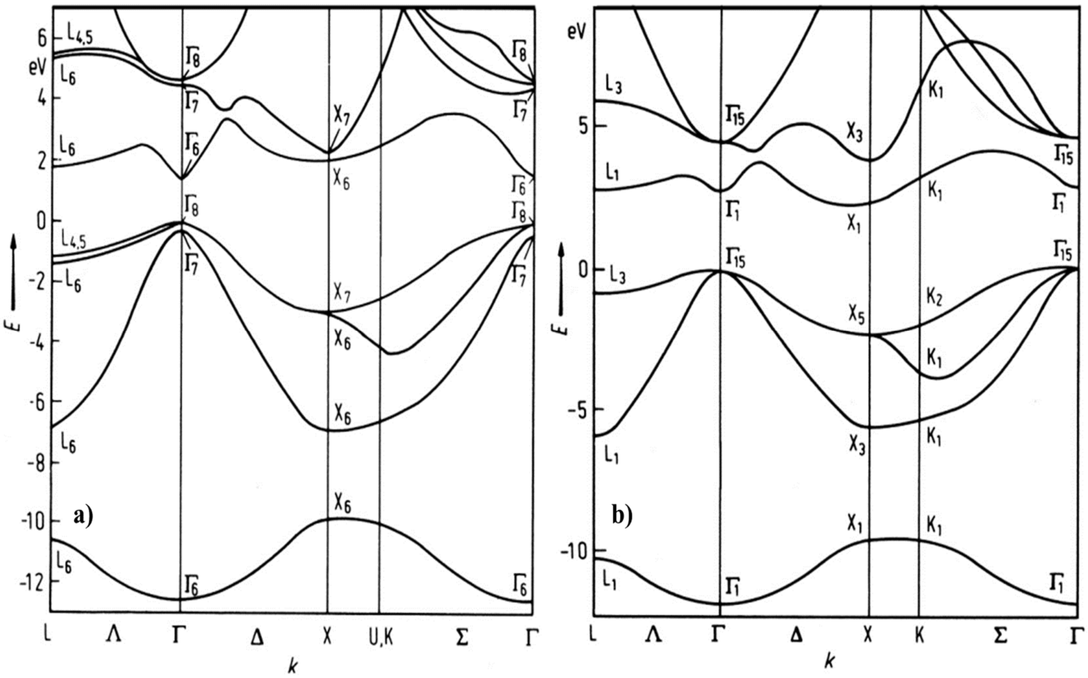

Figure 2.1: **a)** Band structure of GaAs **b)** Band structure of AlAs[1]

Due to the internal multiplication that is provided by impact ionization, APD are widely used in optical detection systems. Because they can provide higher sensitivity and a larger signal to noise ratio than conventional p-i-n diodes. This avalanche multiplication results from the impact ionization process that electrons and holes undergo at high electric fields. For impact ionization, carriers must gain the ionization threshold energy by traversing the high field multiplication region. This threshold energy (E_{th}) depends both on the band structure and bandgap energy, which usually is 1.5 times larger than E_g, by assuming a simple parabolic band structure with identical electron (m_e) and hole masses (m_h)[2]. For a non-parabolic band structure, Anderson-Crowell estimated the E_{th} for electrons as follows [3]:

$$E_{th} = E_g\left(1 + \frac{m_e}{m_e + m_h}\right) \tag{2.1}$$

However, the masses of electrons and holes can be different in different bands and the band structure is complicated. For example, Figure 2.1 shows the calculated band structures of GaAs and AlAs [4]. The maxima of the valence bands in both AlAs and GaAs are located at the center (Γ-point) of the Brillouin zone, and the bands have broadly similar shape. The minima point in the conduction band are located in the X, L and Γ valleys with $E_X > E_L > E_\Gamma$ in GaAs and $E_\Gamma > E_L > E_X$ in AlAs (E_X, E_L, E_Γ are the energy levels at the X, L and Γ symmetry points). The conduction band's lowest point in GaAs is at the Γ-valley, whereas in AlAs it is at the X-valley. Therefore, the smallest energy gap (E_g) in GaAs is at the Γ-valley and it is referred to as a direct bandgap material while AlAs is an indirect bandgap material. The effective masses of electrons and holes are different in X, L and Γ valleys, adding extra complexity in determining the threshold energy.

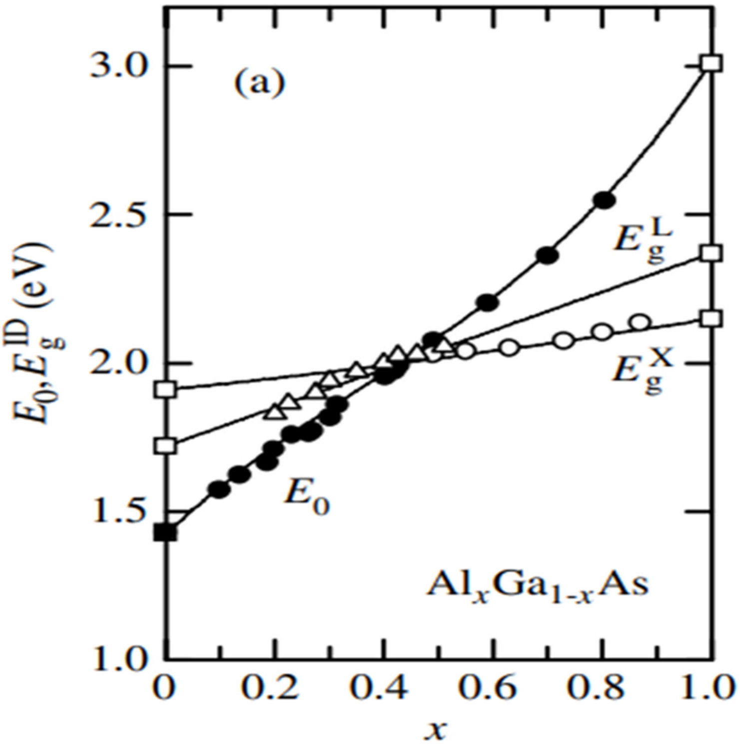

Figure 2.2: Energies of the lowest direct bandgap and indirect bandgap versus x for $Al_xGa_{1-x}As$[5].

The energy levels at different symmetry points are characterized by a cross over from the minimum sequence Γ-L-X in GaAs to X, L and Γ in AlAs. Figure 2.2 shows the lowest direct E_0 and indirect E_g gaps versus x for $Al_xGa_{1-x}As$ (AlGaAs). By changing the ratio of *x*, AlGaAs changes from direct bandgap below *x*=0.43 to indirect bandgap at higher *x*.

Furthermore, a split-off and exists in the valence band to separate the heavy and light holes. In an E-*k* diagram, for valence band the degenerate band with smaller curvature around *k*=0 is called the heavy-hole band, and the one with larger curvature is the light-hole band. In most cases, the assumption of the parabolic band structure is made to simplify the calculation of impact ionization characteristics. However, some reports show that carriers impact ionize from the higher energy bands, which are non-parabolic [6], [7]. Therefore, the value of E_{th} can be challenging to calculate based on the band structure theory.

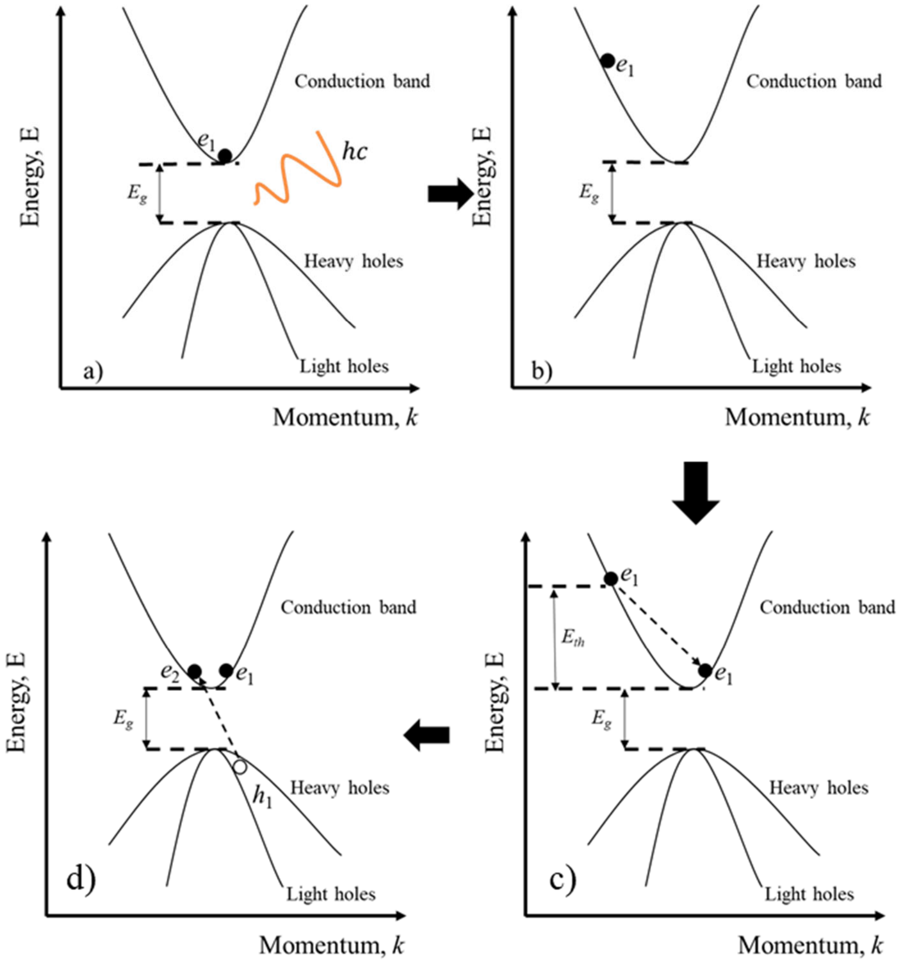

Figure 2.3: A flow diagram to demonstrate electron-initiated impact ionization process.

Figure 2.3 shows a schematic diagram of the electron-initiated impact ionization process in an E-k diagram. In Figure 2.3a, it involves a single promotion from the valence band to the conduction band with the absorption of an incident photon. The primary electron gain energy while travelling in the electric field as shown in Figure 2.3b. The primary carrier e_1 lost a minimum amount of energy greater than E_g for impact ionization during the scattering event as shown in Figure 2c. And in Figure 2d, the energy is then transferred to an electron in the valence band, which is promoted to the conduction band. Another electron, e_2 is generated and leaves behind a hole, h_1, as an outcome of this ionization process. Both primary and secondary carriers continue travelling in the electric field, causing a subsequent impact ionization event that increases the total number of carriers than initially present in the multiplication region, thus amplifying the incoming signal. The energy gained and lost are systematically followed by the energy conservation rule while travelling through the electric field, electrons and holes encounter non-ionization collisions with phonons [8]. Carriers can gain energy hc (phonon absorption), lose energy hc (phonon emission) and exchange momentum (elastic) in the phonon scattering process (h is the planck constant and c is the speed of the light). N_{pc} is the phonon occupation number, and the phonon emission process is proportional to $N_{pc} + 1$ whereas phonon absorption is proportional to N_{pc}. On average, the phonon scattering process is becoming more dominant in the carrier transportation process, which stops carriers gaining sufficient energy to impact ionize. The N_{pc} phonon occupation number is given as follows:

$$N_{pc} = \frac{1}{\exp\left(\frac{hc}{k_B T} - 1\right)} \tag{2.2}$$

Where k_B is the Boltzmann constant, hc is the photon energy, and T is the temperature in Kelvin.

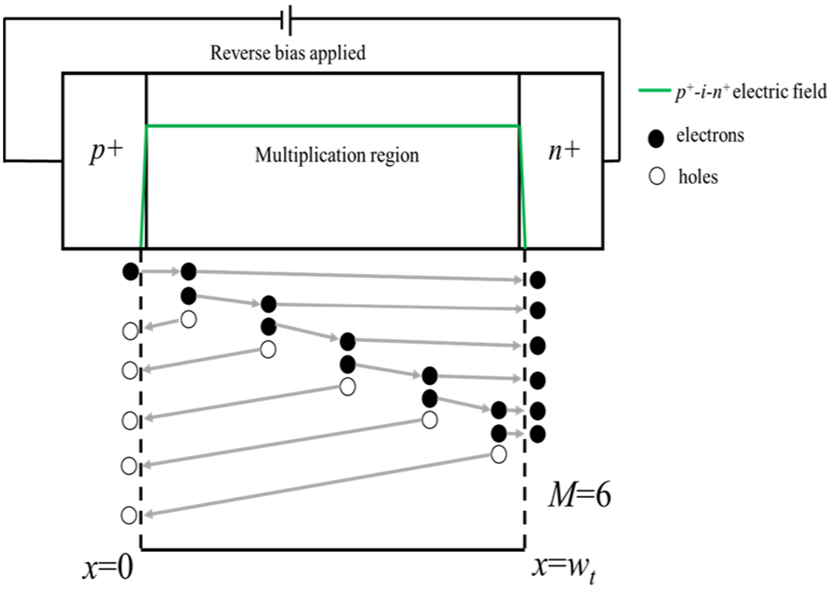

Figure 2.4: A schematic diagram of an impact ionization event with electron initiated.

This phonon scattering process can be highly temperature dependent and a reduction in temperature can lead to a decrease in phonon scattering. Consequently, the probability of impact ionization is increased [9], [10]. In most cases, both α and β increase with a decrease in temperature, but α decrease with temperature increasing whereas β increase in digital alloy InAlAs [11]. Details will be given in Chapter 4.

The average number of ionization events per unit distance travelled by electrons and holes are characterized by α and β. The α and β are material-dependent and vary with the electric field. The reciprocal of α and β represents the average distance a carrier needs to travel prior to an impact ionization event along the direction of the electric field, which is also called the mean ionization path length, $<l>$.

As shown in Figure 2.4 above, an electron is injected at position x_0 and this carrier is travelling in a direction from $x = 0$ to $x = W$. This electron traverses in the high electric field and produces αdx number of impact ionization events, while holes travel in the opposite direction and create βdx ionization events. Therefore, the additional cascading event of impact ionization gives rise to an increased number of electrons and holes in the process referred to as avalanche multiplications, $M(x)$[12].

$$M(x) = \frac{\exp\left[-\int_0^x \left(\alpha(x')-\beta(x')\right)dx'\right]}{1-\int_0^W \alpha(x')\exp\left[-\int_0^{x'} \left(\alpha(x'')-\beta(x'')\right)dx''\right]dx} \tag{2.3}$$

It is well known that the ionization coefficients characterize the impact ionization behavior of electrons and holes, α and β respectively. An electron and hole pair is generated upon the absorption of a photon in the semiconductor. The 'hot' carriers in the high electric field region can trigger a few successive impact ionization events. The field will sweep out the newly generated carriers. They may be able to produce more secondary carriers depending on the position of where they were generated in the electric field. This process increases the number of free carriers to produce a multiplication factor (*M*). This cascading effect is described by equation 2.3 when a carrier is injected at position x.

Assuming pure electron injection in a p-i-n diode, where an electron is injected at x = 0, the multiplication factor M_e can be expressed as

$$M_e = M(0) = \frac{1}{1-\int_0^W \alpha(x')\exp\left[-\int_0^x \alpha(x'')-\beta(x'')dx''\right]dx'} \tag{2.4}$$

The pure hole injection multiplication factor where a hole is injected at $x = w$, M_h, can be expressed as

$$M_h = M(w) = \frac{1}{1-\int_0^W \beta(x')\exp[-\int_x^W \alpha(x'')-\beta(x'')dx'']dx'} \tag{2.5}$$

Since α and β are a function of the electric field, α and β are constant when the avalanche multiplication region is uniform, and equation 2.3 can be simplified into

$$M(x) = \frac{\exp\left[-(\alpha-\beta)x\right]}{1-\int_0^W \alpha\exp\left[-(\alpha-\beta)x'\right]dx'} \tag{2.6}$$

For pure M_e and M_h in the case of uniform electric field profile, equation 2.4 and 2.5 can be further simplified to

$$M_e = \frac{1}{1-\frac{\alpha}{\alpha-\beta}\{\exp\left[(\beta-\alpha)w\right]-1\}} \tag{2.7}$$

$$M_h = \frac{1}{1-\frac{\beta}{\alpha-\beta}\{\exp\,[(\alpha-\beta)w]-1\}} \tag{2.8}$$

Under the assumption that $\alpha \neq \beta$, equation 2.6 becomes

$$M(x) = \frac{\exp\,[-(\alpha-\beta)x]}{1-\frac{\alpha}{(\alpha-\beta)}[1-\exp\,(-(\alpha-\beta)w)]} \tag{2.9}$$

From equation 2.9, high multiplication can be obtained if $\alpha > \beta$ for pure electron injection or $\alpha < \beta$ for pure hole injection. The α/β ratio is closely related to the APD excess noise characteristics. It is important to consider how α and β change with the electric field. When α is much greater than β, the multiplication process will approximate a single carrier multiplication process. In a p-i-n structure, electrons travel in the electric field from p^+ to right n^+ (positive direction) until sufficient energy is acquired to promote an electron from the valence band to the conduction band, leaving a hole in the valence band. On the other hand, holes travel from n^+ to p^+ (negative direction), and only a few holes can impact ionize before they leave the multiplication region. The multiplication increases exponentially with the electric field, as shown in Figure 2.5. In this case, only electrons undergo impact ionization. Therefore, there is less noise and fluctuation in the multiplication process.

Since the carriers require a finite time to traverse the depletion region, a phase difference between the photon flux and the photocurrent will appear when the incident light intensity is modulated rapidly. The regenerative avalanche process results in the presences of a large number of carriers in the high-field region long after the primary electrons have traversed through that section. The higher the avalanche multiplication is, the longer the avalanche process persists. This implies a behavior that is set by a gain-bandwidth product (GBP). The total duration of the impact ionization process is when all the electrons and holes exit the electric field. When $\alpha >> \beta$, the feedback holes (from n^+ to p^+) don't impact hence reduce the total transit time. It provided highest speed (shortest duration) when only one carrier type can impact ionize for a given multiplication.

In this case, $\alpha >> \beta$, *and* equation 2.9 can be further simplified to

$$M = \exp\,(\alpha w) \tag{2.10}$$

In the other extreme case where $\alpha = \beta$, equation 2.6 becomes

$$M = \frac{1}{1-\alpha w} \tag{2.11}$$

In this case, both electrons and holes have equal ionization probability. The duration of the avalanche multiplication process takes longer for all the carriers to exit the electric field, resulting in limited GBP. The avalanche multiplication increases sharply (Figure 2.5) because both carriers contribute to the overall multiplication. However, most of the semiconductor avalanche multiplication is contributed to by both electrons and holes. Depending on the α/β ratio of the material, the multiplication characteristics lie between the two extreme cases considered (red and blue curve in Figure 2.5).

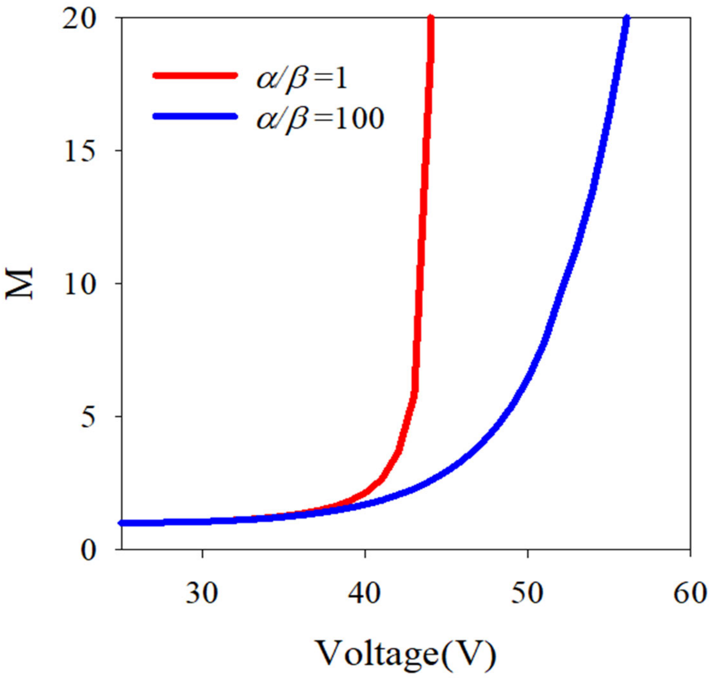

Figure 2.5: Multiplication characteristic for a 1µm perfect p-i-n structure with different α/β ratios.

Since the α/β ratio is of significant importance to the device performance, it is important to characterize these quantities. The easiest way to extract the electron and hole ionization coefficient is to measure the M_e and M_h from p-i-n and n-i-p structures. By rearranging equations 2.7 and 2.8, the α and β at different positions can be expressed in terms of M_e and M_h. Assume that the i-region doping levels are low and that the cladding layer doping is high.

$$\alpha = \frac{1}{w_{\mathrm{T}}}\left(\frac{M_e-1}{M_e-M_h}\right)\ln\left(\frac{M_e}{M_h}\right) \tag{2.12}$$

$$\beta = \frac{1}{w_T}\left(\frac{M_h-1}{M_e-M_h}\right)\ln\left(\frac{M_e}{M_h}\right) \tag{2.13}$$

This equation is only valid for ideal p-i-n and n-i-p structures with thick avalanche regions and low background doping levels. For thin structures, equation 2.12 and 2.13 does not take the cladding layer into account. However, cladding layer depletion can represent a significant fraction of the avalanche region width. In addition, the electric field can vary at different position of the avalanche region if the i-region background doping is high. Ideally, M_e and M_h should be measured on the same device to ensure the same electric field and carrier transportation characteristics. However, the risk of using back illumination is high because substrate grinding and backside alignment can damage the device, and generally complementary p-i-n and n-i-p structures are used instead. Therefore, in order the to extract the ionization coefficients, a numerical method is applied by using equations 2.7 and 2.8 following the method of Grant[13].

2.2 Avalanche breakdown

The definition of avalanche breakdown is when the multiplication becomes infinite. By equating the denominators of equations 2.7 and 2.8 to zero, these two equations can be rewritten as

$$\int_0^W \left[\alpha \exp\left(-\int_0^x (\alpha-\beta)dx'\right)\right]dx = 1 \tag{2.14}$$

$$\int_0^W \left[\beta \exp\left(\int_x^{w_{\mathrm{T}}} (\alpha-\beta)dx'\right)\right]dx = 1 \tag{2.15}$$

It can be shown that the breakdown condition specified in equations 2.14 and 2.15 are identical. The ionization coefficients and the electric field profile determine the avalanche breakdown voltage (V_{bd}), but the injection profile does not affect the V_{bd} [14].

So far, all the discussions and derivations assume that the ionization probability at a given position is only a function of local electric field in thick avalanche region structures, and carriers can quickly reach an equilibrium state. In the case of 'dead-space', the minimum distance that a carrier is required to travel to reach an equilibrium state within an electric field [15]. This distance is negligible compared to the mean carrier ionization path length (l) when the avalanche region is thick. However, in a thin avalanche region structure, the dead-space becomes a significant fraction of the total avalanche region width. In this case, the impact ionization coefficients not only depend on the local electric field but also the carrier's history. The multiplication characteristic can change when considering the dead-space effect, especially the low multiplication values. The effect of the 'dead-space' on multiplication characteristics in GaAs has been studied in detail [16][17]. The local model agrees with experimental multiplication characteristics for structures with avalanche regions larger than 0.2μm and using the effective ionization coefficient, considering the dead-space effect for avalanche region width <0.2μm. 'Dead-space' effect leads to an overestimation of local model at low multiplication values. This experiment proved that in a 0.1μm structure, low multiplication values from local ionization coefficients are higher than the measured values. Consequently, the dead-space effects will suppress the ionization of electrons and holes even at a low electric field, corresponding to the lower multiplication values compared to the thicker avalanche region bulk structures[18], [19]. 'Dead-space' also significantly affects excess noise in APD devices[20]. Details will be discussed in a later section.

2.3 Excess noise

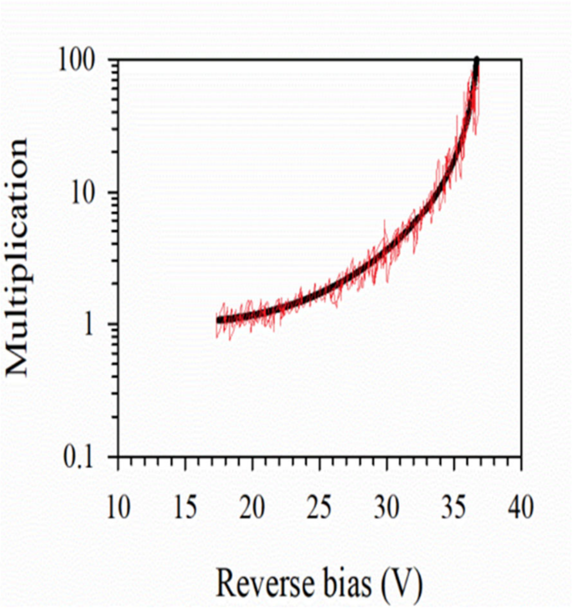

Figure 2.6: A diagram to show fluctuation in the multiplication process.

The stochastic nature of impact ionization results in fluctuation in the multiplication of the electrons and holes. The randomness (M_{ind}) where secondary carriers impact ionize leads to the multiplication fluctuation. The total number of carriers generated by a single carrier injection can have a variety of values. The statistical fluctuation gives rise to a mean multiplication value and distribution of the multiplication. Figure 2.6 shows that typical multiplication characteristics vary with bias. It shows the average multiplication and the multiplication fluctuation, which is closely related to the excess noise in APDs. Since F is the standard deviation of the avalanche multiplication for a single ionization event M_{ind}, from mean multiplication, the excess noise $F(M)$ can be defined as:

$$F = \frac{<M_{ind}^2>}{<M_{ind}>^2} \qquad (2.16)$$

McIntyre[21] showed that the excess noise could be expressed in terms of β/α ratio k_{eff} and multiplication(M), assuming the ionization probability only depends on the local electric field. It concluded that to achieve low excess noise, the dominant carrier type should be injected as the initial carrier in the avalanche region. When $\alpha > \beta$, the excess noise factor *F(M)* for pure electron injection can be expressed as

$$F_e = k_{eff}M + \left(2 - \frac{1}{M}\right)\left(1 - k_{eff}\right) \tag{2.17}$$

When $\beta > \alpha$, the excess noise factor *F(M)* for pure hole injection can be expressed as

$$F_h = k_{eff}M + \left(2 - \frac{1}{M}\right)\left(1 - k_{eff}\right) \tag{2.18}$$

From Figure 2.7, in McIntyre's local model theory, low excess noise is achievable when the ionization coefficients are very different, and the dominant carrier initiates the impact ionization process. The minimum excess noise at high multiplication values is 2 when k_{eff} is zero.

Compared to conventional p-i-n diodes, the most critical advantage is that an APD can provide better sensitivity, in other words, better signal-to-noise ratio (SNR). Because of the internal gain from avalanche multiplication. However, the shot noise originating from the discrete nature of the electric charges also contributes to the overall noise. Assume the injection profile of photons follows the Poisson distribution. The shot noise in the mean square is given by

$$\langle i_s \rangle = 2q(I_d + I_p)B \tag{2.19}$$

Where B is the operating bandwidth, q is the electronic charge, I_d is the dark current and I_p is he photocurrent.

Due to the internal gain in APDs, the shot noise is being amplified, then the mean square noise becomes:

$$< i >= 2q(I_d + I_p)FM^2B \tag{2.20}$$

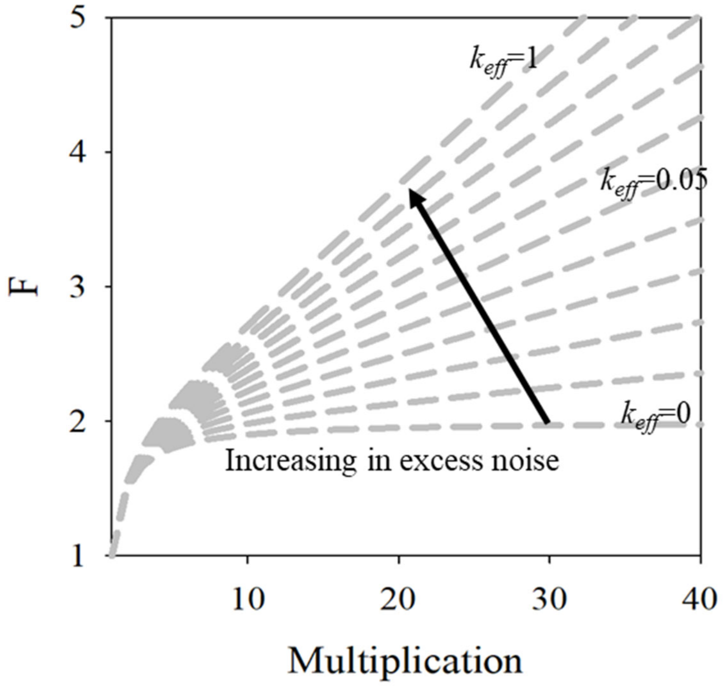

Figure 2.7: McIntyre local model excess noise factor as a function of multiplication with different k_{eff} values from 0 to 0.1 with a step of 0.01.

In general, SNR is the ratio between the average photocurrent power and the total noise. The SNR for APD is given by equation 2.21 [22].

$$\mathrm{SNR} = \frac{(MR_dP_{\mathrm{in}})^2}{2qM^2F(R_dP_{\mathrm{in}}+I_d)\mathrm{B}+n_{circuit}^2} \tag{2.21}$$

R_d is the responsivity at unity gain

P_{in} is the input power

B is the operating bandwidth

$n_{circuit}^2$ is the circuit noise

To fully utilize the advantage of APD, it is necessary to keep the excess noise lower or equal to the circuit noise. From equation 2.17 and Figure 2.7, APD with k_{eff} value close to 0, the maximum excess noise factor (F) it can go to is 2. In this case, the SNR will increase with the increase of multiplication. On the other hand, APD with k_{eff} value close to 1, excess noise will soon dominate the overall total noise and degrade the overall SNR.

For material with $\alpha >> \beta$, αw must be large to reach to high multiplication. There are plenty of electrons in the multiplication region, and a small fluctuation in the number of ionization events will cause relatively small changes in multiplication and hence the smaller excess noise. However, in the case of $\alpha = \beta$, large multiplication can be achieved when αw is close to unity, and fewer electrons are involved in the multiplication process. Therefore, a small fluctuation in the impact ionization process becomes significant, hence high excess noise.

In the conventional McIntyre excess noise theory, the impact ionization process is only a function of electric field, it is independent of the carrier history and dead-space effect and the probability density distribution (PDF) must be ideal exponential decay. The effect of ‘dead-space’ on multiplication is discussed in the previous section. In addition, ‘dead-space’ can also change the excess noise. This ‘dead-space’ effect is becoming a significant fraction as the total distance travelled by the carrier before impact ionization decreases when the avalanche region thickness gets smaller. The ‘dead-space’ can be estimated by using equation 2.22.

$$d_e = \frac{E_{the}}{q\xi} \; and \; d_h = \frac{E_{thh}}{q\xi} \qquad (2.22)$$

Where E_{the} is the electron threshold energy and E_{thh} is the hole threshold energy, q is the electronic charge, ξ is the electric field.

McIntyre's local noise theory described that excess increases when α and β get close to each other at high electric field. However, lower excess noise was observed in thin avalanching region structures, as demonstrated by some recent III-V materials APD measurements [17], [20]. McIntyre's local model is no longer valid when the 'dead-space' effect becomes significant. The local model theory assumes that the noise behaviors of an APD’s ionization probability are always the same at the instant following carrier creation and are independent of carrier history [21]. The 'dead-space' theory assumes that the ionization probability is set to zero immediately after new carrier creation. Considering this, the 'dead-space' effect tends to decrease both average multiplication and excess noise factor [20][23]. This benefits the performance of the optical receiver when used in photon starved applications. It was found that by taking advantage of the 'dead-space' effect can improve the SNR [23].

2.4 APD device performance parameters

2.4.1 Responsivity (R_d) and quantum efficiency(η)

Quantum efficiency (η) is defined as the number of electron-hole pairs created per incident photon. Electron-hole pairs are generated each time a photon is absorbed by the semiconductor when the incident photon energy is larger than the bandgap (E_g). The photocurrent (I_{ph}) generated is proportional to responsivity (R_d) and incident optical power (P_{in}) it is expressed in units of Watts(W).

$$R_d = \frac{I_{ph}}{P_{\text{in}}} = \frac{\eta q}{hv} = \frac{\eta\lambda(\mu\text{m})}{1.24} \qquad (2.23)$$

Where q is the electronic charge, h is the Planck constant and v is the speed of the light and λ is the wavelength of the incident light. Unit of R_d is ampere/wats(A/W).

As described by equation 2.23, the responsivity increases linearly with wavelength for a given quantum efficiency. For a perfect photodiode without any internal gain, the maximum quantum efficiency is 100%, which is 1.24A/W at 1550nm.

2.4.2 Absorption of the light in semiconductors

The absorption of light is a material property of semiconductor devices, based on the photoelectric effect. A photon with larger energy than the semiconductor bandgap can excite an electron-hole pair and then contribute to the photocurrent. Since the photoelectric effect is based on the photon energy *hc*, the relationship between the wavelength and photon energy can be described as follows:

$$\lambda = \frac{hc}{\Delta E} = \frac{1.24}{\Delta E(\text{eV})}\ (\mu\text{m}) \qquad (2.24)$$

Where λ is the wavelength of photon, h is Planck constant ($\sim 4.13 \times 10^{-15}$)eV s), c is the speed of the light ($\sim 3 \times 10^{8}$ m/s) and ΔE is the transition of energy levels.

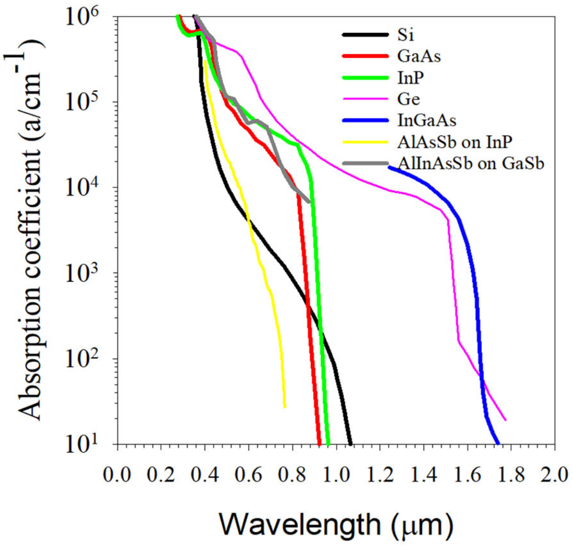

Figure 2.8： Absorption coefficient for different III-V semiconductor materials including Si[24],GaAs[25],InP[26],Ge[24],InGaAs[5],AlAsSb[27],AlInAsSb[28].

The absorption of light is described by the absorption coefficient (γ). This parameter indicates where the light is absorbed and whether the light can be absorbed due to the photoelectric effect. Equation 2.25 described the light absorption characteristics in a material. A high value of absorption coefficients typically ($>10^{5}$cm^{-1}) means that more light is absorbed in the material at a given wavelength. However, most of the light is absorbed near the surface, and the photogenerated carriers recombine before they are collected by the electric field. A low value of the absorption coefficient means that the light is more uniformly absorbed and penetrates deeper into the semiconductor. In the near-infrared region, silicon with an anti-reflection coating, can reach a responsivity of 0.64A/W near 0.8-0.9μm, while Ge and InGaAs also show high responsivity at 1.0 to 1.6μm region. In some cases, light can be transparent to the semiconductor materials, which will not cause photoexcitation. Figure 2.8 shows a series of materials with different bandgap and absorption coefficients. Since the optical absorption coefficient is wavelength dependent for a given semiconductor, the wavelength range in which appreciable photocurrent can be generated is limited. The intensity of the light distribution in the device structure can be described as

$$\varphi = \varphi_0 \exp(-\gamma x) \tag{2.25}$$

Where φ_0 is the initial intensity of the light, and x is the distance light penetrated.

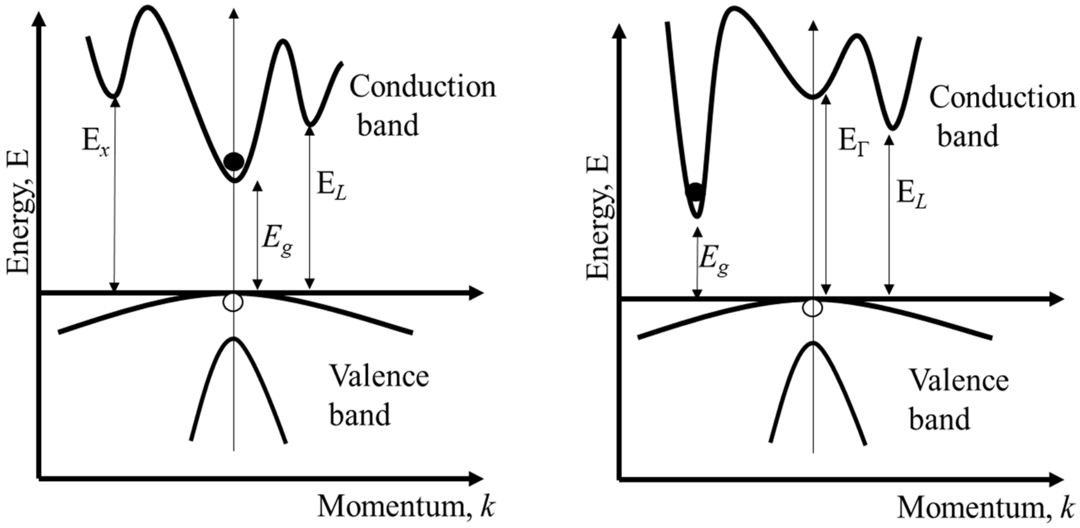

Figure 2.9. Examples of band structure for GaAs(left) and Si(Right)

It is important to note that electrons and holes transition between the valence and conduction bands are energy and momentum conserved. The minimum amount of photon energy must be larger than the energy difference between the valence band maxima and conduction band minima to enable the excitation of electrons and holes. This difference is generally defined as the semiconductor material's bandgap, which is closely related to the cut-off wavelength stated in equation 2.24. For example, in the GaAs shown in Figure 2.9 (left), there is no change in momentum since the conduction band minima are aligned with the maximum point of valence band in the Γ-valley of the Brillouin zone. The photoexcitation effect will happen if the photon energy hv is larger than E_g. However, this process is different in indirect bandgap material such as Si, as shown in Figure 2.9 (right). The phonons must interact with the photons to simultaneously meet the momentum and energy conversation. The probability of the photoexcitation process is therefore higher in direct bandgap materials than indirect bandgap materials.

Plotting the γ^2 verse E and $\gamma^{0.5}$ versus hv and extrapolating to find the horizontal intercept can determine the bandgap of direct and indirect bandgaps of a material since the absorption coefficients can be expressed as follows [29].

$$\begin{aligned} \gamma &\propto \left(hf - E_g\right)^{\frac{1}{2}} \quad , hv \geq E_g \\ \gamma &= 0 \quad , hv < E_g \end{aligned} \tag{2.26}$$

$$\begin{aligned} \gamma &\propto \left(hf - E_g \mp \hbar\Omega\right)^{2} \quad , hv \geq E_g \\ \gamma &= 0 \quad , hv < E_g \end{aligned} \tag{2.27}$$

Where $\mp\hbar\Omega$ is the phonon absorption and emission.

There have been many efforts to improve the responsivity in semiconductor materials to overcome the effects of surface recombination, the reflection of the light and minority carrier recombination. Several recombination processes include band to band, trap-assisted and auger recombination, which are opposed to the photoexcitation process. At short wavelengths, most carriers are created near the surface, and the carriers created can recombine with the traps, dangling bonds[30]. The absorption profile may vary depending on the absorption coefficient, as stated in equation 2.25. Only carriers in the electric field region contribute to the photocurrent, and carriers created outside the electric field region must diffuse into the high field region before recombining. The diffusion process is a function of crystal quality and life time [31], temperature [32], band structure [33] and doping concentration [32].

Figure 2.10 shows an example of an absorption profile based on the absorption coefficient at a given wavelength. In a p-i-n structure, the total photocurrent consists of electrons diffused from the p^+ cladding layer, holes from the n^+ cladding layer and electron-hole pairs generated in the *i*-region (all the carriers are swept by the electric field). However, the diffusion length (minority carrier lifetime) can vary the contribution of electrons from the p^+ cladding layer and holes from the n^+ cladding layer. The external quantum efficiency results can be fitted by a 1-D quantum efficiency model based on current-continuity equation[34].

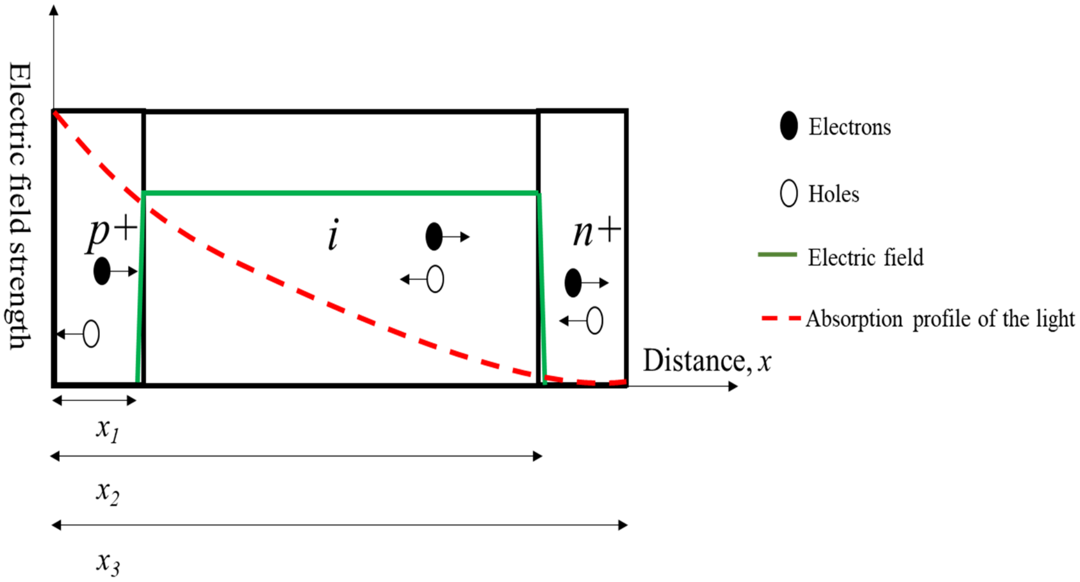

Figure 2.10: A schematic diagram to show how electrons and holes move in the p-i-n structure under illumination.

The quantum efficiency (η_1) due to electrons diffused from the p^+ layer is:

$$\eta_1 = \left(\frac{\gamma L_e}{\gamma^2 L_e^2 - 1}\right) \left[\frac{\frac{S_e L_e}{D_e} + \gamma L_e - \exp(-\gamma X_1)\left(\frac{S_e L_e}{D_e}\cosh\frac{X_1}{L_e} + \sinh\frac{X_1}{L_e}\right)}{\frac{S_e L_e}{D_e}\sinh\frac{X_1}{L_e} + \cosh\frac{X_1}{L_e}} - \gamma L_e \exp(-\gamma X_1)\right] \tag{2.28}$$

The quantum efficiency (η_3)due to holes diffused from the n^+ cladding layer is:

$$\eta_3 = \left(\frac{\gamma L_h}{\gamma^2 L_h^2 - 1}\right) \exp\left[-\gamma(X_3 - X_2)\right] \left[\gamma L_h - \frac{\frac{S_h L_h}{D_h}\left[\cosh\frac{X_3}{L_h} - \exp(-\gamma X_3)\right] + \sinh\frac{X_3}{L_h} + \gamma L_h \exp(-\gamma X_3)}{\frac{S_h L_h}{D_h}\sinh\frac{X_3}{L_h} + \cosh\frac{X_3}{L_h}}\right]\Bigg] \tag{2.29}$$

The quantum efficiency (η_2) due to electron-hole pairs generated in the *i*-region is:

$$\eta_2 = \exp(-\gamma X_1)\{1 - \exp[-\gamma(X_2 - X_1)]\} \tag{2.30}$$

The minority carrier diffusion length is a function of lifetime which can be represented as

$$L_e = \sqrt{D_e \tau_e} \tag{2.31}$$

$$L_h = \sqrt{D_h \tau_h} \tag{2.32}$$

Where S_e and S_h are the surface recombination velocities for electrons and holes, respectively. $\mathrm{D_e}$ and $\mathrm{D_h}$ are the minority electron and hole lifetimes. x_1, x_2 and x_3 are stated in Figure 2.10, which are the distances from the top surface to the top of the depletion edge, the distance between the surface to the bottom depletion edge, and the total thickness of the device.

The total internal quantum efficiency (η_t) is the sum of all.

$$\eta_t = \eta_1 + \eta_2 + \eta_3 \tag{2.33}$$

By taking the reflection of the light into account, the external quantum efficiency (η_{eqe}) is

$$\eta_{eqe} = (1-\mathrm{R_f})\eta_t \tag{2.34}$$

Where $\mathrm{R_f}$ is the reflectivity[34]

2.4.3 Response speed and bandwidth

The response speed depends on the drift velocity in the depletion region, diffusion of carriers and the capacitance of the depletion region. Carriers created outside the electric field region need to diffuse into the junction. Junctions that are close to the surface can help reduce the transit time caused by diffusion. Carriers generated inside the depletion region will drift at their saturation velocity with sufficient reverse bias. The depletion region needs to be thin to avoid the transit-time limitation but not so thin that high excessive capacitance results in a large RC time constant. For APD, the α/β ratio can vary the avalanche build-up time, and the α/β ratio is a function of the electric field. It is important to find the optimal thickness so that the α/β ratio at the electric field is large but does not compromise the transit time. The transit time limited -3dB bandwidth can be defined as [35]

$$f_{\text{transit}} \approx 0.45 \times \frac{v_s}{d} \tag{2.35}$$

Where v_s is the saturation velocity of electrons and holes, and d is the depletion width.

The corresponding RC-limited bandwidth is given by

$$f_{RC} = \frac{1}{2\pi RC} = \frac{d}{2\pi R\varepsilon A} \propto \frac{d}{(R_S+R_L)A} \tag{2.36}$$

Where ε is the dielectric constant of the intrinsic region and R_s is the series resistance, R_L is the load resistance, d is the depletion width and A is area of the device.

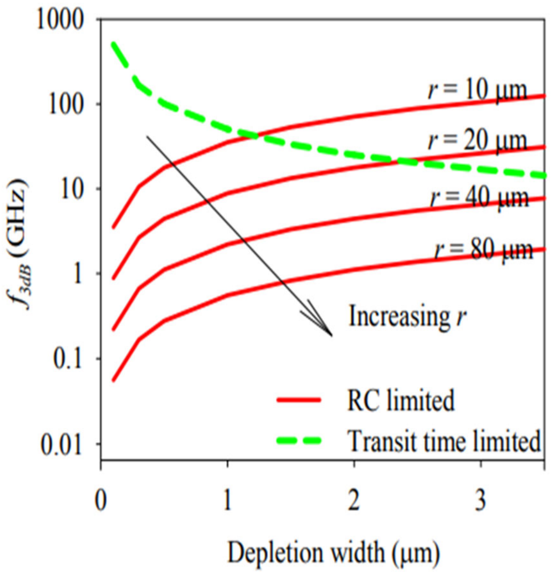

Figure 2.11: -3dB transit time and RC limited bandwidth for APD with different device size

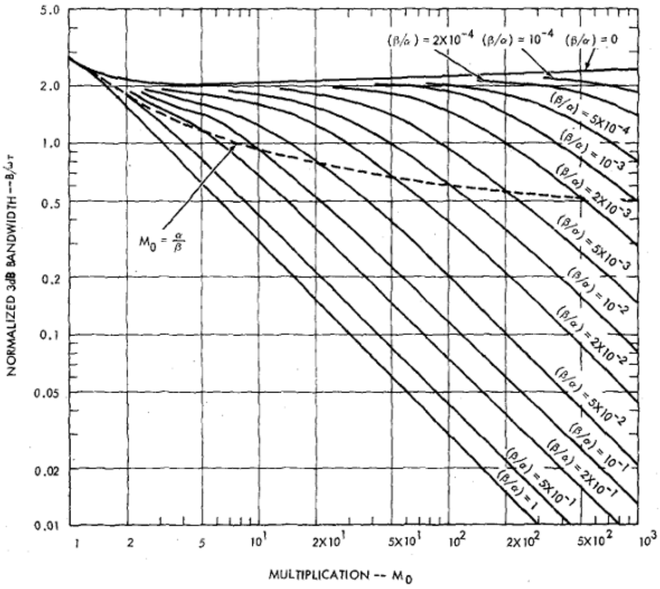

Figure 2.12: APD bandwidth variation with different *α/β* ratio [36]

As shown in Figure 2.11, there is a trade-off between the device size and transit time in the APDs, assuming R_L is 60Ω and R_S is 10Ω(assume R_s is the same in different size devices), and the device's size varies in radius (*r*) from 10 to 80μm.

However, the transit time limited bandwidth can no longer be characterized by equation 2.35 since the avalanche multiplication requires multiple transits to build up. Therefore, the multiplication decreases with the increase of frequency, and the relationship can be expressed as [36]

$$M(\omega) = M_0[1 + (\omega\tau M_0)^2]^{-1/2} \tag{2.37}$$

Where M_0 is the avalanche multiplication at low operating frequency, ω is the operating frequency, and τ is the effective transit time in the avalanche region which varies with the *α/β* ratio.

Because of the trade-off between the avalanche multiplication and operating frequency, a new Figure of merit, gain-bandwidth product (GBP), is now used to estimate the APD response speed [37]. For APDs, the transit time has a strong dependence on the α/β ratio, and the larger α/β ratio will be preferable to have a higher GBP, as shown in Figure 2.12. In addition, the effect of dead space on bandwidth has been studied by using the RPL model [38]. It showed that the bandwidth is reduced when dead space is considered since it requires more multiplication transit to reach a specific multiplication value.

2.4.4 Temperature dependence of APDs

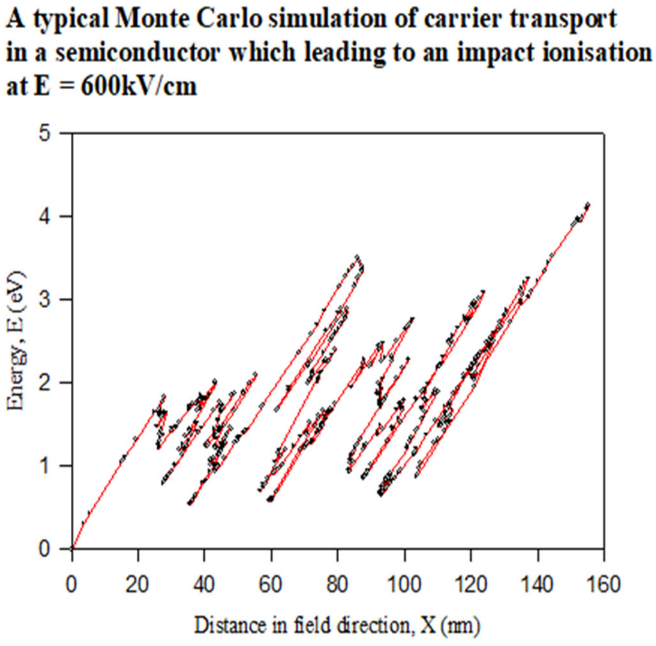

Figure 2.13: Carrier energy gain and lose travelling at direction of *x* at saturation velocity.

Impact ionization occurs when electrons and holes travel at high electric field and gain sufficient energy. As a result of impact ionization process, avalanche multiplication happens. This process can be highly temperature dependent. For impact ionization, electrons and holes must acquire the threshold energy by traversing in the high field multiplication region for ionization. This threshold energy depends on the bandgap energy (E_g) [39], which is only weakly dependent on temperature [40]. As shown in

Figure 2.13, prior to an impact ionization event, carriers travelling in an electric-field gain and lose kinetic energy due to various scattering processes [41]. If the material is an alloy, then alloy scattering will also be present. Each scattering process also results in a small loss in energy. This scattering will increase the distance a carrier travels in an electric field before it gains sufficient energy to impact ionize. Of these, phonon scattering is the most temperature-dependent process and can make the overall avalanche multiplication factor highly temperature sensitive.

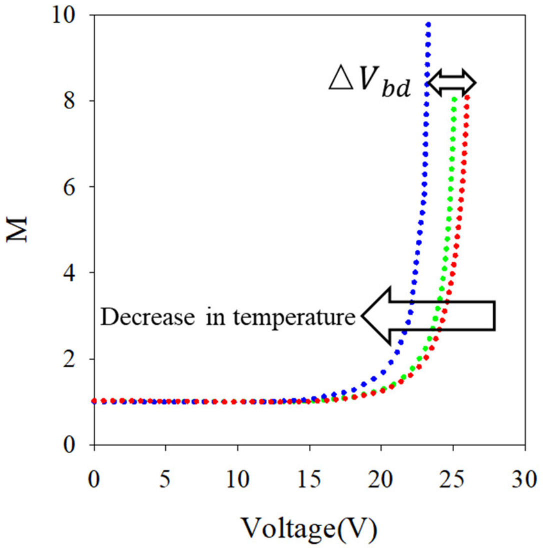

Figure 2.14: Temperature dependence of multiplication in APD device

It is important to understand the temperature dependence characteristic in linear mode avalanche multiplication and hence the sensitivity of an APD receiver module. In addition, breakdown voltage and over bias in a Geiger mode APD does not change with temperature, an active variable bias circuit is sometimes required to modify the reverse bias voltage across the device as the temperature changes [42]. Alternatively, the temperature must be regulated by an embedded thermoelectric cooler (TEC) and temperature sensor for temperature stabilization [43]. It is favorable to have APD is made of a material which has a weakly temperature dependent ionization process and a small breakdown voltage temperature coefficient (C_{bd}) since both active bias circuit and TEC add extra complexity and cost to the receiver modules.

$$C_{bd} = \Delta V_{bd}/\Delta T \quad (2.38)$$

Where ΔV_{bd} is the change in breakdown voltage and ΔT is the temperature difference. The C_{bd} Values are material dependent and can be significant in Silicon APDs and InGaAs APDs.

2.5 Modelling

2.5.1 Random path length model (RPL)

The random path length model describes the behavior of a carrier in a region of a given electric field, characterized by an ionization path length probability density function (PDF), *h(x)*. This shows the probability of the carrier after moving a distance *x* from where it was created at position x_0, and this is given as [44]:

$$h_e(x) = \begin{cases} 0 & \text{for } x < d_e \\ \alpha^* \exp[-\alpha^*(x - d_e)] & \text{for } x \geq d_e \end{cases} \quad (2.39)$$

$$h_h(x) = \begin{cases} 0 & \text{for } x < d_h \\ \beta^* \exp[-\beta^*(x - d_h)] & \text{for } x \geq d_h \end{cases} \quad (2.40)$$

Where electrons are travelled in the *x* direction and holes in the opposite direction(*-x*), d_e and d_h are the 'hard' dead space that a carrier needs to travel to obtain sufficient energy for impact ionization.

$$d_e = \frac{E_{the}}{\xi} \text{ and } d_h = \frac{E_{thh}}{\xi} \quad (2.41)$$

Where E_{the} and E_{thh} are the ionization threshold energy of electrons and holes, ξ is the electric field strength, and $\alpha^*$and $\beta^*$are effective ionization coefficients for electrons and holes.

$$\frac{1}{\alpha} = d_e + \frac{1}{\alpha^*} \text{ and } \frac{1}{\beta} = d_h + \frac{1}{\beta^*} \quad (2.42)$$

When a carrier travels within a distance *x*, the probability of ionizing is given by integrating the PDF from x_0+d_e to *x*,

$$G_e(x_0 < x' < x) = \begin{pmatrix} 0 & , x - x_0 < d_e \\ 1 - \exp\left[-\alpha^*(x - d_e)\right] & , x - x_0 \geq d_e \end{pmatrix} \tag{2.43}$$

By rearranging equation 2.42, the probability of electrons not ionizing, S_e is defined as:

$$S_e(x_0 < x' < x) = \begin{pmatrix} 1 & , x - x_0 < d_e \\ \exp\left[-\alpha^*(x - d_e)\right] & , x - x_0 \geq d_e \end{pmatrix} \tag{2.44}$$

By using a random number *r* (from 0 to 1) to substitute S_e,

$$x_e = d_e - \frac{\ln(r)}{\alpha^*} \text{ and } x_h = d_h - \frac{\ln(r)}{\beta^*} \tag{2.45}$$

Where *r* is a randomly generated number with uniform distribution, x is the distance a carrier must travel for its first ionization. Mapping *r* to the corresponded discrete cumulative distribution function to select the random ionization path length in the case of PDFs calculated from the SMC model. These CDF profiles are incorporated into the RPL model. Using a simple linear interpolation, the ionization path lengths from values of *r* fall between two discrete data points in the look-up table. In each trial, all carriers' positions of impact ionization are recorded until there is no carrier in the avalanche region. Many trails (with N representing the number of trials) are performed to achieve reliable simulation results. Multiplication (*M*) and excess noise factor (*F*) can be defined as a function of *x*:

$$M(x_0) = \frac{1}{N} \sum_{N=1}^{N} M_N \tag{2.46}$$

and

$$F(x_0) = \frac{1}{NM^2(x_0)} \sum_{N=1}^{N} M_N^2 \tag{2.47}$$

2.5.2 Monte Carlo model (MC)

The Monte Carlo model has the capacity to generate the most realistic simulation of high field carrier transportation events but has very long computation times. Hayat et al. [45] have shown that the recursive technique can generate the multiplication and excess noise based on the ionization path length PDF from both thin and thick structures. The RPL model was introduced by Ong et al. [46] and successful reproduced the multiplication and excess noise characteristics based on the randomly chosen ionization path length to calculate the ionization probability of a carrier in a thick device using displaced ionization path length PDFs within an MC framework. Due to the complicated and time-consuming nature of the MC model, the RPL model will be the main simulation tool used in this work to help with analysis.

2.6 References

[1] M. Thomas, "Semiconductors — basic data, 2nd ed. Edited by O. Madelung, Springer, Berlin 1996, viii, 317 pp., hardcover, DM 88.00, ISBN 3-540-60883-4," *Chem. Vap. Depos.*, vol. 3, no. 5, pp. 288–289, Oct. 1997, doi: https://doi.org/10.1002/cvde.19970030508.

[2] P. A. Wolff, "Theory of electron multiplication in silicon and germanium," *Phys. Rev.*, vol. 95, no. 6, pp. 1415–1420, 1954, doi: 10.1103/PhysRev.95.1415.

[3] C. L. Anderson and C. R. Crowell, "Threshold energies for electron-hole pair production by impact ionization in semiconductors," *Phys. Rev. B*, vol. 5, no. 6, pp. 2267–2272, 1972, doi: 10.1103/PhysRevB.5.2267.

[4] O. Madelung, *Semiconductors--basic Data*. Springer, 1996.

[5] S. Adachi, *Properties of Semiconductor Alloys: Group-IV, III-V and II-VI Semiconductors*. 2009.

[6] J. Bude and K. Hess, "Thresholds of impact ionization in semiconductors," *J. Appl. Phys.*, vol. 72, no. 8, pp. 3554–3561, 1992, doi: 10.1063/1.351434.

[7] J. Allam, "'Universal' dependence of avalanche breakdown on bandstructure: Choosing materials for high-power devices," *Japanese J. Appl. Physics, Part 1 Regul. Pap. Short Notes Rev. Pap.*, vol. 36, no. 3 SUPPL. B, pp. 1529–1542, 1997, doi: 10.1143/jjap.36.1529.

[8] B. F. Aull *et al.*, "Geiger-Mode Avalanche Photodiodes for Three- Dimensional Imaging," *Lincoln Lab. J.*, vol. 13, no. 2, pp. 335–350, 2002, [Online]. Available: http://www.ll.mit.edu/publications/journal/pdf/vol13_no2/13_2geigermode3d.pdf.

[9] J. S. L. Ong, J. S. Ng, A. B. Krysa, and J. P. R. David, "Temperature dependence of avalanche multiplication and breakdown voltage in Al0.52In0.48P," *J. Appl. Phys.*, vol. 115, no. 6, pp. 0–6, 2014, doi: 10.1063/1.4865743.

[10] X. Jin *et al.*, “Temperature Dependence of the Impact Ionization Coefficients in AlAsSb Lattice Matched to InP,” *IEEE J. Sel. Top. Quantum Electron.*, vol. 28, no. 2, 2022, doi: 10.1109/JSTQE.2021.3099912.

[11] Y. Yuan *et al.*, “Temperature dependence of the ionization coefficients of InAlAs and AlGaAs digital alloy: erratum,” *Photonics Res.*, vol. 7, no. 3, p. 273, 2019, doi: 10.1364/prj.7.000273.

[12] A. G. Chynoweth, “Ionization Rates for Electrons and Holes in Silicon,” *Phys. Rev.*, vol. 109, no. 5, pp. 1537–1540, Mar. 1958, doi: 10.1103/PhysRev.109.1537.

[13] W. N. Grant, “Electron and hole ionization rates in epitaxial silicon at high electric fields,” *Solid State Electron.*, vol. 16, no. 10, pp. 1189–1203, 1973, doi: 10.1016/0038-1101(73)90147-0.

[14] G. E. Stillman and C. M. Wolfe, “Chapter 5 Avalanche Photodiodes**This work was sponsored by the Defense Advanced Research Projects Agency and by the Department of the Air Force.,” in *Semiconductors and Semimetals*, vol. 12, R. K. Willardson and A. C. B. T.-S. and S. Beer, Eds. Elsevier, 1977, pp. 291–393.

[15] S. A. Plimmer, J. P. R. David, D. S. Ong, and K. F. Li, “A simple model for avalanche multiplication including deadspace effects,” *IEEE Trans. Electron Devices*, vol. 46, no. 4, pp. 769–775, 1999, doi: 10.1109/16.753712.

[16] S. A. Plimmer, C. H. Tan, J. P. R. David, R. Grey, K. F. Li, and G. J. Rees, “The effect of an electric-field gradient on avalanche noise,” *Appl. Phys. Lett.*, vol. 75, no. 19, pp. 2963–2965, 1999, doi: 10.1063/1.125202.

[17] S. A. Plimmer, J. P. R. David, and D. S. Ong, “The merits and limitations of local impact lonization theory,” *IEEE Trans. Electron Devices*, vol. 47, no. 5, pp. 1080–1088, 2000, doi: 10.1109/16.841244.

[18] G. E. Bulman, V. M. Robbins, and G. E. Stillman, “The Determination of Impact Ionization Coefficients in (100) Gallium Arsenide Using Avalanche Noise and Photocurrent Multiplication Measurements,” *IEEE Trans. Electron Devices*, vol. 32, no. 11, pp. 2454–2466, 1985, doi: 10.1109/T-ED.1985.22295.

[19] S. A. Plimmer *et al.*, “Investigation of impact ionization in thin GaAs diodes,” *IEEE Trans. Electron Devices*, vol. 43, no. 7, pp. 1066–1072, 1996, doi: 10.1109/16.502416.

[20] M. M. Hayat, W. L. Sargeant, and B. E. A. Saleh, “Effect of Dead Space on Gain and Noise in Si and GaAs Avalanche Photodiodes,” *IEEE J. Quantum Electron.*, vol. 28, no. 5, pp. 1360–1365, 1992, doi: 10.1109/3.135278.

[21] R. J. McIntyre, “Multiplication noise in uniform avalanche diodes,” *IEEE Trans. Electron Devices*, vol. ED-13, no. 1, pp. 164–168, 1966, doi: 10.1109/T-ED.1966.15651.

[22] M. C. Teich, “Signal-to-Noise Ratio for Lightwave Systems using Avalanche Photodiodes,” *J. Light. Technol.*, vol. 9, no. 3, pp. 318–320, 1991, doi: 10.1109/50.70006.

[23] B. E. A. Saleh, M. M. Hayat, and M. C. Teich, “Effect of Dead Space on the Excess Noise Factor and Time Response of Avalanche Photodiodes,” *IEEE Trans. Electron Devices*, vol. 37, no. 9, pp. 1976–1984, 1990, doi: 10.1109/16.57159.

[24] G. G. Macfarlane and V. Roberts, “Infrared Absorption of Germanium near the Lattice Edge,” *Phys. Rev.*, vol. 97, no. 6, pp. 1714–1716, Mar. 1955, doi: 10.1103/PhysRev.97.1714.2.

[25] D. E. Aspnes and A. A. Studna, “Dielectric functions and optical parameters of Si, Ge, GaP, GaAs, GaSb, InP, InAs, and InSb from 1.5 to 6.0 eV,” *Phys. Rev. B*, vol. 27, no. 2, pp. 985–1009, Jan. 1983, doi: 10.1103/PhysRevB.27.985.

[26] H. Burkhard, H. W. Dinges, and E. Kuphal, “Optical properties of In1−xGaxP1−yAsy, InP, GaAs, and GaP determined by ellipsometry,” *J. Appl. Phys.*, vol. 53, no. 1, pp. 655–662, Jan. 1982, doi: 10.1063/1.329973.

[27] X. Yi, “Impact ionization in AlAsSb,” University of Sheffield, 2020.

[28] Y. Yuan, J. Zheng, A. K. Rockwell, S. D. March, S. R. Bank, and J. C. Campbell, “AlInAsSb Impact Ionization Coefficients,” *IEEE Photonics Technol. Lett.*, vol. 31, no. 4, pp. 315–318, 2019, doi: 10.1109/LPT.2019.2894114.

[29] W. B. Steward and H. H. Nielsen, “The infrared absorption spectrum of germane,” *Phys. Rev.*, vol. 48, no. 11, pp. 861–864, 1935, doi: 10.1103/PhysRev.48.861.

[30] J. P. Zheng, L. Shi, F. S. Choa, P. L. Liu, and H. S. Kwok, “Intensity-dependent photoluminescence spectra of semiconductor-doped glasses,” *Appl. Phys. Lett.*, vol. 53, no. 8, pp. 643–645, Aug. 1988, doi: 10.1063/1.100396.

[31] D. K. Schroder, “Carrier Lifetimes in Silicon,” vol. 44, no. 1, pp. 160–170, 1997.

[32] S. S. Li and W. R. Thurber, “THE DOPANT DENSITY AND TEMPERATURE DEPENDENCE OF ELECTRON MOBILITY AND RESISTIVITY IN n-TYPE SILICON ’ t ",” vol. 20, pp. 609–616, 1977.

[33] and K. J. V. H. A. Zarem, J. A. Lebens, K. B. Nordstrom, P. C. Sercel, S. Sanders, L. E. Eng, A. Yariv, “Effect of Al mole fraction on carrier diffusion lengths and lifetimes in AlxGa1−xAs,” *Appl. Phys. Lett1*, vol. 55, no. 25, pp. 2622–2624, 1989.

[34] M. I. Yernaux, C. Battochio, P. Verlinden, and F. Van De Wiele, “A one-dimensional model for the quantum efficiency of front-surface-field solar cells,” *Sol. Cells*, vol. 13, no. 1, pp. 83–97, 1984, doi: https://doi.org/10.1016/0379-6787(84)90095-4.

[35] J. Bowers and C. Burrus, “Ultrawide-band long-wavelength p-i-n photodetectors,” *J. Light. Technol.*, vol. 5, no. 10, pp. 1339–1350, 1987, doi: 10.1109/JLT.1987.1075419.

[36] R. B. Emmons, “Avalanche-Photodiode Frequency Response,” *J. Appl. Phys.*, vol. 38, no. 9, pp. 3705–3714, Aug. 1967, doi: 10.1063/1.1710199.

[37] X. G. Zheng *et al.*, “Avalanche Photodiode Array,” vol. 38, no. 11, pp. 1536–1540, 2002, doi: 10.1109/JQE.2002.804297.

[38] J. S. Ng *et al.*, “Effect of dead space on avalanche speed [APDs],” *IEEE Trans. Electron Devices*, vol. 49, no. 4, pp. 544–549, 2002, doi: 10.1109/16.992860.

[39] K. Yeom, J. M. Hinckley, and J. Singh, “Theoretical study on threshold energy and impact ionization coefficient for electrons in Si1-xGex,” *Appl. Phys. Lett.*, vol. 64, no. 22, pp. 2985–2987, 1994, doi: 10.1063/1.111379.

[40] P. Varshni, “Temperature dependence of the energy gap in semiconductors,” pp. 2–7, 1967.

[41] M. V Fischetti, “Monte Carlo Simulation of Transport in Technologically Significant Semiconductors of the Diamond and Zinc-Blende Structures-Part I : Homogeneous Transport,” vol. 38, no. 3, 1991.

[42] S. Deng, A. P. Morrison, and J. Hayes, “A bias and control circuit for gain stabilization in avalanche photodiodes,” pp. 37–37, 2013, doi: 10.1049/ic.2012.0187.

[43] Princeton lightwave, “PAR Series - High Sensitivity APD Front End Receiver Modules,” pp. 1–3, 2016, [Online]. Available: https://sphotonics.ru/upload/iblock/be0/par_series_high_sensitivity_apd_front_end_receiver_modules.pdf.

[44] D. S. Ong, K. F. Li, G. J. Rees, J. P. R. David, and P. N. Robson, “A simple model to determine multiplication and noise in avalanche photodiodes,” *J. Appl. Phys.*, vol. 83, no. 6, pp. 3426–3428, Mar. 1998, doi: 10.1063/1.367111.

[45] M. M. Hayat *et al.*, “Gain-bandwidth characteristics of thin avalanche photodiodes,” *IEEE Trans. Electron Devices*, 2002, doi: 10.1109/16.998583.

[46] D. S. Ong, K. F. Li, G. J. Rees, G. M. Dunn, J. P. R. David, and P. N. Robson, “A monte carlo investigation of multiplication noise in thin p+-i-n+ GaAs avalanche photodiodes,” *IEEE Trans. Electron Devices*, vol. 45, no. 8, pp. 1804–1810, 1998, doi: 10.1109/16.704382.

Chapter 3:

Experimental techniques

3.1 Electrical characterisation details

3.1.1 Current-voltage (I-V) measurements

The forward and reverse dark current-voltage (I-V) measurements are performed using an HP4140B picoammeter or a Keithley 236/237 source measure unit (SMU), controlled by Labview software. The HP4140B and Keithley SMU can measure the resulting current value while applying a bias voltage to the diode. The I-V characteristic of a device can provide helpful information like breakdown voltage (V_{bd}), leakage current (I_s), bulk dark current (I_b), series resistance (R_s), and ideality factor (n). I-V measurements can provide helpful information as a measure of fabrication techniques and material quality. I-V measurements are usually the most fundamental characterization.

The bulk dark current is generally due to tunnelling and generation-recombination, and generally scales with the area. In contrast, surface leakage current can vary with the leakage paths around the mesa periphery and scales with the perimeter. The contribution of the bulk dark current and surface leakage current can be measured by normalizing the dark current to the device area (1) and (2) perimeter.

$$J_{\text{Area}} = \frac{I_{dark}}{\pi r^2} \tag{3.1}$$

$$J_{\text{Perimeter}} = \frac{I_{dark}}{2\pi r} \tag{3.2}$$

Where r is the radius of the device.

Information such as material quality, junction formation and contact resistance can be obtained by performing dark forward I-V measurements. The forward IV of an ideal diode with no series resistance can be described as[1]:

$$I_F = I_o\left[exp\left(\frac{qV_t}{nk_BT}\right) - 1\right] \tag{3.3}$$

Where I_o is the saturation current, which is a function of cladding layer doping level and diffusion length of electrons and holes, V_t is the total voltage applied to the device including built-in voltage and applied bias, q is the electronic charge, T is the temperature in Kelvin, k_B is Boltzmann's constant, and n is the ideality factor.

$$I_F = I_o\left[exp\left(\frac{q(V_t-IR)}{nk_BT}\right) - 1\right] \tag{3.4}$$

Equation 3.3 assumes that there is no series resistance in the diode whereas equation 3.4 takes series resistance into consideration. An ideality factor closes to 1 means that the carrier transportation is diffusion-dominated. In contrast, n close to 2 is generation-recombination and usually indicates this material has high defects (trap level in the mid-band states), as shown in Figure 3.1. The forward current bends over because of the effect of series resistance.

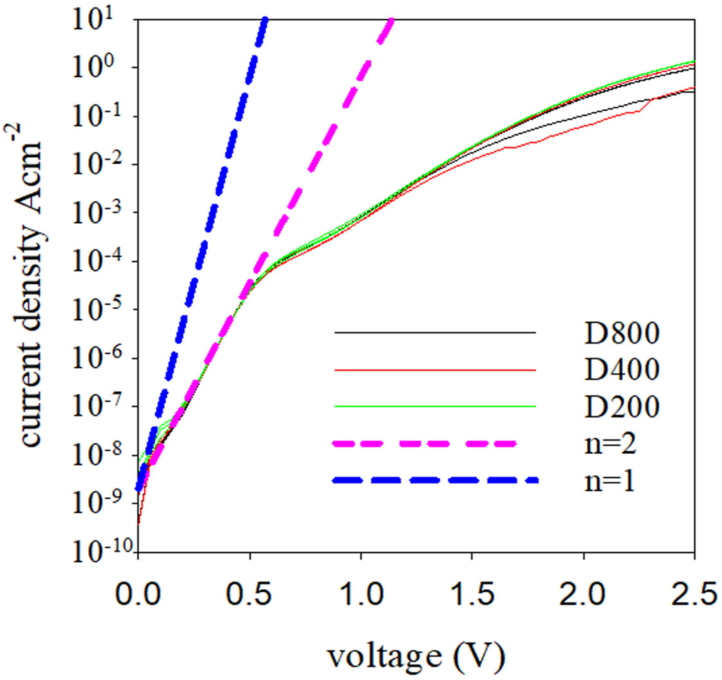

Figure 3.1: A diagram to show ideality factor fitting and series resistance effects for three different size devices.

Figure 3.1 shows an example of forward bias current density measurements on different size APD devices. It scales with area but also exhibits strong series resistance. This characteristic can be described by equation 3.4. For low series resistance device, there is no power dependent on the multiplication characteristic (multiplication at a given voltage are the same with high and low power). However, high resistance can also limit the photocurrent measurements since there will be a large voltage drop across the resistor, which will reduce the electric field applied to the avalanche region. This will limit the maximum achievable multiplication, as shown in Figure 3.2, and impose an RC-time limit.

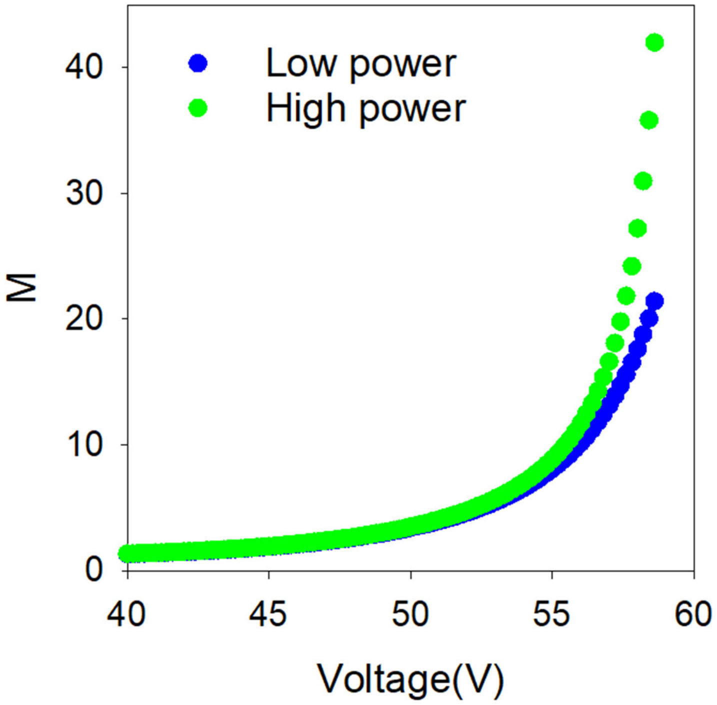

Figure 3.2： multiplication characteristic for III-V APD with high series resistance under different illumination power

It is important to understand that the source of series resistance, *R,* is primarily due to the contact resistance between the metal and semiconductor. The contact resistance can be significantly reduced by increasing the cladding layer doping and selecting appropriate metals as the *p* and *n*-type contacts with the help of annealing.

A transmission line model (TLM) is often used to evaluate the resistivity of the top metal contact on devices. There are various factors can affect the resistivity, including doping density, the density of states in the semiconductor and the work function of the metal contact. On the APD mask, there are $100\times50\mu m^2$ metal pads for top and bottom contacts. The resistance between adjacent metal pads with varied spacings are measured.

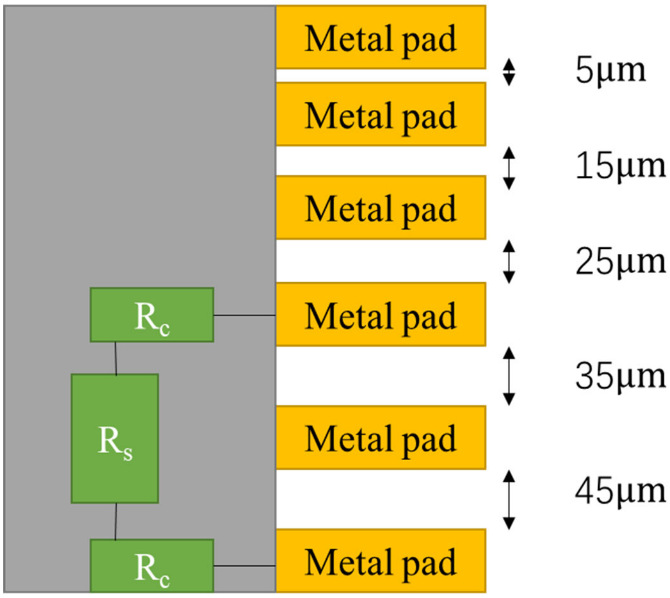

Figure 3.3: A schematic diagram of the metal pattern

As illustrated in Figure 3.3, the total resistance is the sum of two metal contact resistances (R_c), system resistance (R_{sys}), and semiconductor (R_s).

$$R_{\text{tot}} = R_{\text{sys}} + 2R_c + R_{\text{s}} \tag{3.5}$$

R_{tot} is measured with different spaces between metal pads, and is found to increase with an increase in the spacing distance. R_c can be found, as shown in Figure 3.4, by plotting R_{tot} versus distance and extrapolating to the intersect with the y-axis, at which $R_s = 0$ and therefore $R_{\text{tot}} = R_{\text{sys}} + 2R_c$. The R_{sys} can be measured by short-circuiting and is measured to be around 3Ω. Since $R = \frac{\rho L}{A}$, the resistance is proportional to the resistivity (ρ) and length (L) and inversely proportional to the area (A), the resistivity can be obtained by multiplying the R_c and metal pad area $100\times50\mu m^2$. This process can be performed on both top and bottom contact to identify where the series resistance originates.

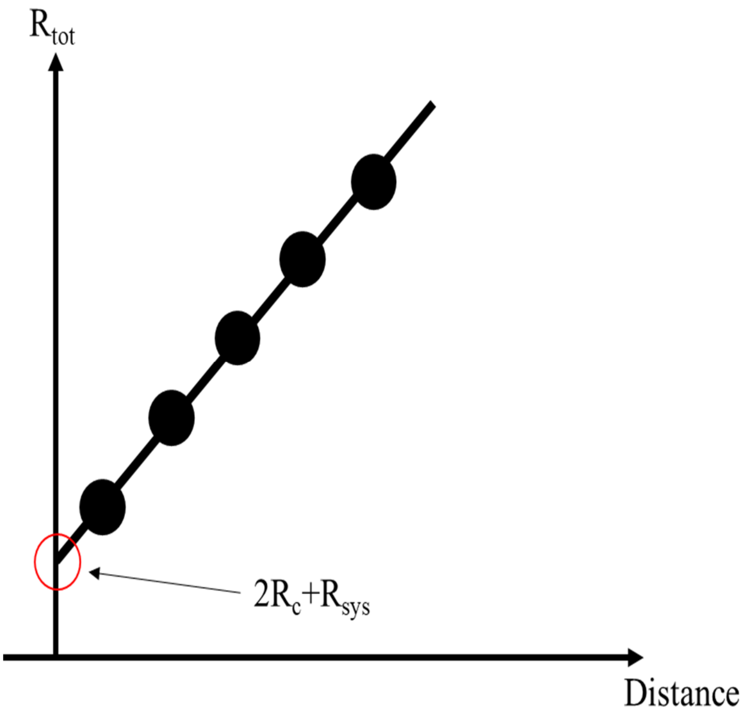

Figure 3.4: The relationship between metal pads distance and total series resistance

As a function of reverse bias, a few mechanisms will occur that can lead to an increase of dark current which then degrade the SNR of an APD. Mainly, this process includes generation and recombination ($I_{G\text{-}R}$), diffusion (I_{diff}) and band to band tunnelling (I_{tunn}) and surface leakage (I_{surf}). These are expressed as follows[1]:

$$I_{diff} = I_o\left[exp\left(\frac{qV}{k_BT}\right) - 1\right] \tag{3.6}$$

$$I_{G-R} = \frac{qn_iAw}{\tau_{eff}} \tag{3.7}$$

$$I_{\text{tunn}} = \frac{(2m^*)^{0.5}q^3EVA}{4\pi^2\hbar E_g^{0.5}}exp\left(-\frac{\alpha_T(m^*)^{0.5}E_g^{0.5}}{q\hbar E}\right) \tag{3.8}$$

$$I_{surf} = \frac{V}{R} \tag{3.9}$$

Where A is the cross-sectional area, w is the depletion width, n_i is the intrinsic carrier concentration, τ_{eff} is the effective carrier lifetime, m^* is the effective electron mass, $\hbar$ is the reduced Planck constant and α_T is used to describe the shape of the barrier. The surface leakage current is mainly caused by the conduction on the surface of an etched mesa. Equation 3.9 indicates that surface leakage current simply follows Ohm's Law.

3.1.2 Capacitance-voltage(C-V) measurements

The capacitance-voltage (C-V) measurements are performed using an HP4275 LCR meter. The capacitance of the APD device changes with reverse bias measured by superimposing a sinusoidal test signal with an amplitude of 50mV at a frequency of 10KHz, 100KHz, and 1MHz. Two conductors separated by a dielectric will give rise to a capacitance, *C*. The capacitance varies with dielectric constants ε_r, the permittivity of vacuum ε_0, the distance between the two conductors (*W*) and the area of the conductor,

$$C = \frac{\varepsilon_r \varepsilon_0 A}{W} \tag{3.10}$$

The built-in voltage (V_{bi}) can be estimated by plotting 1/C^2 and extrapolating the linear intercept of the 1/C^2 plot. This is only valid on an abrupt single-side junction with constant doping density. The doping density at a given position can be expressed as

$$N(w) = \frac{2}{q\varepsilon_0 \varepsilon_r A^2}\left[\frac{dV}{d\left(\frac{1}{C^2}\right)}\right] \tag{3.11}$$

In a p-i-n diode, the intrinsic region will be depleted by the electric field when the device is reverse biased. The depletion width and doping level can be calculated using an electrostatic model from C-V measurements. Poisson's equation assumes the doping profile is abrupt, and the electric field gradient was expressed as

$$\frac{dE}{dx} = \frac{qN}{\varepsilon_0 \varepsilon_r} \tag{3.12}$$

Where *E* is the electric field, and *N* is the doping density.

The area under the electric field profile curve is the sum of reverse applied voltage (*V*) and (V_{bi}), and the C-V measurements can therefore be fitted to with doping level, the thickness of each layer and the dielectric constant as adjustable parameters.

3.1.3 Photo-response measurements

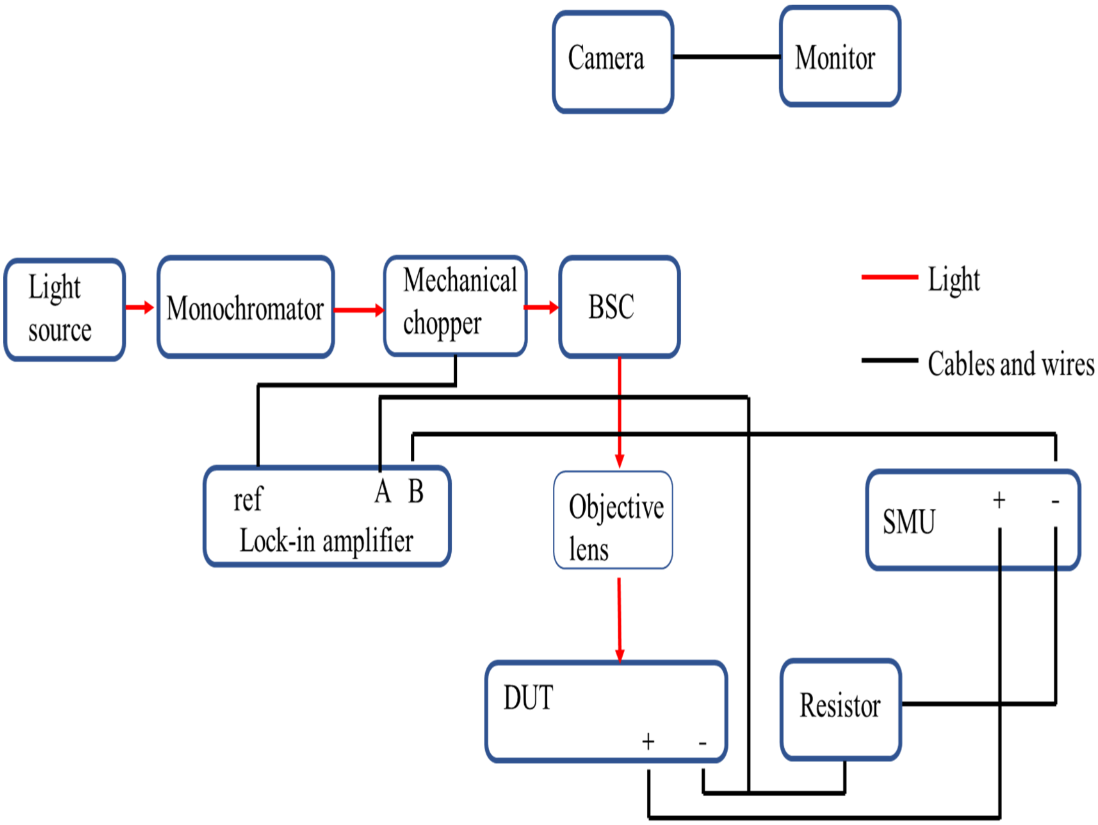

Figure 3.5： Schematic diagram of photo-response measurements set up

Photo-response measurements investigate the optical properties of an APD over a specific range of wavelengths. Figure 3.5 shows a schematic diagram of the photo-response setup. Light comes from a 100W tungsten bulb source and is injected into a monochromator (iHR320) using optical focusing lenses. Light is transmitted through the monochromator grating and the resultant monochromatic light is focused onto the APD under test using further optical lenses. A beam-splitting cube (BSC) is used to image the device and the incident light spot. The light coming out from the monochromator is chopped with a mechanical chopper at a frequency of 180Hz. This phase sensitive detection (PSD) technique utilises an SR830 lock-in amplifier (LIA) to measure the photocurrent by measuring the photovoltage (V_{ph}) drop across the resistor. The modulation frequency from the chopper is fed into the LIA as the reference frequency (f_{ref}). The phase-lock-loop can track f_{ref} actively to ensure the measurements are not affected by the variation of f_{ref}. The LIA only response to the signal associated with that frequency, and a low pass filter can remove other frequencies' signals, detailed will be given in the later section. Either a Hamamatsu silicon photodiode (S5973-02) or a Thorlabs InGaAs photodiode (FD05D) with known responsivity at a given wavelength was used to calculate the output power falling on the device, depending on the relevant wavelength. The following equation can then relate the photovoltage measured through LIA to the photocurrent:

$$I_{ph} = \frac{\frac{LIA}{10} \times \text{sensitivity}}{0.45 \times \text{ resistance}} \tag{3.13}$$

Where LIA is the output value of the lock-in amplifier and resistance is the value of the resistor used in the circuit.

3.1.4 Photo-multiplication measurement

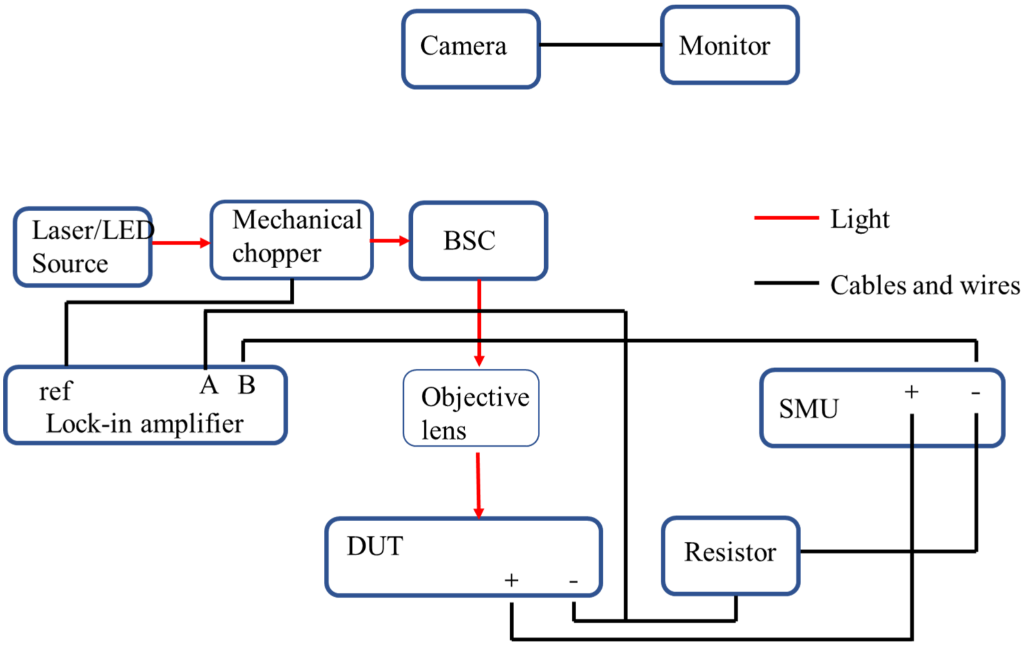

Figure 3.6: A schematic diagram of the photo-multiplication set-up

Carriers can impact ionize, resulting in avalanche multiplication, when subject to a high electric field. It is essential to accurately determine the pure electron and pure hole injection multiplication (M_e and M_h) from p-i-n and n-i-p structures (Figure 3.7) with different thicknesses to cover a wide range of electric field strengths, and therefore calculate the α and β.

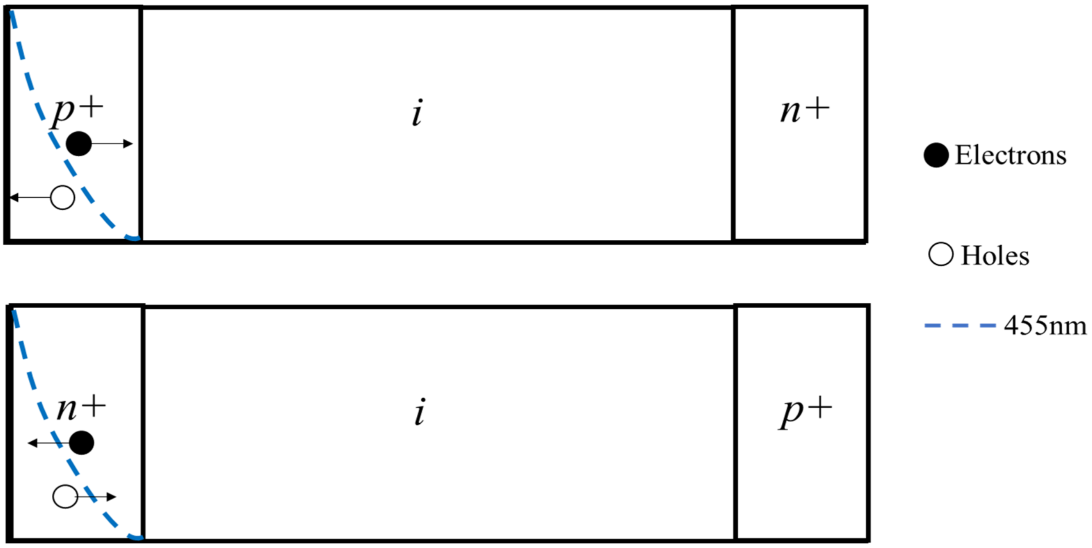

Figure 3.7: Pure injection profile in p-i-n and n-i-p structures

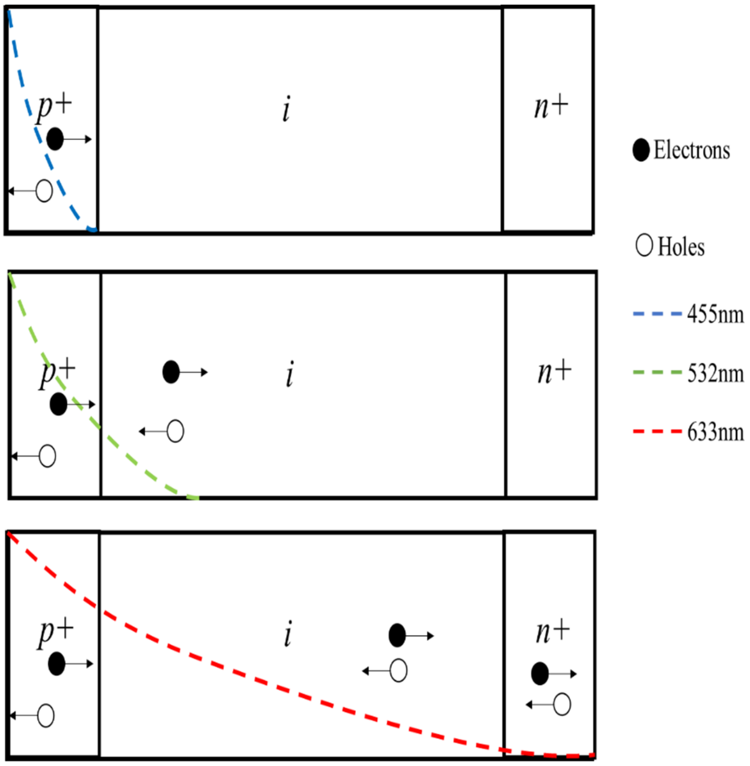

Figure 3.8: A diagram to show carrier transportation under different injection conditions.

A schematic of the photo-multiplication set-up is shown in Figure 3.6. A laser or LED light source was modulated at a frequency of 180Hz to utilize a PSD technique. An SMU was used to bias the device under test. The AC optical signal can then be superimposed with a reference AC signal with the same frequency, and the lock-in amplifier is used to measure the resultant photovoltage signal. The avalanche multiplication factor is calculated as:

$$M(V) = \frac{I_{ph}(V)}{I_{pr}} \tag{3.14}$$

Where $M(V)$ is the multiplication at a given voltage, I_{pr} is the primary photocurrent, and $I_{ph}(V)$ is the photocurrent at a particular reverse bias.

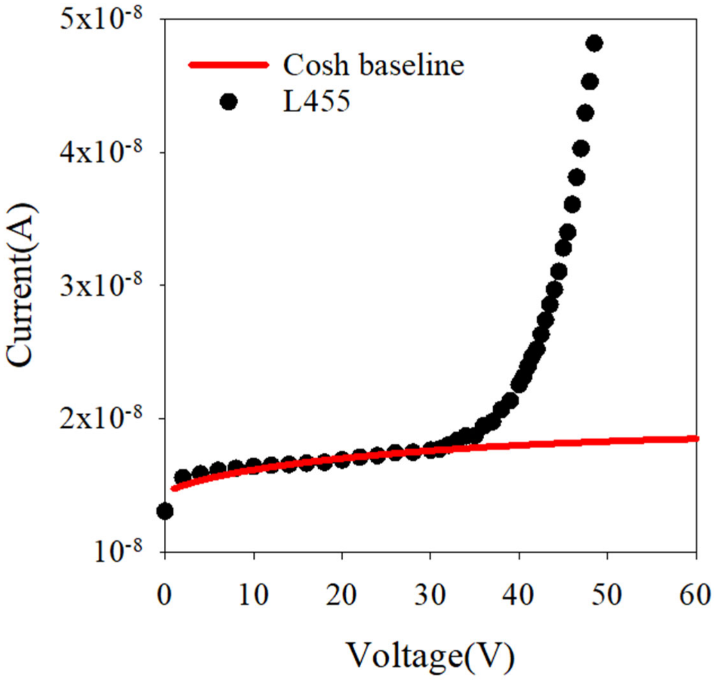

Figure 3.9: A diagram to show total current normalized to primary photocurrent, with Early effect correction.

The avalanche multiplication characteristics were calculated by correcting the total photocurrent (I_{ph}) to the primary photocurrent (I_{pr}) shown in Figure 3.9. Because of the increase in reverse bias, the depletion edge moves closer to the surface, similar to the Early effect in a bipolar junction transistor. Woods et al.[2] described the I_{pr} in an abrupt p-n junction, and an example is shown in the Figure above:

$$I_{pr} = \frac{qG_0}{cosh(L/L_{pn})} \tag{3.15}$$

Where G_0 is an adjustable parameter of carrier photogeneration rate at the cladding region edge, L is the distance between the illuminated surface and the depletion edge at a given voltage, L_{pn} is the minority carrier diffusion length.

Equation 3.15 can be simplified into a linear correction function as:

$$I_{pr} = aV + c \tag{3.16}$$

Where a is an adjustable parameter representing the rate of increasing photocurrent with reverse bias and *c* is the intercept of the *y*-axis.

It is important to choose an appropriate resistor value so that the overall voltage drop on the resistor is <0.1V and the voltage applied on the device will not be affected. Although a larger resistor value can yield a larger photocurrent signal, it can cause problems when the dark current is high, resulting in a large voltage drop across the resistor and reducing the voltage across the APD.

Ideally, the avalanche multiplication is independent of optical power, but in real measurements, this can be a problem when laser power is focused on the device. This can cause the local temperature to increase, which may change the resistance. Both effects will decrease avalanche multiplication due to the temperature dependence effects on the impact ionization process. It is essential to measure avalanche multiplication on different size devices with different optical power to ensure the repeatability of the measurements. Low power is always preferred, when possible, to eliminate the effects of series resistance and local heat. There are two ways to extract the α and β for given semiconductor materials. The first one, discussed in the previous section, is using M_e and M_h from pure injection measurements on p-i-n and n-i-p structures.

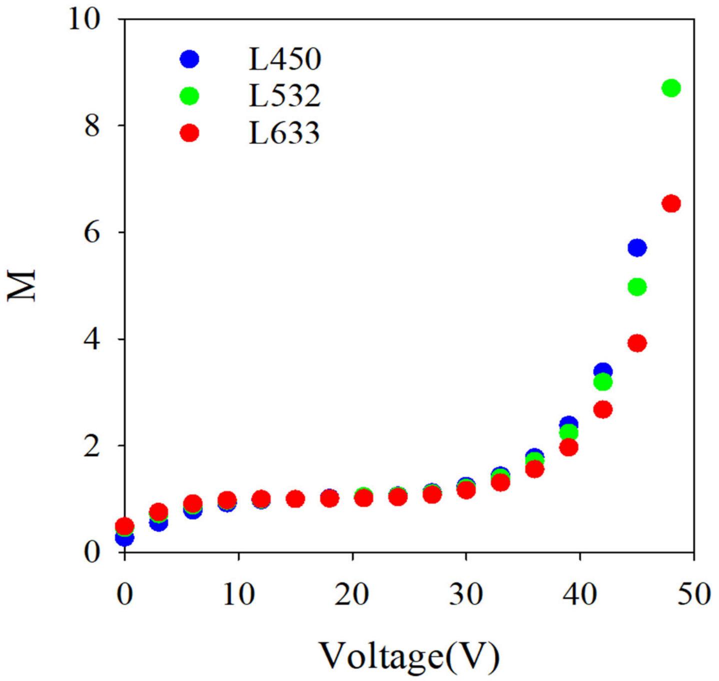

Figure 3.10: Wavelength-dependent avalanche multiplication characteristics in $\alpha > \beta$ material

However, it is also possible to extract α and β by measuring the multiplication with different wavelengths. For example, different absorption profiles can be obtained by illuminating a p-i-n structure with different wavelengths, and the relative magnitude of α and β can be obtained. The longer the wavelength, the more weakly it will be absorbed. Figure 3.8 shows that 99% of 455nm light is absorbed in p^+ cladding layer, and carriers are created deeper in the structure when the wavelength is longer. For a material with $\alpha > \beta$, the avalanche multiplication increases faster with short wavelength injection than with long wavelength injection, as shown in Figure 3.10. This is simply due to the fact that more holes are injected into the high electric field avalanche region at longer wavelengths and the smaller hole ionization coefficient reduces the overall multiplication.

During the fabrication process, mesa-etching does not form a perpendicular edge due to the natural reaction between the etchant and semiconductor. It is important to ensure that there is no light falling on the edge of the mesa structure, as this will cause mixed injection if short-wavelength light falls on the i-region. The laser spot should be kept small enough such that it is within the top optical window of the measuring device.

The phase-sensitive technique is also utilized in photo-multiplication measurements. As discussed, the lock-in amplifier generates a reference signal at the same frequency. The measured signal and lock-in amplifier reference signal can be expressed as:

$$V_{\mathrm{sig}} = A_{\mathrm{sig}} sin \left(\omega_{\mathrm{sig}} t + \theta_{\mathrm{sig}}\right) \tag{3.17}$$

$$V_{ref} = A_{ref} sin \left(\omega_{ref} t + \theta_{ref}\right) \tag{3.18}$$

Where A_{sig} and A_{ref} are the amplitude of photocurrent signal and reference signal respectively, and θ_{sig} and θ_{ref} are labelled in Figure 3.11.

The output of the resultant signal is the product of the two sine waves, given by:

$$V_o = V_{\mathrm{sig}} \times V_{\mathrm{ref}} = A_{\mathrm{sig}} A_{\mathrm{ref}} sin \left(\omega_{\mathrm{sig}} t + \theta_{\mathrm{sig}}\right) sin \left(\omega_{\mathrm{ref}} t + \theta_{\mathrm{ref}}\right)$$
$$= \frac{1}{2} A_{\mathrm{sig}} A_{\mathrm{ref}} \left[cos \left(\omega_{\mathrm{sig}} t - \omega_{\mathrm{ref}} t + \theta_{\mathrm{sig}} - \theta_{\mathrm{ref}}\right) - cos \left(\omega_{\mathrm{sig}} t + \omega_{\mathrm{ref}} t + \theta_{\mathrm{sig}} + \theta_{\mathrm{ref}}\right)\right] \tag{3.19}$$

There is a low pass filter in the lock-in amplifier, which means that the signal component with a frequency $\omega_{\mathrm{sig}} + \omega_{\mathrm{ref}}$ will be filtered out and $\omega_{\mathrm{sig}} - \omega_{\mathrm{ref}}$ will remain as the low-frequency component. At $\omega_{\mathrm{sig}} = \omega_{\mathrm{ref}}$, the lock-in amplifier will output a DC signal:

$$\frac{1}{2} A_{sig} A_{ref} cos \left(\theta_{sig} - \theta_{ref}\right) \tag{3.20}$$

Thus, a photocurrent signal that has the same frequency component will be isolated with the output amplitude proportional to the photocurrent signal amplitude.

The laser/LED source is modulated at a frequency of 180 Hz with a square wave, and the sum of many harmonic sinusoid waves at multiples of f is the measured photocurrent signal:

$$V_{\text{square}} = \frac{2A_p}{\pi}\left[\sin(2\pi f t) + \sin(6\pi f t) + \sin(10\pi f t) + \cdots\right] \tag{3.21}$$

To eliminate any low-frequency noise from the dark current component due to leakage and tunnelling, the first component of this sine wave can be measured and displayed in its RMS value of $2A_p/\pi \times \sqrt{2}/2 = \sqrt{2}A_p/\pi$.

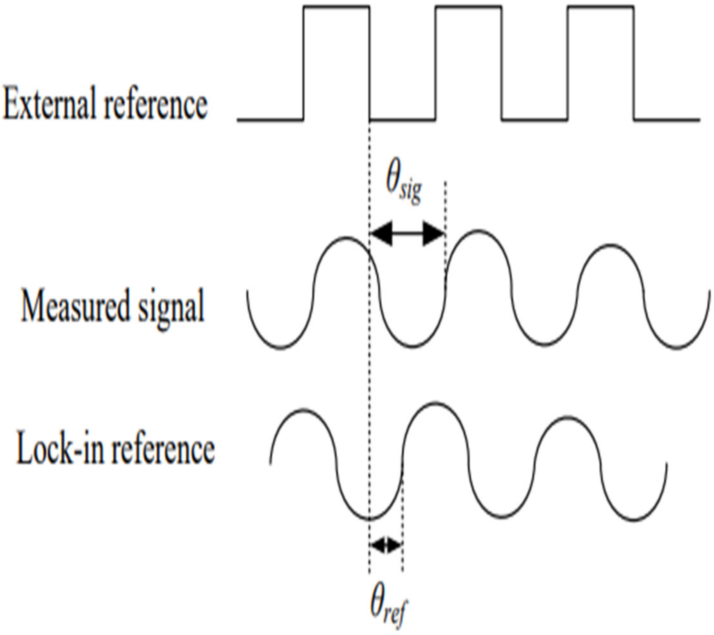

Figure 3.11: A diagram to show the phase sensitive detection technique.

3.1.5 Excess noise measurements

The excess noise measurement set-up is shown in Figure 3.12 and this circuit was designed by Lau et al.[3]. The laser source is mechanically chopped at a frequency of 180Hz and focused on devices with a diameter >200µm with a spot size of 100µm. A low noise transimpedance amplifier (TIA) with a gain of 2.2kV/A was used to amplify the photocurrent signal generated and converted it into a proportional square wave voltage signal at the reference frequency. In order to avoid any saturation of the TIA, the input photocurrent signal should be limited at 1.7mA. The voltage signal coming out from the TIA is then filtered by a low pass band filter with a frequency of 10Mhz with a bandwidth of 4.2 MHz to differentiate the high frequency from the noise at the chopped frequency to remove the photocurrent signal. The resulting output signal from the bandpass filter was further amplified before the power meter convert the signal into the mean square value. A lock-in amplifier measures the noise power coming out from the noise power meter. And an attenuator placed between the amplifier output and noise power meter to prevent amplifier stages from clipping when measuring high noise signals.

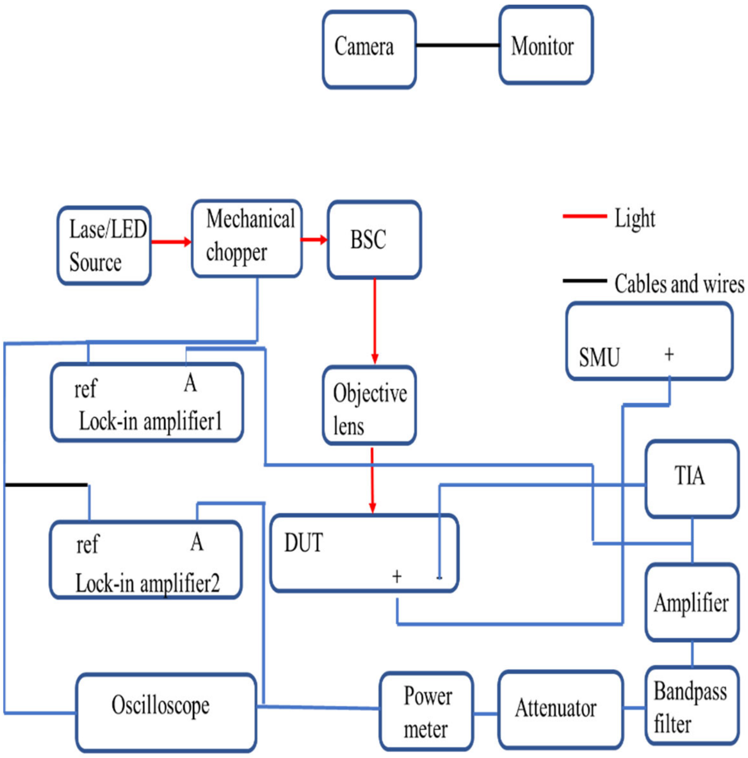

Figure 3.12: A schematic diagram of the experimental set-up for excess noise measurements

The measurement setup is calibrated using a reference device (SFH2701 Silicon PIN photodiode) [4], which only operates with shot noise. It has a unity gain (M=1) at -10V and fully depleted capacitance. The shot noise power of SFH2701 was measured at different optical intensities to present full shot noise due to operating under the non-avalanching condition, as shown in Figure 3.13. The gradient of the shot noise signal increase per unit of photocurrent signal is about 2.969V/V. The measured noise power of the DUT is compared to the measured noise power of the reference device at a given photocurrent to determine excess noise factor by referring to SFH2701.

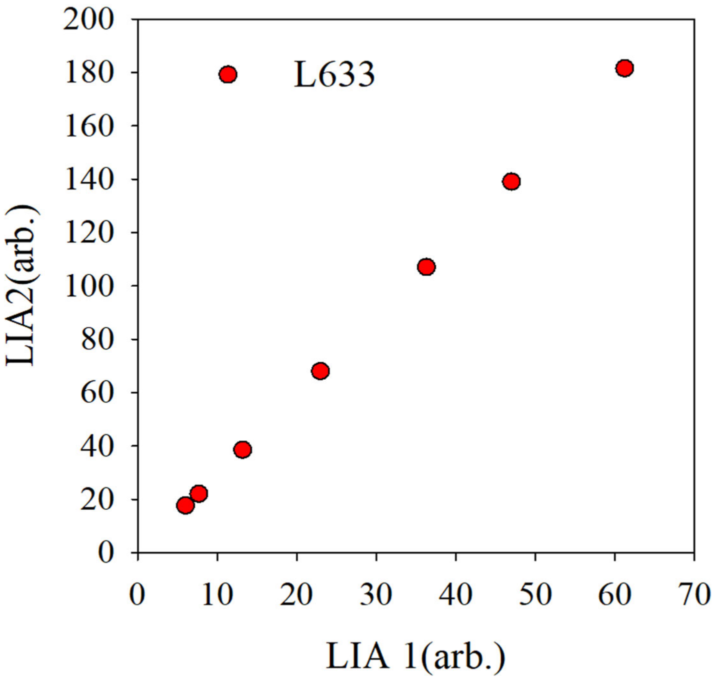

Figure 3.13: Shot noise variation with increase of light intensity at 633nm wavelength.

For an ideal device, the ratio of noise power to photocurrent is defined as:

$$K = \frac{N_u}{I_{ph}} = 2eB_{eff}(C_{si})A^2 \tag{3.22}$$

Where $B_{eff}(C_{si})$ is the effective bandwidth that varies with transimpedance gain capacitance (Calibrated), A is the total system gain.

The total noise power of the DUT with avalanche multiplication is given by:

$$N_{DUT} = 2eIB_{eff}(C_{DUT})A^2MF(M) \tag{3.23}$$

Where $B_{eff}(C_{DUT})$ is the effective noise bandwidth of the DUT at a given capacitance, I is the multiplied photocurrent, M is the multiplication.

As mentioned before, the excess noise factor can be obtained by taking the ratio between the measured noise power of DUT and the reference Si device:

$$F = \frac{N_{DUT}}{N_{ref} \times M^2} \tag{3.24}$$

By relating equations 3.22, 3.23 and 3.24 together, the excess noise factor can be calculated by using the following equation as shown in Figure 3.14:

$$F(M) = \frac{N_{DUT}}{K \times M^2 I} \times \frac{B_{eff}(C_{si})}{B_{eff}(C_{DUT})} \tag{3.25}$$

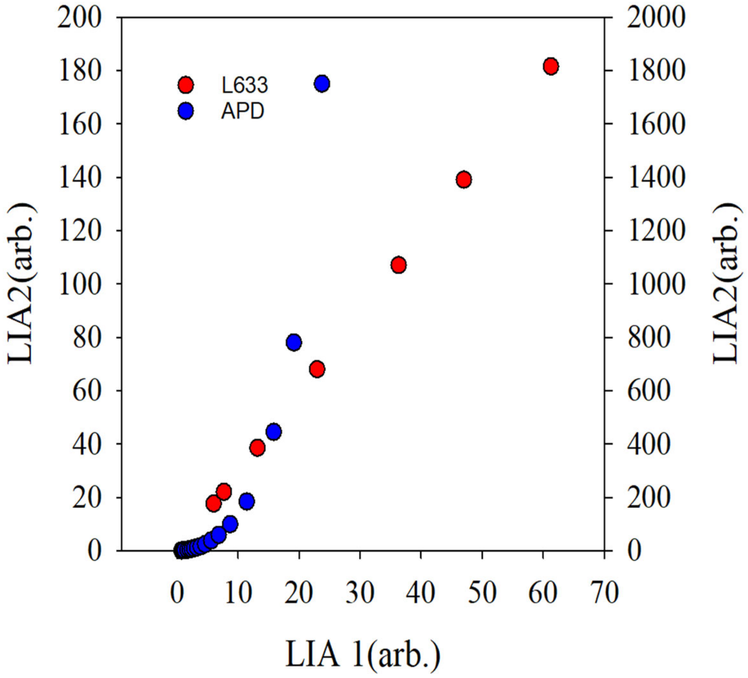

Figure 3.14: Measured noise power for commercial Si diode and APD. LIA1 is the photocurrent and LIA2 is the noise power.

3.1.6 Temperature dependence measurements

Temperature dependence measurements are important as they provide essential information as to how an APD works under different environmental conditions. There is a growing interest in APD performance in a temperature range from 200K to 350K. The low-temperature measurements are carried out in a Janis ST-500 probe station, as shown in Figure 3.15, with a lakeshore temperature controller. In contrast, high-temperature measurements are done by passing a current through a metal hotplate and using a thermometer to monitor the temperature.

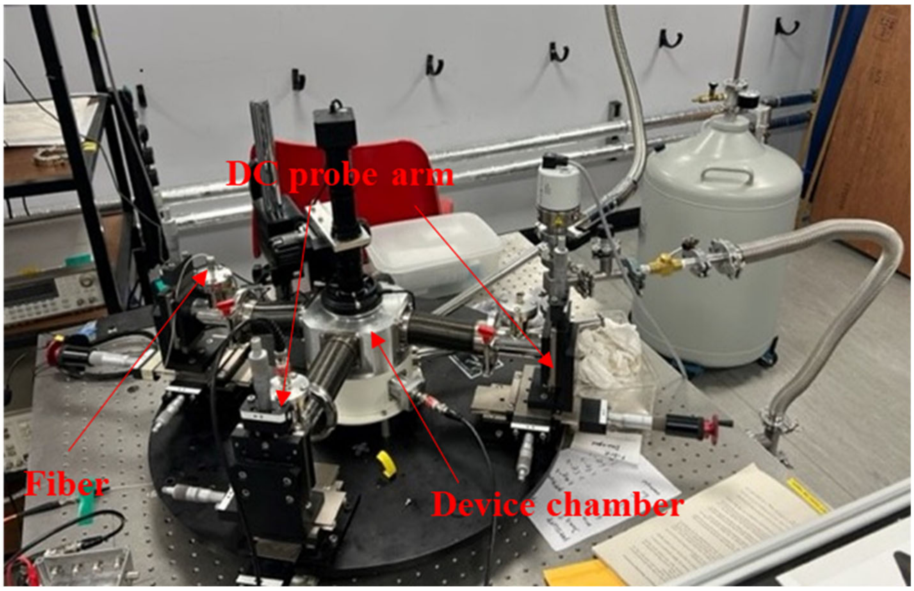

Figure 3.15: Janis ST-500 probe station.

The Janis ST-500 has two DC probe arms and a multimode fibre that can transmit light from visible light to near-infrared. The chamber is pumped down to a pressure of 3×10^{-5} mbar. The contact metal plate can be cooled from 295K to 77K using circulating liquid nitrogen. To achieve pure injection and eliminate the effects of side injection, a fiber with a core of 62.5µm needs to be as close to the device's optical window as possible. The measurement technique is very similar to the photo response and multiplication measurements described in the previous section, but with a cryo-stat probe station in this case. Temperature dependence measurements can provide information such as temperature dependent multiplication and dark current. Detail of the results will be shown in a later section.

3.1.7 Molecular beam epitaxy (MBE)

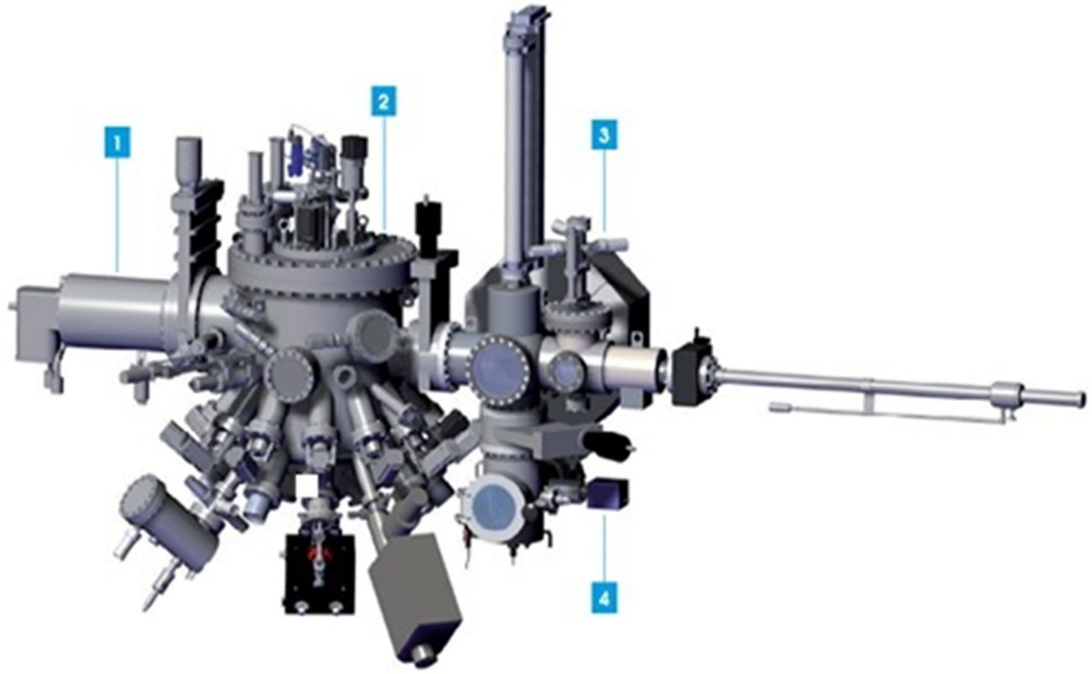

Figure 3.1.6: A schematic diagram of the RIBER comptact 21 DZ system[4]

In 1970s, the first molecular beam epitaxy using a vacuum deposition process was developed[5]. The concept of this technology is very simple. The substrate is held by a clamp in an ultra-high vacuum (UHV) environment ($\sim 10^{-10}$ mBar) and there are atomic fluxes from the tunnelable evaporation of high purity elements in effusion cells. The key elements to this growth technique are:

- A sample stage with an integrated substrate heater.
- A growth chamber sustaining an ultra-high vacuum.
- Several cells containing high purity elements sources.
- Shutters to allow abrupt changes in molecular flux to a substrate.

The temperature in the cell is raised to a temperature where significant sublimation or evaporation occurs. The substrate is heated in the sample stage and the shutter are opened to allow the material to reach the substrate. Adatom bond to exposed lattice site on the substrate form a new semiconductor unit cells. This technique makes high crystal purity and sub-monolayer composition control possible. This technique led to unprecedented advances in semiconductor technology[6]. Technologies such as metalorganic vapour phase epitaxy (MOVPE)[7] are chemical reactions, the simplicity of MBE allows growth to be performed at comparatively low sample temperatures[8].

Material growth for most of the research in this thesis was performed by RIBER Compact 21 DZ MBE system. Figure 3.1.6 shows the schematic of the RIBER Compact 21 DZ MBE reactor. There are three vacuum chambers, including load-lock (4), buffer (3) and growth chambers (2). The growth chamber is attached to the vacuum system (1), including cryo and ion pumps. The pressures for lock-lock, buffer, and growth chambers maintain ~5$\times 10^{-8}$, ~1$\times 10^{-10}$ and ~8$\times 10^{-11}$ Torr, respectively.

3.2 References

[1] S. M. Sze, *Physics of semiconductor devices.* Wiley-Blackwell, 2006.

[2] M. H. Woods, W. C. Johnson, and M. A. Lampert, “Use of a Schottky barrier to measure impact ionization coefficients in semiconductors,” *Solid State Electron*, vol. 16, no. 3, pp. 381–394, 1973, doi: https://doi.org/10.1016/0038-1101(73)90013-0.

[3] K. S. Lau *et al.*, “Excess noise measurement in avalanche photodiodes using a transimpedance amplifier front-end,” *Meas Sci Technol*, vol. 17, no. 7, pp. 1941–1946, 2006, doi: 10.1088/0957-0233/17/7/036.

[4] RIBER, “Extend your research perspectives with riber’s new compact 21 dz.”

[5] A. Y. Cho and J. R. Arthur, “Molecular beam epitaxy,” *Progress in Solid State Chemistry*, vol. 10, pp. 157–191, 1975, doi: https://doi.org/10.1016/0079-6786(75)90005-9.

[6] B A Joyce, “Molecular beam epitaxy,” *Reports on Progress in Physics*, vol. 48, no. 12, p. 1637, 1985, doi: 10.1088/0034-4885/48/12/002.

[7] A. G. Thompson *et al.*, “Large scale manufacturing of compound semiconductors by MOVPE,” *J Cryst Growth*, vol. 170, no. 1, pp. 92–96, 1997, doi: https://doi.org/10.1016/S0022-0248(96)00552-0.

[8] F. W. Smith, A. R. Calawa, C. .-L. Chen, M. J. Manfra, and L. J. Mahoney, “New MBE buffer used to eliminate backgating in GaAs MESFETs,” *IEEE Electron Device Letters*, vol. 9, no. 2, pp. 77–80, 1988, doi: 10.1109/55.2046.

Chapter 4:

Temperature dependence characteristic of $AlAs_{0.56}Sb_{0.44}$ grown on InP

4.1 Introduction

In previous work, Yi *et al.* have demonstrated an extremely low excess noise and high sensitivity in $AlAs_{0.56}Sb_{0.44}$ (hereafter AlAsSb) avalanche photodiodes that can be utilized in high-speed data communications, light detection and ranging(lidar) systems[1]. AlAsSb showed that the excess noise can reach k_{eff}=0.005 with a 1.55µm avalanche region structure. Therefore, the temperature dependence characteristics of this material with significant superior ionization coefficients is worth investigating. Impact ionization is a temperature dependence process. Carrier acquires minimum energy and threshold energy (E_{th}) for impact ionization when traversing the high electric field region. However, the E_{th} depends on the bandgap energy (E_g) [2], which has weak temperature dependence. While carriers are gaining energy travelling in the high electric field region, they also lose energy due to various scattering processes [3]. Of these, phonon scattering is a highly temperature-dependent process. The number of phonons increase with increase of temperature. This leads to the overall avalanche multiplication process being temperature sensitive. It is important to understand the change in multiplication due to temperatures variation in linear mode APD, hence the sensitivity of a APD receiver module. In a Geiger mode APD, it is essential to ensure the V_{bd} and over bias does not change with temperature. There are two ways to mitigate the effects of temperature effects on APD. The reverse bias across the device can be modified with an active variable bias circuit as the temperature changes[4].

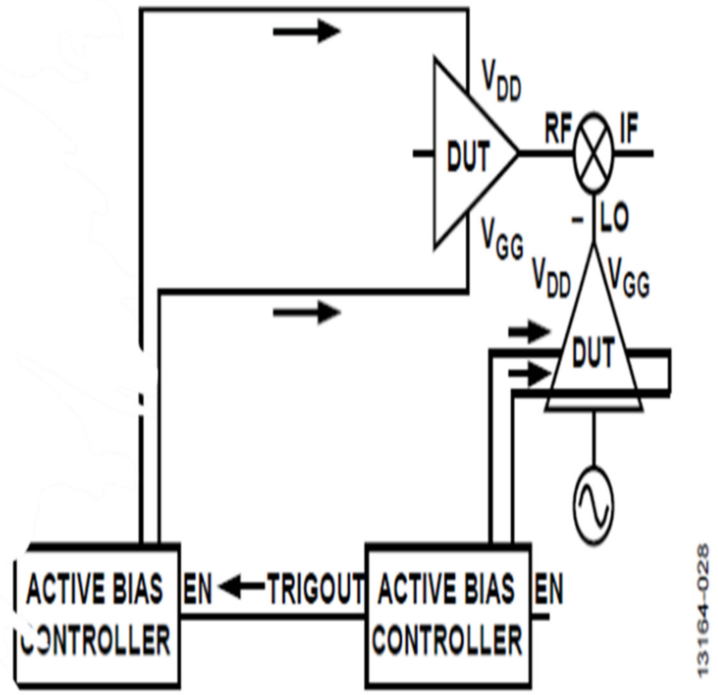

Figure 4.1: A schematic diagram to show the active bias circuit for temperature compensation[5].

Alternatively, the temperature can be stabilized with an embedded thermoelectric cooler(TEC) [6]. It is much simpler to have an APD material that has weak temperature dependence ionization process and small variation in V_{bd} when temperature changes because both are adding extra cost and complexity to the system. The temperature dependence of avalanche multiplication is characterized by using the value of the temperature coefficient of breakdown voltage (C_{bd}):

$$C_{bd} = \frac{\Delta V_{bd}}{\Delta T} \tag{4.1}$$

Where ΔV_{bd} is the change in breakdown voltage and ΔT is the temperature difference.

The C_{bd} values are material-dependent characteristics and can be significant in Silicon APDs(0.78V/°C)[7] and InGaAs APDs (0.11V/°C)[8]. The C_{bd} is found to increase with avalanche region width; since the carriers are experiencing more phonons in a thicker avalanching structure than in a thinner structure, they will undergo larger change in V_{bd} with temperature.

The common telecommunication III-V APD materials InP and InAlAs, As shown in table 4.1, the C_{bd} values, have been investigated on different avalanche region thickness structure at temperatures between 20K to 375K. InP exhibit a C_{bd} value variation from 6 to 73 mV/K with the avalanche region width from 0.13µm to 1.7µm, whereas InAlAs C_{bd} changes from 2.5 to 16 mV/K for avalanche region width from 0.1µm to 1µm[9]. In addition to p-i-n and n-i-p diodes, C_{bd} of InGaAs/InP SACM APDs ranging from 46 to 150 mV/K[10]–[13]. In table 4.2, InGaAs/InAlAs SACM APDs exhibit even lower C_{bd} from 15-40mV/K[14]–[17]. From all the reported C_{bd} values in different structures, reducing w is helpful in reducing C_{bd}. However, this is a trade-off between the excess noise and C_{bd} while changing the avalanch region thickness and the tunnelling current will dominate the dark current when the avalanche region become thin.

Table 4.1: A table to show the temperature dependence C_{bd} in InP and InAlAs[9]

Material	Nominal width (µm)	C_{bd} (mV/K)
InP	1.7	73
	0.8	35
	0.55	24
	0.25	11
	0.13	6
InAlAs	1	16
	0.5	8.7
	0.3	5.6
	0.2	4.1
	0.1	2.5

Table 4.1: A table to show the temperature dependence C_{bd} in InP and InAlAs SACM

	Material	multiplication layer width (μm)	Total depletion width (μm)	Experimental C_{bd} (mV/K)	Calculated C_{bd} (mV/K)
Levin et al[14]	InAlAs	0.13	0.75	15	17
Rouvie et al[15]		0.2	1.4	25	28
Ishimura[25]		0.2	1.1	21	22
Goh et al[17]		1	2.7	40	44
lionel et al[9]		0.15	0.15	23	25
Hyun and Park[10]	InP	0.15-0.40	1.60-1.90	50-70	73-83
Tarof et al[11]		0.2-0.4	3.5-3.7	150	160
Ma et al[12]		0.5	3.5	150	150
lionel et al[9]		0.2	1.2	46	54

Recently, Sb containing material alloy system have attracted a lot of attention for use as the multiplier region in APDs. Sb-containing materials show small excess k_{eff} values (large α/β)[18]–[20] compared to Silicon, InP and InAlAs. Xie et al. demonstrated a small C_{bd} of 0.95 – 1.47mV/K for 80-230nm thick AlAsSb lattice match to InP[21], [22]. The very thin avalanche region structures can benefits from the 'dead-space' effects which reduce the excess noise [23]. In addition, for a given α/β ratio, thin avalanche region structure also provide a higher (GBP)[24] while maintaining a small C_{bd}. However, the Sb containing alloys with a very large α/β ratio means that both low noise and high GBP can be achieved with thick avalanche structures. The C_{bd} of AlInAsSb alloy with a thick avalanche region (890nm) was investigated[26], [27] and found to be small(~7mV/K), and no systematic study of AlAsSb exists. AlAsSb offers the prospect of very high sensitivity telecommunications APDs operating at very high bit rate because AlAsSb is latticed matched to InP whereas AlInAsSb is latticed matched to GaSb[28]. Semi-insulating InP substrate can provide low capacitance compared to doped GaSb substrate, hence avoiding RC limited GBP.

In this study, avalanche multiplication characteristics were studied on five AlAsSb p-i-n and two n-i-p structures that cover avalanche region widths of 0.08 μm to 1.55 μm over a temperature range of 210K to 335K. The temperature dependent ionization coefficients (210K to 335K) were extracted over a wide electric field range from 220kV/cm to 1250kV/cm and compared them to InP and InAlAs structures. Some challenges in undertaking these measurements accurately in materials that exhibits larger α/β ratio and small change in C_{bd} were highlighted. Finally, Monte Carlo modelling was used to explain the mechanism of weak temperature dependence seen in AlAsSb.

4.2 Experimental details

Digital alloy technique was utilized to grown AlAsSb p-i-n and n-i-p structures on n-InP(001) and p-InP(001) substrates respectively. A Veeco GEN930 MBE reactor is used for the digital alloy growth and valved cracker cell supplied both As_2 and Sb_2 flux. The detail of the growth of lattice-matched digital alloy AlAsSb on InP (001) and GaSb(001) substrate are given elsewhere[29], [30]. It is extremely challenging to grow high-quality and lattice-matched InP because of group-V species' wide miscibility bandgap and non-unity sticking coefficient [31][32].

As described above, the AlAsSb p-i-n and n-i-p structures P1-P3 and N1-N2 were grown by a digital alloy technique. P4 and P5 are two thin structures previously reported[21], [22]. There are two more p-i-n InAlAs (P6, N3) structures and one InP p-i-n structure(P7). A schematic diagram of the device structure is shown in Figure 4.2. The i-region is sandwiched between 300nm $p^+(n^+)$ AlAsSb and 100nm $n^+(p^+)$ AlAsSb cladding layers doped with Be and Te with a doping concentration of 2×10^{18} cm^{-3}, respectively. They also have a 20nm highly doped InGaAs contact layer on top and a 500nm InGaAs buffer layer at the bottom. All other homojunction structures have at least 200 nm heavily doped top cladding layers and undoped i-regions.

Details of structures used in this study are given in table 4.3. Mesa devices were fabricated with standard photolithography and wet chemical etching with 2:1 citric acid: hydrogen peroxide(H_2O_2) for the top InGaAs layer and 10:2:200 hydrochloric acid: H2O2: DIW for AlAsSb layers into circular mesa diodes with diameters varying from 70 to 420μm.

Table 4.3: A summary of details of the layers used in this work.

Layer details	**Material**	**Layer structure**	**Nominal *i*-region thickness (μm)**	**CV fitted *i*-region thickness(μm)**	***i*-region doping level (× 10^{15} cm^{-3})**
P1	AlAsSb	PIN	1.5	1.56	5
N1	AlAsSb	NIP	1.5	1.58	7
P2	AlAsSb	PIN	0.6	0.66	8
N2	AlAsSb	NIP	0.6	0.66	8
P3	AlAsSb	PIN	1	1.15	10
P4	AlAsSb	PIN	0.25	0.23	1
P5	AlAsSb	PIN	0.1	0.08	1
P6	InAlAs	PIN	1.01	1.01	3
N3	InAlAs	NIP	0.5	0.51	5
P7	InP	PIN	0.55	0.51	1

4.3 Experimental methods

The total avalanche region width is determined by fitting the experimental capacitance-voltage(C-V) measurements provided that capacitance scales with the area and by using the 1-D model based on Poisson's equation for electric field solver.

AlAsSb should have a low bulk dark current room temperature because of the large indirect bandgap(1.64eV) materials. A PSD technique was used to measure the photocurrent because of the high surface leakage current of the devices (especially at high temperatures).

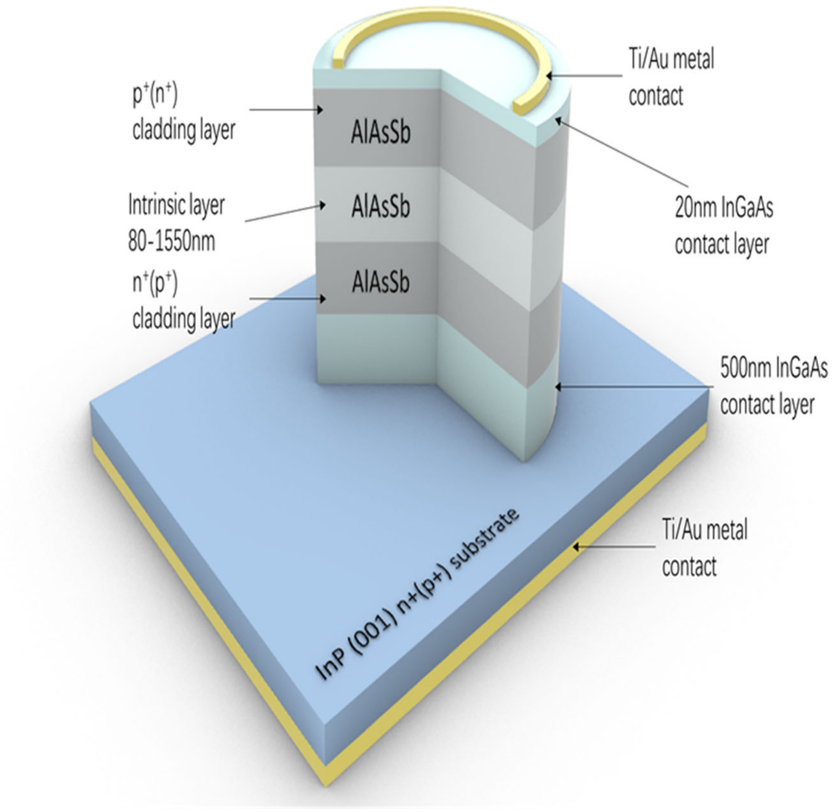

Figure 4.2: A schematic diagram of p-i-n and n-i-p diodes used in this work.

405nm wavelength light for AlAsSb and 532nm for InP and InAlAs ensure >99% light is absorbed in the top cladding layer so that M_e and M_h are obtained by pure electron and pure hole-initiated multiplication in p-i-n and n-i-p structures respectively. To ensure the repeatability of the measurements, multiplication is performed with different optical power on various size devices. The actual multiplication is determined by correcting the photocurrent with the increase of collection efficiency as described in Chapter 2[33]. This technique can reduce the uncertainty down to 5% in multiplication determination.

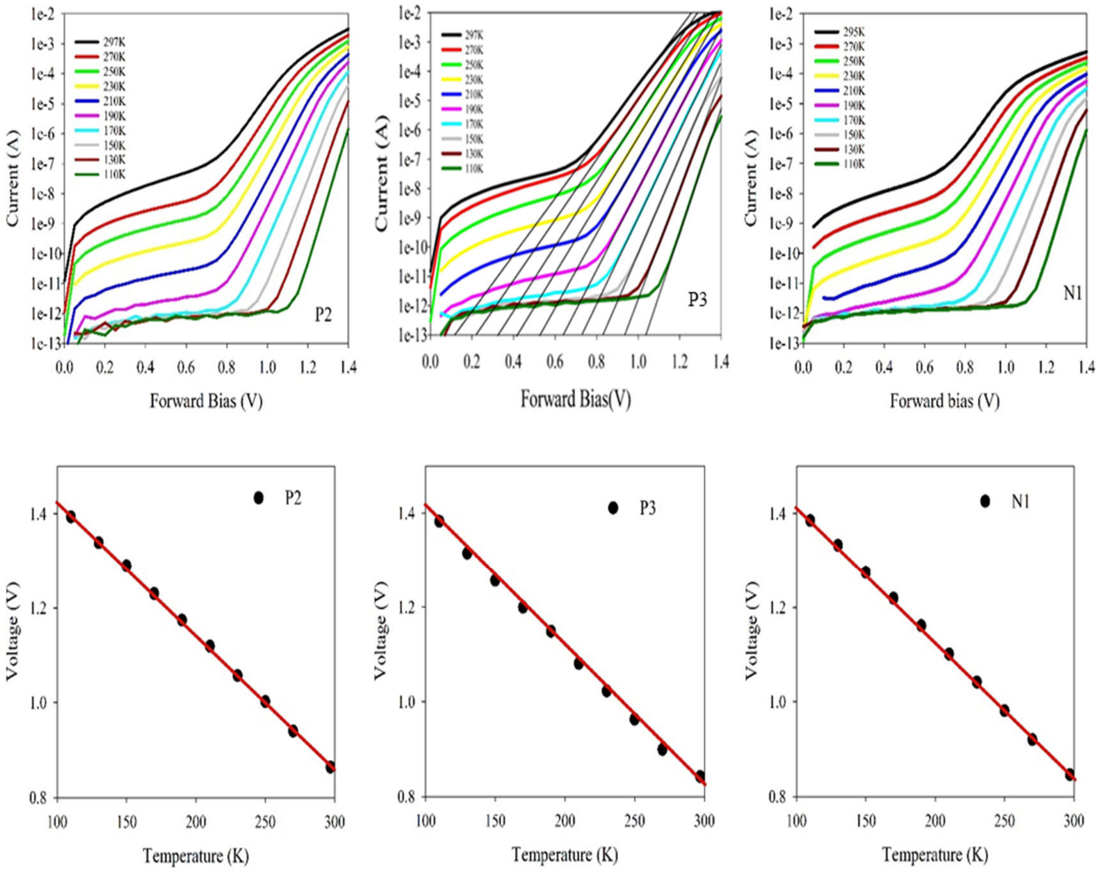

Figure 4.3: Temperature dependence forward current across a 420μA diameter device and a summary of forward voltage drop at a current level of 1μA for P2(0.66μm), P3(1.15μm) and N1(1.55μm). Solid black lines in P3 shows an example of extracting I_0.

It is important to know the junction temperature accurately to measure small values of C_{bd}. To do this, temperature-dependent forward measurements were performed on various structures. The voltage drops at a current of 1μA is used as an indication of the actual junction temperature. This linear relationship between the voltage drops at 1μA and temperature for P2, P3 and N1 are shown in Figure 4.3. In addition, the dark saturation current(I_0) can be extracted by extrapolating the linear curve of the forward

I-V back to the *y*-intercept in Figure 4.3(P3), which can then be used to determine the activation energy. Figure 4.4 shows the relationship between activation energy and forward bias. At 0V, the activation energy is close to $E_g/2$ which is 0.8eV. The linear relationship and activation energy suggest the temperature is expected to have minor uncertainties, and trap states are in the middle of the bandgap. Forward current measurements were taken whenever the temperature-dependent avalanche multiplication measurement was performed to confirm the temperature of the device under test.

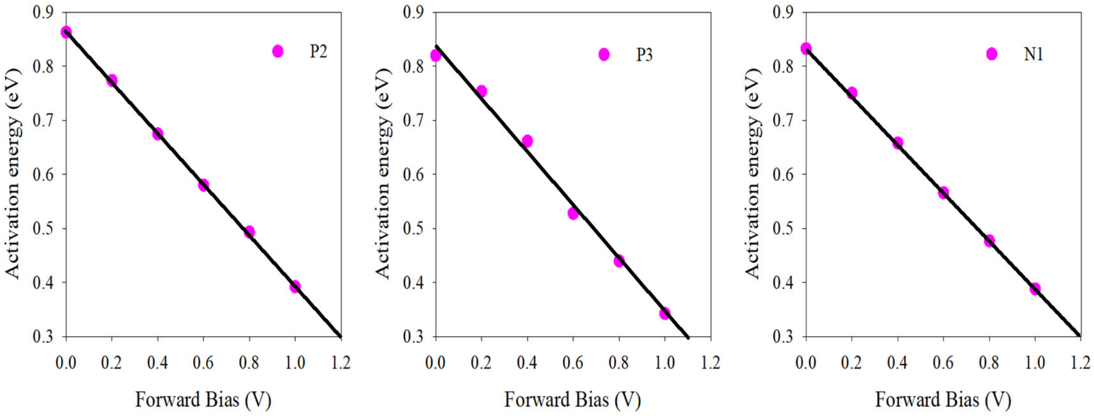

Figure 4.4: Activation energy calculated from the temperature dependence forward bias voltage.

4.4 Temperature-dependent avalanche multiplication characteristics

The temperature dependence ionization characteristics have been investigated on Silicon[34], GaAs[35], AlGaAs[36] and InP[37]. All these results suggested that α and β are increasing with decrease of temperature at approximately the same rate. However, Yuan *et al.* [38]reported that this behaviour can be different in digital InAlAs alloy, where α is increasing while β is decreasing with temperature decreases. It is important to extract the temperature-dependent α and β accurately to estimate the V_{bd}. Moreover, this requires avalanche multiplication measurements on p-i-n and n-i-p structures with different avalanching region thicknesses to cover a wide electric field range.

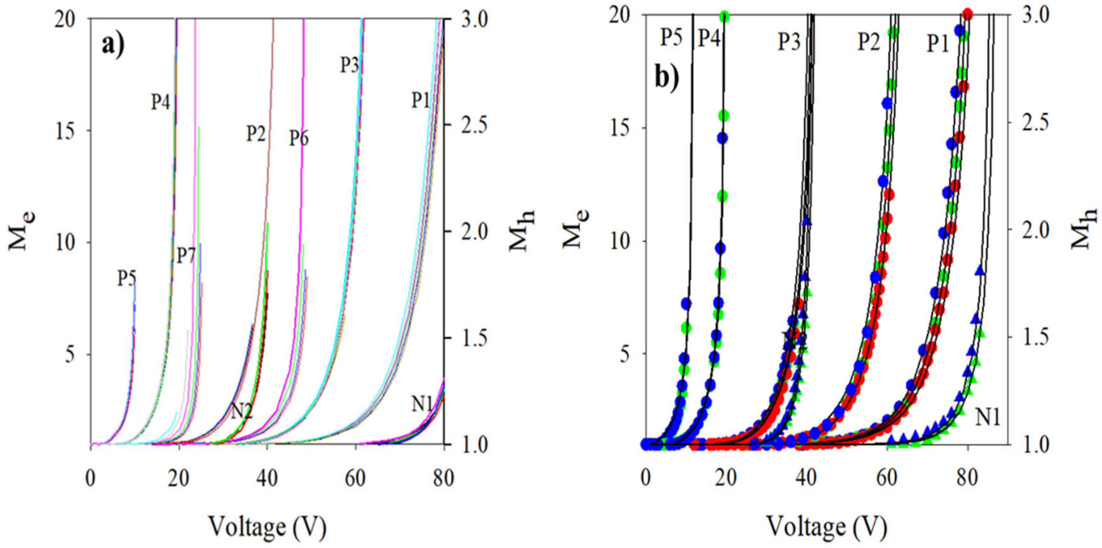

Figure 4.5: **a)** Temperature dependent avalanche multiplication characteristics for AlAsSb, InAlAs and InP. **b)** AlAsSb temperature dependence characteristics are 210K, 295K and 335K for clarity. The blue●, green● and red● symbols represent the temperature at 210K, 295K and 335K, respectively. Solid lines are modelled results using the parameterized ionization coefficients. P1(AlAsSb 1.55μm), P2(AlAsSb 0.66μm), P3(AlAsSb 1.15μm), P4(AlAsSb 0.23μm), P5 (AlAsSb 0.08μm), N1(AlAsSb 1.55μm), N2 (AlAsSb 0.66μm), P6(InAlAs 1.01μm), P7(InP 0.51μm).

Avalanche multiplication measurements for different avalanching region thicknesses AlAsSb, InAlAs and InP were performed from 210K to 335K with an interval of 30-40K as shown in Figure 4.5a. Figure 4.5b only shows the multiplication characteristic at 210K, 295K and 335K with others omitted for clarity. Figure 4.5b shows that the change in multiplication is small from 210K to 335K and these values maintain small in a 1.55μm p-i-n structure(P1). The change in multiplication is smaller in the 1.15μm p-i-n structure(P3) and continues to reduce in the 0.66μm p-i-n structure (P2).

Two thin avalanching region structures(P4 and P5) show negligible changes in multiplication between 210K to 295K which has good agreement with Xie *et al.*'s report[22]. In addition, the multiplication in two n-i-p structures (N1 and N2) also shows a similar behaviour with changing temperatures as in those p-i-n structures.

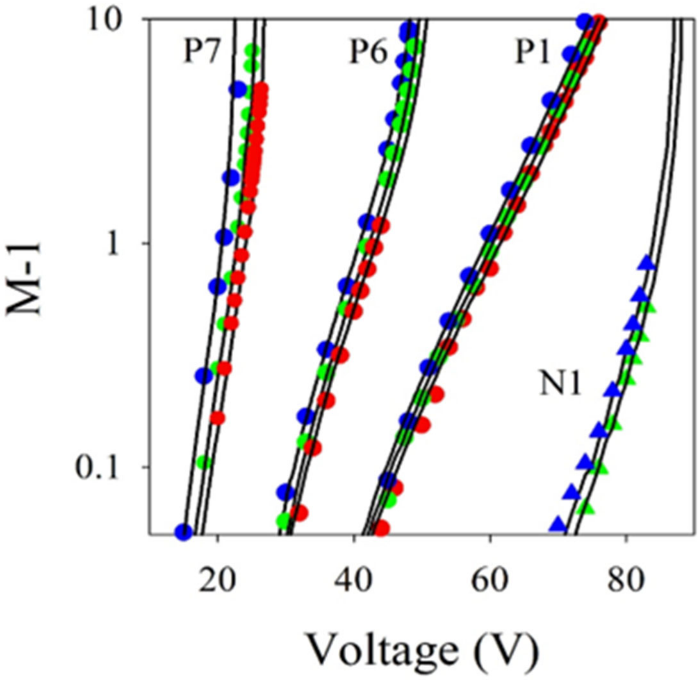

Figure 4.6: Temperature dependent M-1 for 1.55µm AlAsSb p-i-n and n-i-p structures (P1 and N1), 1.01µm InAlAs (P6) and 0.55 InP(P7). Blue🔵, green🟢 and red🔴 symbols represent the temperature at 210K, 295K and 335K.

M_h can only be measured up to a multiplication of 2 because of the large α/β reported[19]. A very high electric field is required for the hole-initiated multiplication to reach a high value of M_h in this material. At a low electric field(M<1.05), ionization is mainly due to the injected carrier type. In contrast, both electrons and holes are contributing to the multiplication at the high electric field, resulting in higher multiplication values. By comparing P1 and N1 in Figure 4.6, both α and β decrease with increasing temperature in AlAsSb. The amount of change is very similar in α and β from low electric field to high electric field. Despite the fact that InAlAs (P6) and InP (P7) have thinner avalanching regions, they still show larger changes in multiplication compared to AlAsSb(P1).

The impact ionization coefficients can be extracted by solving the ionization integral across the multiplication region based on the multiplication data shown in Figure 4.5 and Figure 4.6,

$$M(x) = \frac{\exp\left[-\int_0^x \left(\alpha(x')-\beta(x')\right)dx'\right]}{1-\int_0^W \alpha(x')\exp\left[-\int_0^{x'} \left(\alpha(x'')-\beta(x'')\right)dx''\right]dx'} \tag{4.2}$$

Where $M(x)$ is the multiplication when a photon is injected at position x, and W is the total avalanching region width.

There are some uncertainties in W because of the C-V measurements and the dielectric constant value assumed and largely due to the C-V measurements. There is about 3% uncertainty in the determination of the exact electric field.

A numerical model (RPL) is used to extract α and β while considering the variation in the electric field due to background doping across the avalanche region. The temperature dependent (210K to 335K) ionization coefficients for AlAsSb and InAlAs are shown in Figure 4.7. It shows that both α and β increase with decrease of temperature. The change is very small in AlAsSb, and it is only significant at lower electric fields where the scattering events are more dominant in the carrier transport process. Similarly, InAlAs α and β are extracted over the same temperature range from the multiplication data of P6 and N3. It suggests that both α and β are changing with a similar trend as AlAsSb, but with larger variation over the temperature range from 210K to 335K.

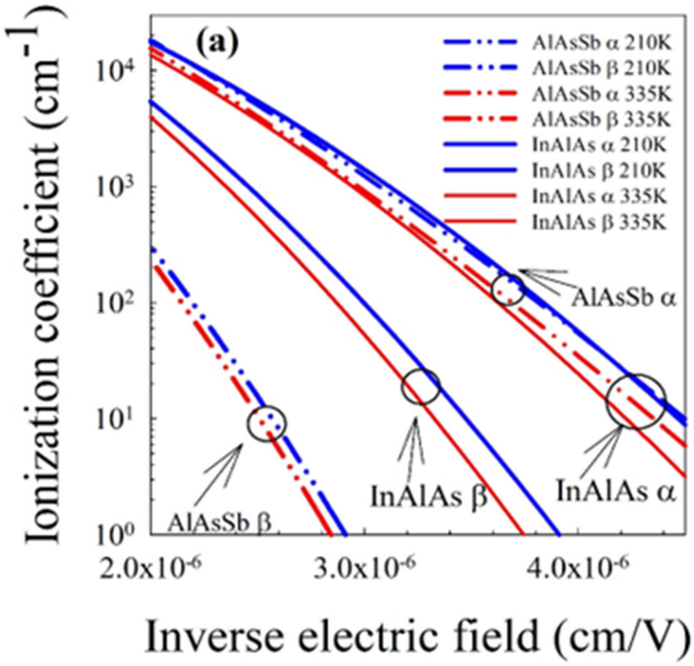

Figure 4.7: ionization coefficient variation with temperature for AlAsSb and InAlAs

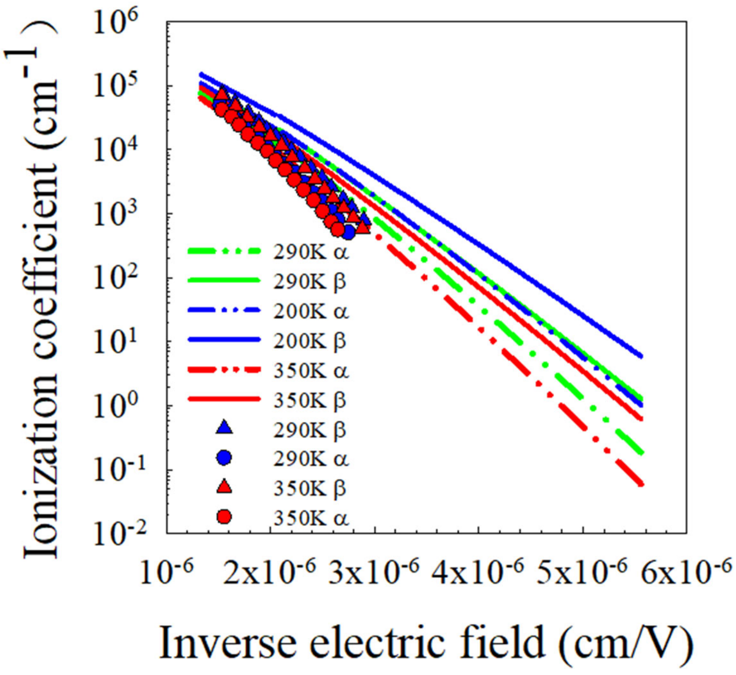

Figure 4.8: Ionization coefficient variation with temperature for InP from 200K to 350K. Solid lines are ionization coefficients extracted in this work. Symbol are results reported by Taguchi *et al.*[37]

A similar analysis approach is undertaken on the avalanche multiplication from InP(P7) structure. It agrees well with the data that Taguchi et al. reported[37]. In Figure 4.7, for an ionization coefficient of 100 cm^{-1}, the electric field has to increase by ~2.4% and 3.4% for α and β in AlAsSb over the temperature range from 210K to 335K. However, the magnitude of this change is more significant in InAlAs, at 4.8% for α and 5.7% for β. In Figure 4.8, InP shows the most significant temperature-sensitive characteristics in α and β over the same temperature range, with the electric field increasing from 11.6% for α and 11.4% for β. Taguchi *et al.*[37] results suggested similar temperature dependence characteristics as the temperature increased from 290K to 350K.

The temperature-dependent ionization coefficients for AlAsSb, InAlAs and InP are parameterized into the following equations[39], which then can be implemented into the RPL model to estimate the avalanche multiplication and breakdown voltage with a function of temperature. The impact ionizations assume that the carriers only depend on the local electric field and are not affected by 'dead-space' effects[40] or their history[41]. The effect of 'dead-space' will overestimate the low values multiplication and is more significant in thin structures[42] but negligible in very thick avalanching region structures(>200nm). The model results show good agreements with the experimental data, as shown in Figure 4.5 and Figure 4.6.

For AlAsSb:

- For 220 KV/cm ≤ E ≤ 500 KV/cm and

$$\alpha(E,T) = 5.70 \times 10^{5} \exp\left[-\left(\frac{3.49\times10^{2}\times T+1.10\times10^{6}}{E}\right)^{1.43}\right] \mathrm{cm}^{-1} \tag{4.3}$$

- For 500 KV/cm < E ≤ 1250 KV/cm

$$\alpha(E,T) = 3.90 \times 10^{5} \exp\left[-\left(\frac{2.73\times10^{2}\times T+1.18\times10^{6}}{E}\right)^{1.25}\right] \mathrm{cm}^{-1} \tag{4.4}$$

- For 360 KV/cm ≤ E ≤ 1250 KV/cm

$$\beta(\mathrm{E,T}) = 3.20 \times 10^{5} \exp\left[-\left(\frac{2.39\times10^{2}\times T+1.63\times10^{6}}{E}\right)^{1.60}\right] \mathrm{cm}^{-1} \tag{4.5}$$

For InAlAs:

- For 220 KV/cm ≤ E ≤ 980 KV/cm and

$$\alpha(E,T) = 2.20 \times 10^{5}\exp -\left(\frac{3.97\times10^{2}\times T+7.76\times10^{5}}{E}\right)^{1.71} \text{cm}^{-1} \tag{4.6}$$

$$\beta(\mathrm{E},\mathrm{T}) = 2.95 \times 10^{5}\exp\left[-\left(\frac{3.89\times10^{2}\times T+1.04\times10^{6}}{E}\right)^{1.71}\right] \text{cm}^{-1} \tag{4.7}$$

For InP:

- For 180 KV/cm ≤ E ≤ 480 KV/cm

$$\alpha(E,T) = 1.41 \times 10^{6}\exp\left[-\left(\frac{1.67\times10^{3}\times T+1.22\times10^{6}}{E}\right)^{1.23}\right] \text{cm}^{-1} \tag{4.8}$$

$$\beta(\mathrm{E},\mathrm{T}) = 2.11 \times 10^{6}\exp\left[-\left(\frac{1.68\times10^{3}\times T+1.32\times10^{6}}{E}\right)^{1.15} \right. \text{cm}^{-1} \tag{4.9}$$

- For 480 KV/cm ≤ E ≤ 750 KV/cm

$$\alpha(E,T) = 1.41 \times 10^{6}\exp\left[-\left(\frac{2.01\times10^{3}\times T+1.30\times10^{6}}{E}\right)^{1.15} \right. \text{cm}^{-1} \tag{4.10}$$

$$\beta(\mathrm{E},\mathrm{T}) = 2.20 \times 10^{6} \exp\left[-\left(\frac{2.37\times10^{3}\times T+1.53\times10^{6}}{E}\right)^{1.01}\right] cm^{-1} \tag{4.11}$$

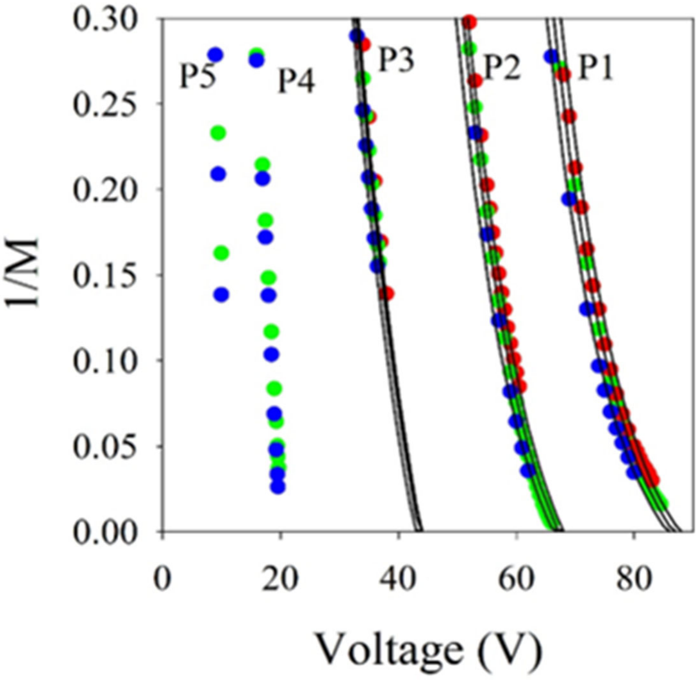

Figure 4.9: 1/M versus voltage for AlAsSb. Blue●(210K), green●(295K) and red●(335K) are experimental data. Black solid lines are calculated using equations 4.3-4.5

Plotting the inverse of avalanche multiplication($1/M$) and extrapolating to zero[43] is often used to determine the breakdown voltage. However, this method can be problematic for material with a large α/β ratio, as shown in Figure 4.9. As the avalanching region width becomes thicker, the larger the α/β ratio, a larger multiplication value is required to predict breakdown voltage (V_{bd}) accurately. Although P1 can reach a multiplication value up to 40, it is not enough to extrapolate the $1/M$ line accurately. Miller's empirical expression can only predict the M and estimate the V_{bd} for materials with an α/β ratio close to unity. Instead, it is more reliable to determine the V_{bd} by calculating it from the extracted ionization coefficients, as shown by the solid black lines in Figure 4.9. It requires $M \geq 6$ to measure the change in voltage accurately. However, this seems to agree closely with those calculated at breakdown voltage, so this can be used to provide us with an accurate estimate of C_{bd}.

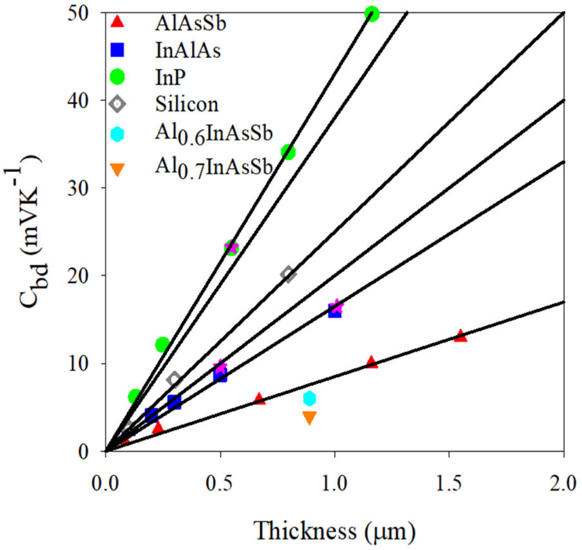

Figure 4.10: Comparison of C_{bd} of this work with other reported data for other semiconductors including InP[9], InAlAs[9], Si[34] and AlInAsSb[27]. ★ are the measurements on InP and InAlAs done respectively in this study. Black lines are the estimated values of P for different materials.

Figure 4.10 shows C_{bd} values of different thicknesses p-i-ns and n-i-ps for different semiconductor materials. C_{bd} values of InP and InAlAs with different thicknesses are taken from [8] and shown as the green and blue symbols. P7, P6 and N3 are shown in pink stars and agree well with reported data. Because carriers experienced fewer phonon scattering events prior to impact ionization at high electric field[34], [44], the C_{bd} increases with total avalanching region thickness. The C_{bd} of AlAsSb is significantly lower than those of InAlAs and InP for similar avalanching region thickness. The results of P1, P2 and P3 show good agreement with P4 and P5, published previously. The linear relationship between the avalanching region width and C_{bd} values (values extracted from Figure 4.10) can be defined as:

$$C_{bd} = P \times W_m (mVK^{-1}) \tag{4.12}$$

Where P is the gradient for different materials and W_m is the total avalanching width

Table 4.4: A summary of P values for different semiconductor materials

Material	P (C_{bd} coefficient)
AlAsSb	8.5
InAlAs	16.5
GaInP	20
Silicon	25
GaAs	38
InP	43

As stated in table 4.4 above, AsAsSb has the smallest P value whereas InP is much larger. Here, the assumption is that C_{bd} is zero when there is no depletion region. This expression is valid for structures with a uniform electric field across the avalanche region. In very thin i-region structures, it is important to consider the cladding layers depletion since it is becoming a significant portion of the total depletion width. Based on the information in Figure 4.10 and table 4.4, the C_{bd} is 5.14mV/K, 10.5mV/K, 15.5mV/K and 25.3mV/K for AlAsSb, InAlAs, Si and InP, respectively for a given 0.6µm structures. More interestingly, $Al_{0.7}In_{0.3}As_{0.3}Sb_{0.7}$ quaternary alloy latticed match to GaSb demonstrated an even lower C_{bd} than AlAsSb (symbols in Figure 4.10).

Telecommunication applications usually utilize the SACM-APD structures for 1310nm and 1550 detection. A narrow bandgap material (InGaAs, GaAsSb) can be used as an absorber in the low field region, whereas large bandgap material can be used as a multiplier in the high field region. Then it is important to understand the C_{bd} variation in a SACM structure. It has been shown that C_{bd} increases linearly with avalanching region width. This means the breakdown electric field also varies linearly with depletion width in a SACM APD. Assume that impact ionization only occurs inside the multiplication region. It is straightforward to show that the C_{bd} of the SACM APD depends on the multiplier region thickness and the total depletion width[9]:

$$C_{bd}(SACMAPD) = C_{bd}(W_m) \times \frac{W_{\text{depletion}}}{W_m} mVK^{-1} \tag{4.13}$$

Where W_m is the multiplier thickness and $W_{\text{depletion}}$ is the total depletion width.

By combining equation 4.12 and equation 4.13, the C_{bd} can be rewritten as:

$$C_{bd}(SACMAPD) = P \times \left(W_{abs} + W_{cg} + W_m\right) mVK^{-1} \tag{4.14}$$

Where W_{abs} is the absorber thickness and W_{cg} is the charge sheet and grading thickness.

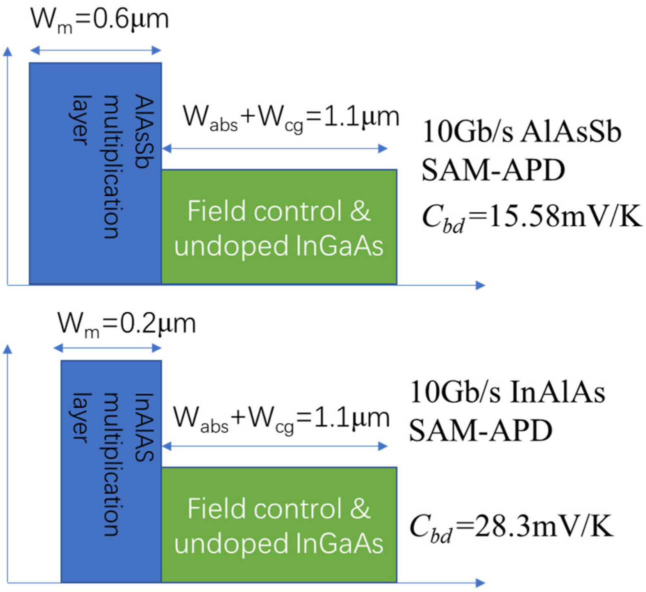

Figure 4.11: A schematic diagram of AlAsSb and InAlAs SACM APD design.

For a 10Gb/s telecommunication application, there are two designs shown in Figure 4.11. One needs a 1.1µm InGaAs absorber and a 0.2µm InAlAs multiplier with a breakdown voltage of 32V[45]. The C_{bd} is estimated to be 28.3mV/K from equation

4.13. However, a 0.6μm AlAsSb can replace the InAlAs multiplication region, still operating at 10Gb/s with a larger breakdown voltage. Because of the larger *α/β* ratio in AlAsSb can provide better sensitivity and a much lower C_{bd} of 15.58mV/K.

4.5 Discussion

APDs must be able to operate over a wide range of temperatures to adapt to different working conditions, so it is important to either have temperature insensitive material or temperature compensation systems for APD to operate with a constant gain. Multiplication can be highly temperature dependent because impact ionization is a temperature sensitive process.

As discussed in the previous section, determining the breakdown voltage of thick AlAsSb structures(P1-P3) using 1/M is unpractical. Because it requires very high multiplication to determine the V_{bd} accurately, the high surface dark current and edge breakdown limit the highest measurable multiplication. The reason that requires a high multiplication value to determine the avalanche breakdown is the uncertainties in the bending of the *1/M* curve, as shown in Figure 4.12. A breakdown voltage analysis is performed to understand this uncertainty in predicting V_{bd} by *1/M* for large *α/β* ratio material.

An artificial semiconductor impact ionization coefficient is assumed for electrons and expressed as:

$$\alpha = 7.03 \times 10^5 \times \exp\left(-\left(\frac{12.3\times 10^5}{E}\right)^1\right) \qquad (4.15)$$

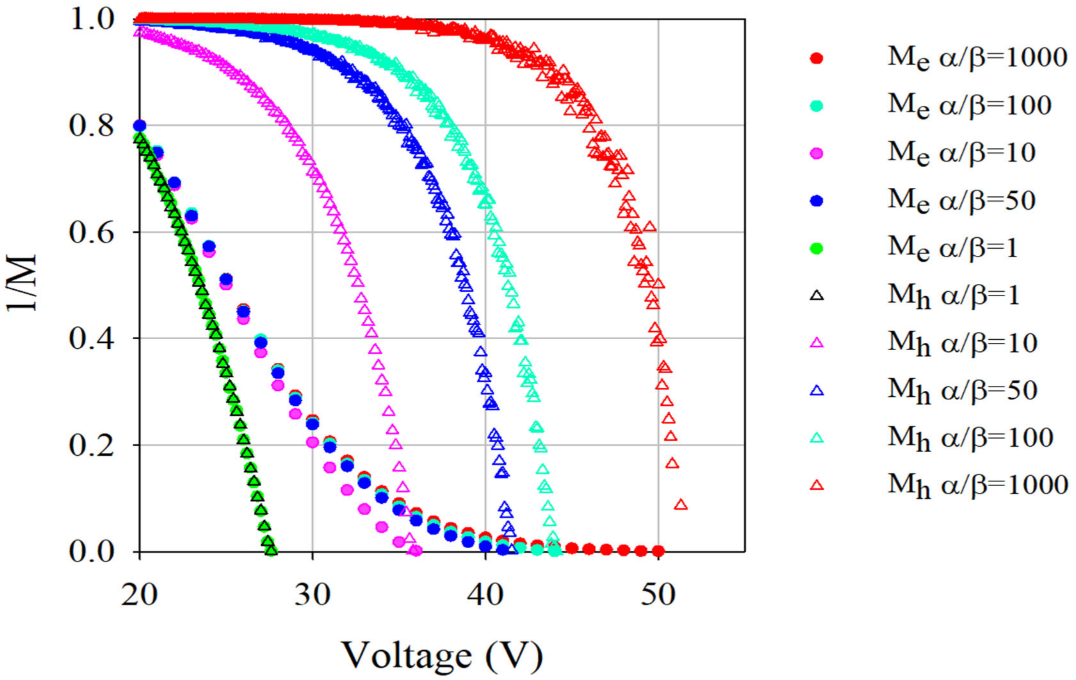

Figure 4.12: Calculated *1/M*$_e$ and *M*$_h$ for different artificial semiconductor materials with different ratios.

The impact ionization coefficient of the hole has a constant ratio to α of 1,10,50,100, 1000 and infinity. Assuming a 1μm ("dead-space" effect negligible) p-i-n structure with a uniform electric field in the avalanche region, the multiplication can be calculated with equation 4.15 above, as shown in Figure 4.12. The breakdown voltage increases as the α/β ratio increases. As the α/β ratio increases, it is getting more challenging to draw a straight line through $1/M_e$ and extrapolate to "0" to predict the V_{bd} from M_e unless a very high multiplication value can be obtained. It suggests that the V_{bd} can be estimated accurately if the material has an α/β ratio close to ~1. However, for a material with α/β ratio of 1000, the voltage at the multiplication of 20 is 34.5V, but the actual breakdown is 51.6V.

However, the breakdown voltage estimation from M_h can be accurate. However, the measurement of M_h is extremely hard to reach a high multiplication value for a material with a large α/β ratio. N1 is an example, and the results are shown in Figure 4.16. The α/β ratio gets larger in the thicker structure of AlAsSb (P3 to P1), and a larger multiplication value is required to determine the breakdown (V_{bd}) accurately. For P1

(1.55µm), the V_{bd} cannot be estimated accurately by extrapolating the $1/M_e$ line to the multiplication of 40. The empirical expression suggested by Miller can only work with a material with an α/β ratio close to "1". It is more accurate to know the breakdown voltage by calculating the M_e from the ionization coefficient (solid lines), as shown in Figure 4.9

AlAsSb shows weak temperature dependence from 210K to 335K, the small change in α and β in this ternary semiconductor can be attributed to the presence of alloy scattering, which is considered a temperature-insensitive process[46]. The analytical-band Monte Carlo(AMC) models have shown the effects of alloy scattering of α in InGaAs[47] and on the breakdown field in $Al_{0.6}Ga_{0.4}As$. MC models simulation on these materials shows that the alloy scattering contributes significantly to the overall scattering events, making the phonon scattering in the structure less critical. This work investigates the effect of alloy scattering on the temperature dependence of β in AlAsSb and InAlAs by the conventional analytical-band MC model[48]. It assumes that the intra and inter-band phonon scattering, and alloy scattering processes are acoustic, polar optical, and non-polar optical for hole transport in the first three valance bands (the heavy hole, light hole and spin-split off bands). This MC model successfully reproduces the electric field dependence β in AlAsSb and InAlAs at 210K and 335K, as shown in Figure 4.13.

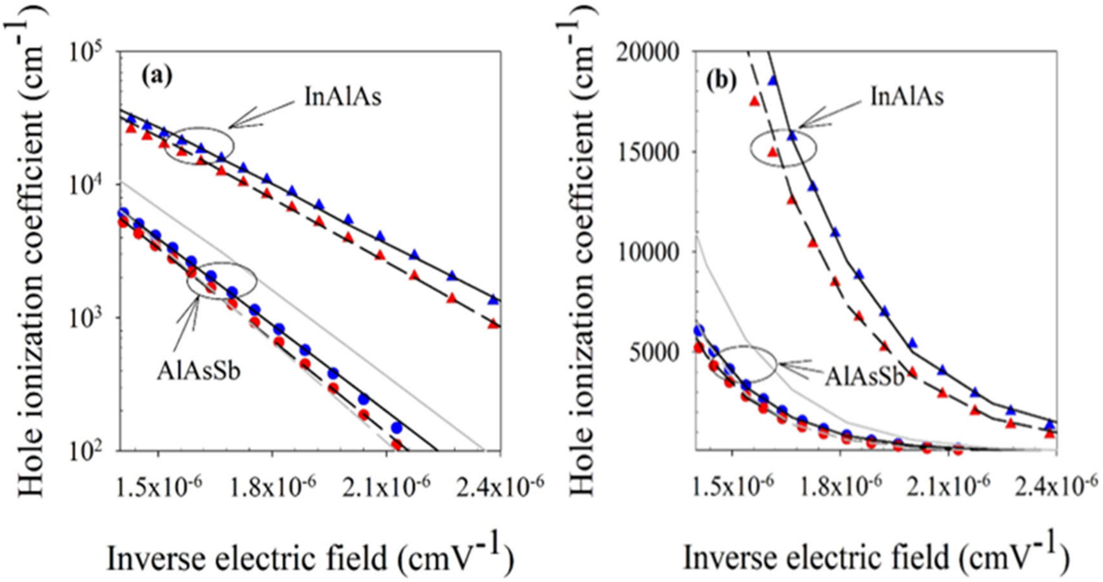

Figure 4.13: a) analytical-band MC model for the temperature dependence of β in AlAsSb and InAlAs. Symbols are data from Figure 4.7 and solid lines(210K); Dashed lines(335K) MC model simulation results. b) Same data but in a linear plot

The alloy disorder potential in the MC model is 0.9eV and 0.6eV for AlAsSb and InAlAs, respectively, which are similar to values calculated by Ong et al.[49] based on the electronegativity difference of Phillips[50]. The model can produce the β, which agrees with the experimental measurements that determined β for AlAsSb and InAlAs when changing the temperature from 335K to 210K while maintaining other identical parameters. In addition, simulation is repeated with reduced alloy potential in AlAsSb to that of InAlAs, i.e., 0.6eVm, while increasing the phonon scattering rate to reproduce the β at 335K (grey dashed line in Figure 4.13). It demonstrates a much more significant increase in β at 210K shown by the solid grey line in Figure 4.13. This is observed because holes are experiencing less alloy scattering while the temperature-sensitive phonon scattering has a relatively more significant role in the overall scattering events. Therefore, this suggests that phonon (or total scattering rates) and the ratio of phonon scatterings and alloy scattering rates determine the temperature dependence of ionization coefficients in the semiconductor alloy. The phonon energy of Sb-containing alloy is likely to be smaller because of the large mass of Sb atoms, leading to a higher number of phonons. However, this may not be obvious as the relative increase in the proportion of the scattering events is due to alloy scattering. Therefore, since alloy scattering dominates carrier transportation before impact ionization, a material with large alloy potential like AlAsSb can exhibit a weak temperature dependence of ionization coefficients. This may also explain quaternary alloy $Al_{0.7}In_{0.3}As_{0.3}Sb_{0.7}$ with more Sb has even lower C_{bd} than AlAsSb.

4.6 Conclusion

Avalanche multiplication measurements with five AlAsSb p-i-n and n-i-p structures from 210K to 335K show that both α and β increase as the temperature decreases at a similar rate. The effects of temperature dependence are less significant in high electric fields than in low electric field transportation. By comparing similar thickness InAlAs and InP, AlAsSb shows a significantly lower breakdown voltage variation with temperature. MC model suggests that large alloy potential is responsible for temperature insensitive characteristics. Thicker AlAsSb can be used as a multiplication region in SACM structures and is still likely to perform better than InP and InAlAs because of its P values.

4.7 References

[1] X. Yi *et al.*, “Extremely low excess noise and high sensitivity AlAs0.56Sb0.44 avalanche photodiodes,” *Nat. Photonics*, vol. 13, no. 10, pp. 683–686, 2019, doi: 10.1038/s41566-019-0477-4.

[2] K. Yeom, J. M. Hinckley, and J. Singh, “Theoretical study on threshold energy and impact ionization coefficient for electrons in $Si_{1-x}Ge_x$,” *Appl. Phys. Lett.*, vol. 64, no. 22, pp. 2985–2987, 1994, doi: 10.1063/1.111379.

[3] M. V Fischetti, “Monte Carlo Simulation of Transport in Technologically Significant Semiconductors of the Diamond and Zinc-Blende Structures-Part I : Homogeneous Transport,” vol. 38, no. 3, 1991.

[4] S. Deng, A. P. Morrison, and J. Hayes, “A bias and control circuit for gain stabilization in avalanche photodiodes,” pp. 37–37, 2013, doi: 10.1049/ic.2012.0187.

[5] K. Kaya, “Meeting Biasing Requirements of Externally Biased RF/Microwave Amplifiers with Active Bias Controllers,” Norwood, 2016.

[6] Princeton lightwave, “PAR Series - High Sensitivity APD Front End Receiver Modules,” pp. 1–3, 2016, [Online]. Available: https://sphotonics.ru/upload/iblock/be0/par_series_high_sensitivity_apd_front_end_receiver_modules.pdf.

[7] HAMAMATSU, “High-sensitivity Si APD for detection of light with a wavelength of 266 nm,” Ichino-cho, 2018. [Online]. Available: http://hamamatsu.com/resources/products/ssd/pdf/tech/si_apd_technical_information.pdf.

[8] Hamamatsu, “High Speed InGaAs APD,” Ichino-cho, 2019.

[9] L. J. J. Tan *et al.*, “Temperature dependence of avalanche breakdown in InP and InAlAs,” *IEEE J. Quantum Electron.*, vol. 46, no. 8, pp. 1153–1157, 2010, doi: 10.1109/JQE.2010.2044370.

[10] K.S. Hyun and C.Y. Park, “Breakdown characteristics in InP/InGaAs avalanche photodiode with p-i-n multiplication layer structure,” *J. Appl. Phys.*, vol. 81, no. 2, pp. 974–984, Jan. 1997, doi: 10.1063/1.364225.

[11] L.E. Tarof, J. Yu, T. Baird, R. Bruce, and D.G. Knight, “Temperature measurements of separate absorption, grading, charge, and multiplication (SAGCM) InP/InGaAs avalanche photodiodes (APD’s),” *IEEE Photonics Technol. Lett.*, vol. 5, no. 9, pp. 1044–1046, Sep. 1993, doi: 10.1109/68.257186.

[12] C. L. F. Ma, M. J. Deen, L. E. Tarof, and J. C. H. Yu, “Temperature dependence of breakdown voltages in separate absorption, grading, charge, and multiplication InP/InGaAs avalanche

photodiodes," *IEEE Trans. Electron Devices*, vol. 42, no. 5, pp. 810–818, 1995, doi: 10.1109/16.381974.

[13] R. Sidhu *et al.*, "2.4 [micro sign]m cutoff wavelength avalanche photodiode on InP substrate," *Electron. Lett.*, vol. 42, no. 3, p. 181, 2006, doi: 10.1049/el:20063415.

[14] B. F. Levine *et al.*, "A New Planar InGaAs–InAlAs Avalanche Photodiode," *IEEE Photonics Technol. Lett.*, vol. 18, no. 18, pp. 1898–1900, 2006, doi: 10.1109/LPT.2006.881684.

[15] A. Rouvie, D. Carpentier, N. Lagay, J. Decobert, F. Pommereau, and M. Achouche, "High Gain×Bandwidth Product Over 140-GHz Planar Junction AlInAs Avalanche Photodiodes," *IEEE Photonics Technol. Lett.*, vol. 20, no. 6, pp. 455–457, 2008, doi: 10.1109/LPT.2008.918229.

[16] S. R. Forrest, R. F. Leheny, R. E. Nahory, and M. A. Pollack, "In0.53Ga0.47As photodiodes with dark current limited by generation-recombination and tunneling," *Appl. Phys. Lett.*, vol. 37, no. 3, pp. 322–325, Aug. 1980, doi: 10.1063/1.91922.

[17] D. S. G. Ong, J. S. Ng, Y. L. Goh, C. H. Tan, S. Zhang, and J. P. R. David, "InAlAs Avalanche Photodiode With Type-II Superlattice Absorber for Detection Beyond 2 $\mu\hbox{m}$," *IEEE Trans. Electron Devices*, vol. 58, no. 2, pp. 486–489, 2011, doi: 10.1109/TED.2010.2090352.

[18] Y. Yuan, J. Zheng, A. K. Rockwell, S. D. March, S. R. Bank, and J. C. Campbell, "AlInAsSb Impact Ionization Coefficients," *IEEE Photonics Technol. Lett.*, vol. 31, no. 4, pp. 315–318, 2019, doi: 10.1109/LPT.2019.2894114.

[19] X. Yi *et al.*, "Demonstration of large ionization coefficient ratio in AlAs0.56Sb0.44 lattice matched to InP," *Sci. Rep.*, vol. 8, no. 1, pp. 8–13, 2018, doi: 10.1038/s41598-018-27507-w.

[20] S. Lee *et al.*, "Low noise Al0.85Ga0.15As0.56Sb0.44avalanche photodiodes on InP substrates," *Appl. Phys. Lett.*, vol. 118, no. 8, pp. 0–5, 2021, doi: 10.1063/5.0035571.

[21] I. C. Sandall, S. Xie, J. Xie, and C. H. Tan, "High temperature and wavelength dependence of avalanche gain of AlAsSb avalanche photodiodes," *Opt. Lett.*, vol. 36, no. 21, p. 4287, 2011, doi: 10.1364/ol.36.004287.

[22] S. Xie and C. H. Tan, “AlAsSb avalanche photodiodes with a Sub-mV/K temperature coefficient of breakdown voltage,” *IEEE J. Quantum Electron.*, vol. 47, no. 11, pp. 1391–1395, 2011, doi: 10.1109/JQE.2011.2165051.

[23] K. F. Li *et al.*, “Avalanche multiplication noise characteristics in thin GaAs p+-i-n+ diodes,” *IEEE Trans. Electron Devices*, vol. 45, no. 10, pp. 2102–2107, 1998, doi: 10.1109/16.725242.

[24] R. B. Emmons, “Avalanche-Photodiode Frequency Response,” *J. Appl. Phys.*, vol. 38, no. 9, pp. 3705–3714, Aug. 1967, doi: 10.1063/1.1710199.

[25] A. A. Photodiodes *et al.*, “Design and Characteristics of Guardring-Free Planar,” *Lightwave*, vol. 27, no. 8, pp. 1011–1017, 2009.

[26] A. H. Jones, Y. Yuan, M. Ren, S. J. Maddox, S. R. Bank, and J. C. Campbell, “$Al_xIn_{1-x}As_ySb_{1-y}$ photodiodes with low avalanche breakdown temperature dependence,” *Opt. Express*, vol. 25, no. 20, p. 24340, 2017, doi: 10.1364/oe.25.024340.

[27] M. Ren *et al.*, “Operation Stability Study of AlInAsSb Avalanche Photodiodes,” pp. 159–160, 2017.

[28] X. Yi *et al.*, “Extremely low excess noise and high sensitivity AlAs0.56Sb0.44 avalanche photodiodes,” *Nat. Photonics*, vol. 13, no. 10, pp. 683–686, 2019, doi: 10.1038/s41566-019-0477-4.

[29] B.C. Juang, B. Liang, D. Ren, D. L. Prout, A. F. Chatziioannou, and D. L. Huffaker, “Optical Characterization of AlAsSb Digital Alloy and Random Alloy on GaSb,” *Crystals*, vol. 7, no. 10, 2017, doi: 10.3390/cryst7100313.

[30] M. C. Debnath *et al.*, “Optical properties of bimodally distributed InAs quantum dots grown on digital AlAs0.56Sb0.44 matrix for use in intermediate band solar cells,” *J. Appl. Phys.*, vol. 121, no. 21, p. 214304, Jun. 2017, doi: 10.1063/1.4984832.

[31] E. Hall, H. Kroemer, and L. A. Coldren, “Improved composition control of digitally grown AlAsSb lattice-matched to InP,” *J. Cryst. Growth*, vol. 203, no. 3, pp. 447–449, 1999, doi: https://doi.org/10.1016/S0022-0248(99)00122-0.

[32] Y.H. Zhang, “Accurate control of As and Sb incorporation ratio during solid-source molecular-beam epitaxy,” *J. Cryst. Growth*, vol. 150, pp. 838–843, 1995, doi: https://doi.org/10.1016/0022-0248(95)80057-J.

[33] M. H. Woods, W. C. Johnson, and M. A. Lampert, “Use of a Schottky barrier to measure impact ionization coefficients in semiconductors,” *Solid. State. Electron.*, vol. 16, no. 3, pp. 381–394, 1973, doi: https://doi.org/10.1016/0038-1101(73)90013-0.

[34] D. J. Massey, J. P. R. David, and G. J. Rees, “Temperature dependence of impact ionization in submicrometer silicon devices,” *IEEE Trans. Electron Devices*, vol. 53, no. 9, pp. 2328–2334, 2006, doi: 10.1109/TED.2006.881010.

[35] C.Groves, R.Ghin, J.P.R.David, and G. J. Rees, “Temperature Dependence of Impact Ionization in GaAs,” *IEEE Trans. Electron Devices*, vol. 53, no. 9, pp. 2328–2334, 2006, doi: 10.1109/TED.2006.881010.

[36] C. Groves, C. N. Harrison, J. P. R. David, and G. J. Rees, “Temperature dependence of breakdown voltage in AlxGa 1-xAs,” *J. Appl. Phys.*, vol. 96, no. 9, pp. 5017–5019, 2004, doi: 10.1063/1.1803944.

[37] K. Taguchi, T. Torikai, Y. Sugimoto, K. Makita, and H. Ishihara, “Temperature dependence of impact ionization coefficients in InP,” *J. Appl. Phys.*, vol. 59, no. 2, pp. 476–481, Jan. 1986, doi: 10.1063/1.336655.

[38] Y. Yuan *et al.*, “Temperature dependence of the ionization coefficients of InAlAs and AlGaAs digital alloy: erratum,” *Photonics Res.*, vol. 7, no. 3, p. 273, 2019, doi: 10.1364/prj.7.000273.

[39] A. G. Chynoweth, “Ionization Rates for Electrons and Holes in Silicon,” *Phys. Rev.*, vol. 109, no. 5, pp. 1537–1540, Mar. 1958, doi: 10.1103/PhysRev.109.1537.

[40] B. E. A. Saleh, M. M. Hayat, and M. C. Teich, “Effect of Dead Space on the Excess Noise Factor and Time Response of Avalanche Photodiodes,” *IEEE Trans. Electron Devices*, vol. 37, no. 9, pp. 1976–1984, 1990, doi: 10.1109/16.57159.

[41] R. J. Mclntyre, “A new look at impact lonization-part I: A theory of gain, noise, breakdown probability, and frequency response,” *IEEE Trans. Electron Devices*, vol. 46, no. 8, pp. 1623–1631, 1999, doi: 10.1109/16.777150.

[42] S. A. Plimmer, C. H. Tan, J. P. R. David, R. Grey, K. F. Li, and G. J. Rees, “The effect of an electric-field gradient on avalanche noise,” *Appl. Phys. Lett.*, vol. 75, no. 19, pp. 2963–2965, 1999, doi: 10.1063/1.125202.

[43] X. Zhou, S. Zhang, J. P. R. David, J. S. Ng, and C. H. Tan, “Avalanche Breakdown Characteristics of Al1-xGaxAs0.56Sb0.44 Quaternary Alloys,” *IEEE Photonics Technol. Lett.*, vol. 28, no. 22, pp. 2495–2498, 2016, doi: 10.1109/LPT.2016.2601651.

[44] F. Ma, G. Karve, X. Zheng, X. Sun, A. L. Holmes, and J. C. Campbell, “Low-temperature breakdown properties of AlxGa1−xAs avalanche photodiodes,” *Appl. Phys. Lett.*, vol. 81, no. 10, pp. 1908–1910, Aug. 2002, doi: 10.1063/1.1506012.

[45] A. E. Ishimura and E. Yagyu, “High Sensitivity 2.5/10 Gbps InAlAs Avalanche Photodiodes,” no. September, pp. 17–19, 2009.

[46] D. K. Ferry, “Alloy scattering in ternary III-V compounds,” vol. 17, no. 2, pp. 1–2, 1978.

[47] K. Y. Choo and D. S. Ong, “Positive and negative temperature dependences of electron-impact ionization in In 0.53Ga 0.47As,” *J. Appl. Phys.*, vol. 98, no. 2, 2005, doi: 10.1063/1.1993755.

[48] D. S. Ong, K. F. Li, G. J. Rees, G. M. Dunn, J. P. R. David, and P. N. Robson, “A monte carlo investigation of multiplication noise in thin p+-i-n+ GaAs avalanche photodiodes,” *IEEE Trans. Electron Devices*, vol. 45, no. 8, pp. 1804–1810, 1998, doi: 10.1109/16.704382.

[49] J. S. L. Ong, J. S. Ng, A. B. Krysa, and J. P. R. David, “Temperature dependence of avalanche multiplication and breakdown voltage in Al0.52In0.48P,” *J. Appl. Phys.*, vol. 115, no. 6, pp. 0–6, 2014, doi: 10.1063/1.4865743.

[50] J. C. Phillips, “Ionicity of the chemical bond in crystals,” *Rev. Mod. Phys.*, vol. 42, no. 3, pp. 317–356, 1970, doi: 10.1103/RevModPhys.42.317.

Chapter 5:

Avalanche multiplication and excess noise of $Al_{0.85}Ga_{0.15}As_{0.56}Sb_{0.44}$ at room temperature

5.1 Introduction

Chapter 2 discussed that a feasible way to achieve 1310nm and 1550nm wavelength detection without suffering from high tunnelling current is to have a SACM APD structure. This structure utilizes a narrow band-gap semiconductor to detect light and operate at a low electric field whereas a wider band-gap material as a multiplier operates at high electric field. It is ideal to have two semiconductor materials be lattice matched with each other enabling them to be grown monolithically without the effect of strain occurring at the interface. InGaAs or GaAsSb can be grown on InP substrate in this configuration for telecommunication application APDs. Silicon has been reported to have a large α/β ratio >100 at 150kV/cm[1]and also demonstrated low noise characteristics with very thick structures and operating at very high voltage [2]. Recently, AlInAsSb lattice matched on GaSb exhibited a k_{eff} value of 0.015 at unity gain in a 1μm *i*-region structure [3]. AlInAsSb SACM APD structure can achieve 2μm detection for gas sensing application(CO_2) in the space with a low noise of k_{eff} ~0.01[4].The low noise characteristic observed in Sb-containing material is attributed to the high phonon scattering rate and the heavy effective hole mass associated with the large Sb component[5]. There have been some studies on the excess noise characteristics on $Al_{0.85}Ga_{0.15}As_{0.56}Sb_{0.44}$ with 100nm, 200nm *i*-region thickness p-i-n diodes. The excess noise factor k_{eff} values vary from 0.08 to 0.1 from 87 to 170nm *i*-region thickness p-i-n diodes under pure electrons injection condition[6]. The low noise is observed in these thin structures because it benefits from utilising the dead-space effect. Taylor-Mew et al. reported 600nm *i*-region AlGaAsSb shows subMcInytre excess noise characteristic that F below 2 until M=25 because of the non-uniform electric field[7], [8]. Since the excess noise largely depends on the α/β ratio, and this ratio is getting larger in the low electric field hence lower excess noise, it will be interesting to investigate the bulk thick structure excess noise characteristic for this material.

In Chapter 4, the results demonstrated very low C_{bd} values in AlAsSb. However, this ternary alloy shows high surface leakage current suffering from oxidization. This makes the quaternary alloy $Al_{0.85}Ga_{0.15}As_{0.56}Sb_{0.44}$ (hereafter AlGaAsSb) alloy a better candidate as a SACM multiplier. SACM performance mainly depends on the characteristics of multiplier material. It is important to understand the excess noise and multiplication characteristics of AlGaAsSb.

In this work, α and β are determined over a wide range of electric fields using two digital alloy (DA)and six random alloy (RA) AlGaAsSb p-i-n and n-i-p structures with different avalanching region thicknesses. The electric field-dependent impact ionization coefficients were extracted with a local model, which assumes that the mean distance that a carrier travels before impact ionizing is only a function of the electric field[9]–[11]. By adjusting the α and β fitting parameters, the simulated multiplication results were fitted to the experimental multiplication curve (M_e and M_h). The extraction of the ionization coefficient helps understand the physical mechanisms that lead to low noise in Sb-containing APDs. In addition to the initial study of AlGaAsSb in the thin structures, this work comprehensively studies the excess noise characteristic using a range of wavelengths to yield pure electron and hole injection and mix injection in thick bulk structures. The difference between DA and RA are compared in terms of their multiplication and excess noise characteristics.

5.2 Experimental details

Table 5.1 shows five layers grown by molecular beam epitaxy on a semi-insulating (InP) substrate. Be and Si (or Te) are dopants in p^+ and n^+ cladding layers. In DA, AlGaSb and AlGaAs are the constituent materials to achieve the target fraction of Al, Ga, As and Sb with a target period of 1.3nm. Growing thick RA AlGaAsSb is a challenge because phase separation prevents the formation of a single-phase crystalline alloy [12]. A 400nm/500nm n^{++} InGaAs buffer layer is grown on top of the substrate for DA and RA, respectively. The i-region with different thicknesses is sandwiched between 100nm and 300nm n^+ and p^+ cladding layer in order. A schematic diagram is attached to show the structure of the APD (Figure 5.1). Standard photolithography was used to fabricate the AlGaAsSb APD, followed by wet mesa etching with a mixture of Citric acid: Phosphoric acid: Hydrogen peroxide: Deionised water(40g,10ml,10ml,240ml). Ti/Au (20nm/200nm) is deposited on top and bottom contact layers by electron beam evaporation. SU-8 was used to cover the mesa sidewall for surface passivation. The devices are made into mesa-circles with a diameter of 500µm,350µm,250µm,200µm, and 100µm.

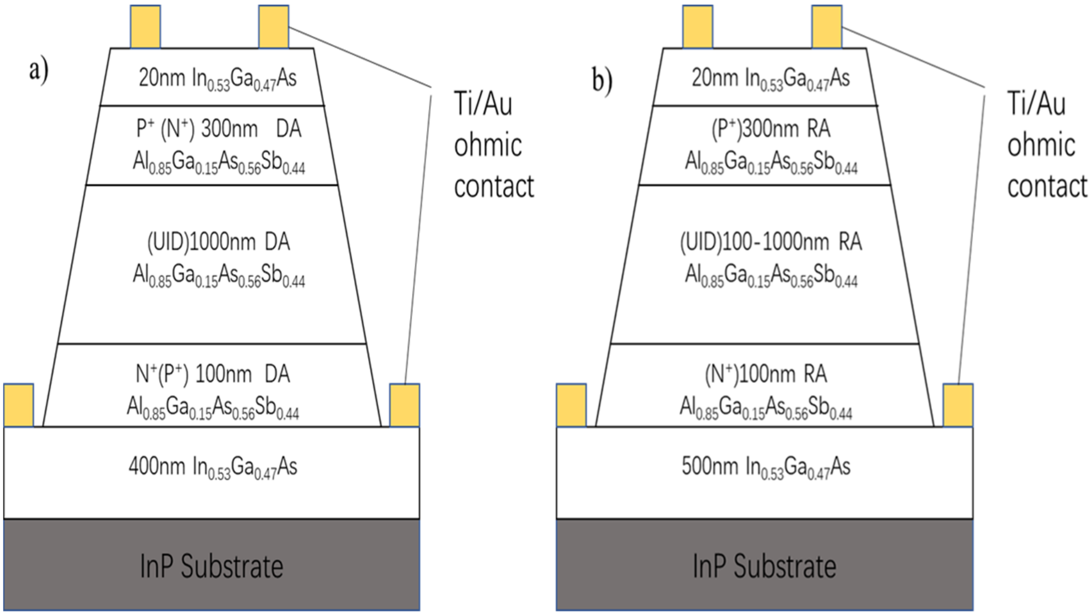

Figure 5.1: A schematic diagram of AlGaAsSb RA and DA structures

5.3 Capacitance-voltage measurements

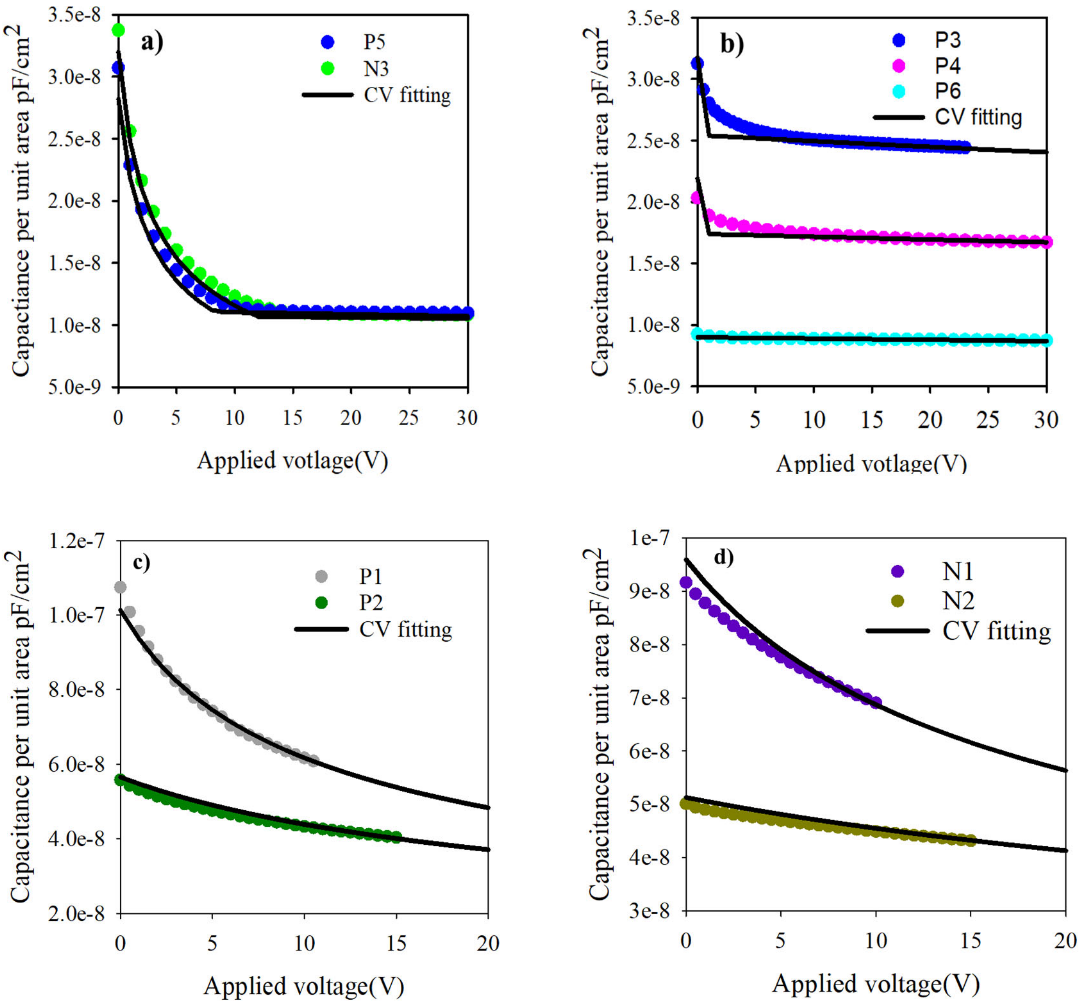

Figure 5.2: a) DA 1µm p-i-n(P5) and 1µm n-i-p(N3) capacitance per unit area. b) RA 0.3µm(P3),0.5µm(P4) and 1µm p-i-n(P6) capacitance per unit area. c) RA 0.1µm p-i-n(P1),0.2µm p-i-n(P2) capacitance per unit area. d) RA 0.1µm n-i-p(P1),0.2µm n-i-p (P2) capacitance per unit area. Solid lines are CV fitting model.

The capacitance-voltage measurements were performed on P3-P6 and N3 with an LCR(HP4275) meter. CV data of P1, P2, N1 and N2 are taken from the literature that Pinel *et al.* reported[6]. Various sizes of devices are measured, and the CV results on each layer scales with the area well, which means the diodes are appropriately isolated. The built-in voltage is estimated to be 1.4V since the built-in voltage determination by plotting $1/C^2$ is only valid in abrupt p-n junction rather than p-i-n structure. The built-in voltage is validated by the forward current measurement where 1.4V is sufficient for the majority carrier to flow and increase exponentially with bias. The permittivity of AlGaAsSb is estimated to be 11.4 from linear interpolation between AlAsSb (10.95) and GaAsSb (14.1) permittivity[13]. The CV fitting data is based on Poisson's equation and the details about CV fitting is shown in appendix A. The calculated thickness and doping level are summarized in table 5.1 and the electric field profile is shown in Figure 5.3. It shows some differences between nominal *i*-region thickness and the actual thickness calculated from the CV measurements. This is attributed to the diffusion of the dopant. The dopant atoms can move from the highly doped cladding layers into the undoped region, which reduce the thickness of the undoped region.

In Figure 5.2, after an initial decrease in capacitance with bias due to the depletion of the *i*-region, the rate of capacitance changing with bias is very small in most of the layers except P5 and N3. This means there is negligible depletion in the cladding because of the high doping level. But the *i*-region background doping is higher in P5 and N3.

Table 5.1: A summary of layers used in this work

Types	Material	Doping (cm^{-3})	Nominal i-region thickness(nm)	CV fitted thickness (nm)
P1(N1)Random alloy p^{+}-i-n^{+} (n^{+}-i-p^{+}) APDs	InGaAs	p^{++} (n^{++})	100	100 (100)
	AlGaAsSb	p^{+}: 1.5×10^{18} (n^{+}: 2.4×10^{18})		300 (300)
	AlGaAsSb	UID		87 (98)
	AlGaAsSb	n^{+}: 1.5×10^{18} (p^{+}: 2.4×10^{18})		200 (200)
	InGaAs	n^{++} (p^{++})		1000 (1000)
	Semi-insulating InP substrate			
P2(N2)Random alloy p^{+}-i-n^{+} (n^{+}-i-p^{+}) APDs	InGaAs	p^{++} (n^{++})	200	100 (100)
	AlGaAsSb	p^{+}: 1.25×10^{18} (n^{+}: 2.4×10^{18})		300 (300)
	AlGaAsSb	UID		170 (193)
	AlGaAsSb	n^{+}: 1.25×10^{18} (p^{+}: 2.4×10^{18})		200 (200)
	InGaAs	n^{++} (p^{++})		1000 (1000)
	Semi-insulating InP substrate			
P3Random alloy p^{+}-i-n^{+} APDs	InGaAs	p^{++}	400	20
	AlGaAsSb	p^{+}: 1.5×10^{18}		300
	AlGaAsSb	UID [5.5×10^{15}]		397
	AlGaAsSb	n^{+}: 1.5×10^{18}		100
	InAlAs	n^{++}		500
	Semi-insulating InP substrate			

P4 Random alloy p^{+}-i-n^{+} APDs	InGaAs	p^{++}	500	20
	AlGaAsSb	p^{+}: 1×10^{18}		300
	AlGaAsSb	UID [2.5×10^{15}]		590
	AlGaAsSb	n^{+}: 1×10^{18}		100
	InAlAs	n^{++}		500
	Semi-insulating InP substrate			
P5(N3)Digital alloy p^{+}-i-n^{+} (n^{+}-i-p^{+}) APDs	InGaAs	p^{++} (n^{++})	1000	20 (20)
	AlGaAsSb	p^{+}: 1×10^{18} (n^{+}: 1×10^{18})		300 (300)
	AlGaAsSb	UID [1.5×10^{16} (1.9×10^{16})]		890 (890)
	AlGaAsSb	n^{+}: 1×10^{18} (p^{+}: 1×10^{18})		100 (100)
	InGaAs	n^{++} (p^{++})		400 (400)
	Semi-insulating InP substrate			
(P6)Random alloy p^{+}-i-n^{+} APDs	InGaAs	p^{++}	1000	20
	AlGaAsSb	p^{+}: 1×10^{18}		300
	AlGaAsSb	UID [1×10^{15}]		1020
	AlGaAsSb	n^{+}: 1×10^{18}		100
	InGaAs	n^{++}		500
	Semi-insulating InP substrate			

The i-region doping level is estimated to be 1×10^{15} cm^{-3} to 1.9×10^{16} cm^{-3} for different layers, and the cladding layer doping is about 1×10^{18}. The structure with thin avalanche regions was fully depleted by its built-in voltage (P1, N1, P2, N2, P3 and P4). In contrast, the thicker structures with higher background doping fully depleted at 8V(P5), 12(N3) and 5V for P6.

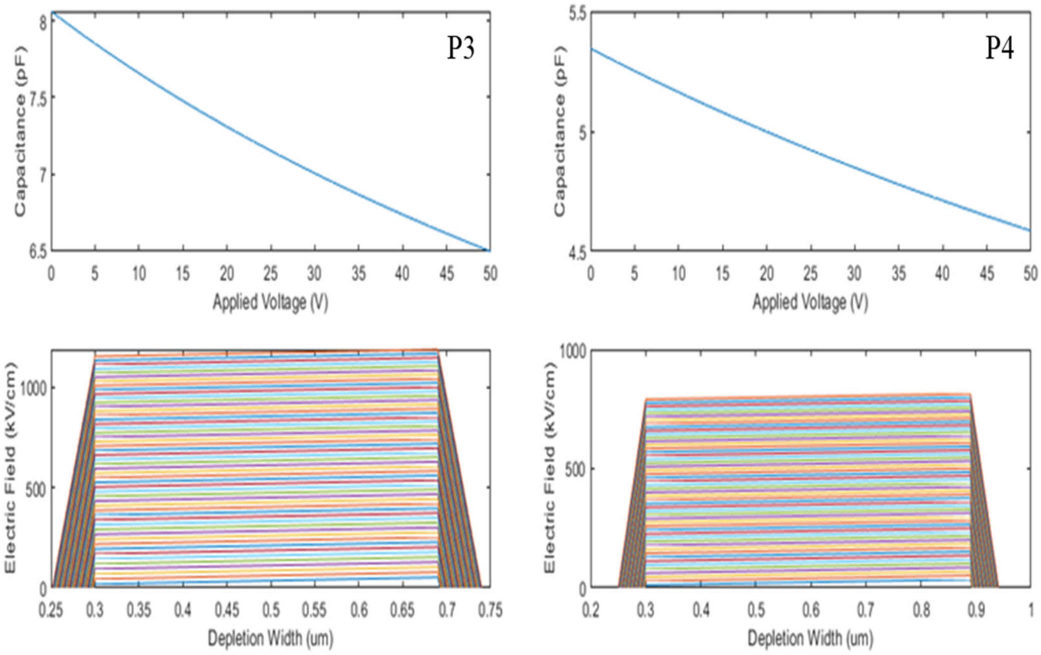

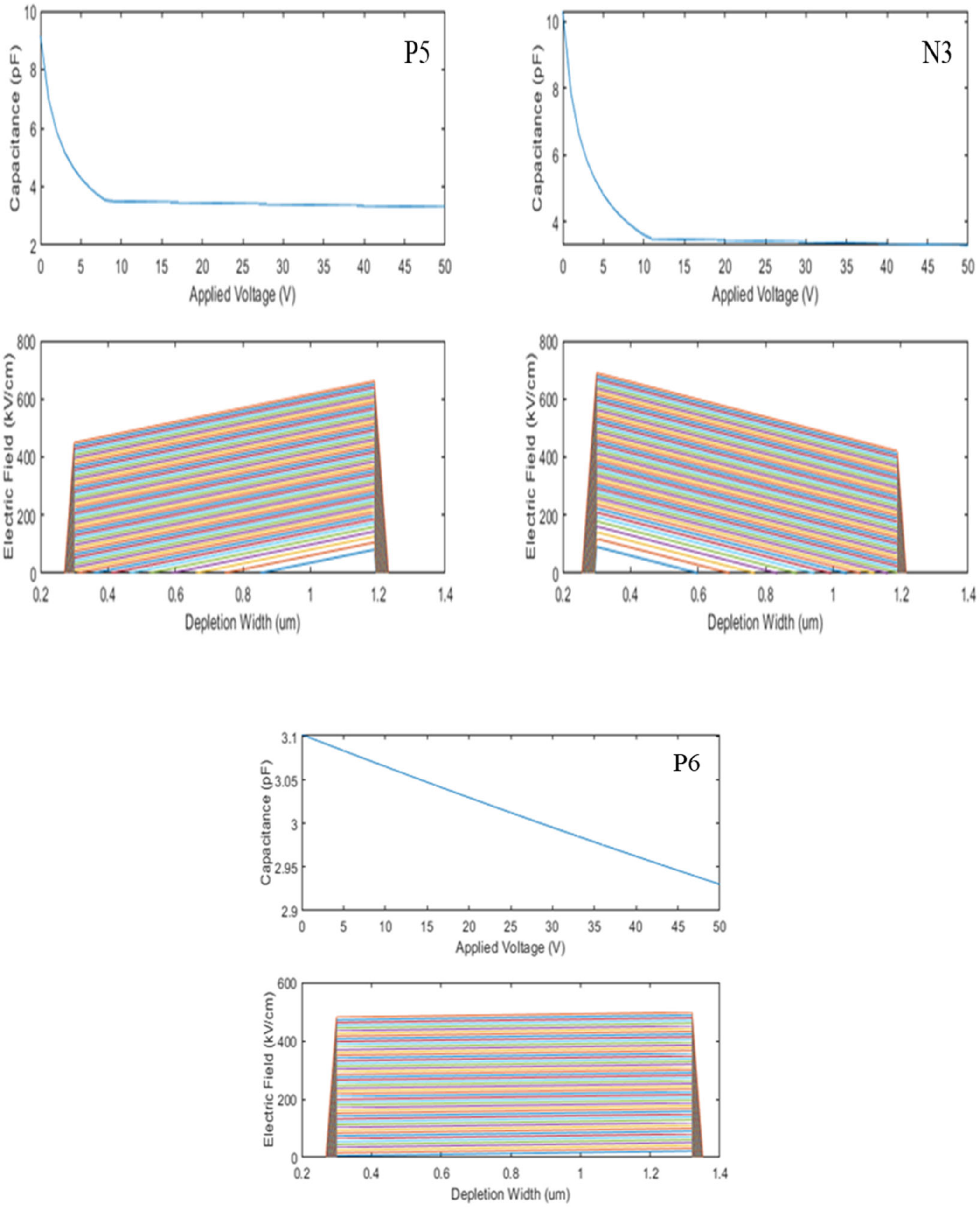

Figure 5.3: Simulated Electric field and C-V for P2-P6 and N3 with 200μm diameter devices from 0V to 50V with a step of 1V (part figure in previous page for clarity).

5.4 Current-voltage measurements

Dark IV measurements were performed on all the layers. Some of dark I-V measurements are shown for example. Surface dark current dominates the total current before 0.5V, and then bulk dark current dominates. In Figure 5.4a, the dashed grey lines show that the diode for the bulk current region has an ideality factor of around 1.8, suggesting the mechanism is generation and recombination. The series resistance is small since the forward current can reach 1mA promptly. Dark forward current density is shown in Figure 5.4b, the large surface current is present at low bias, and it is becoming bulk dominated when high forward bias is applied, and they start to scale with the area.

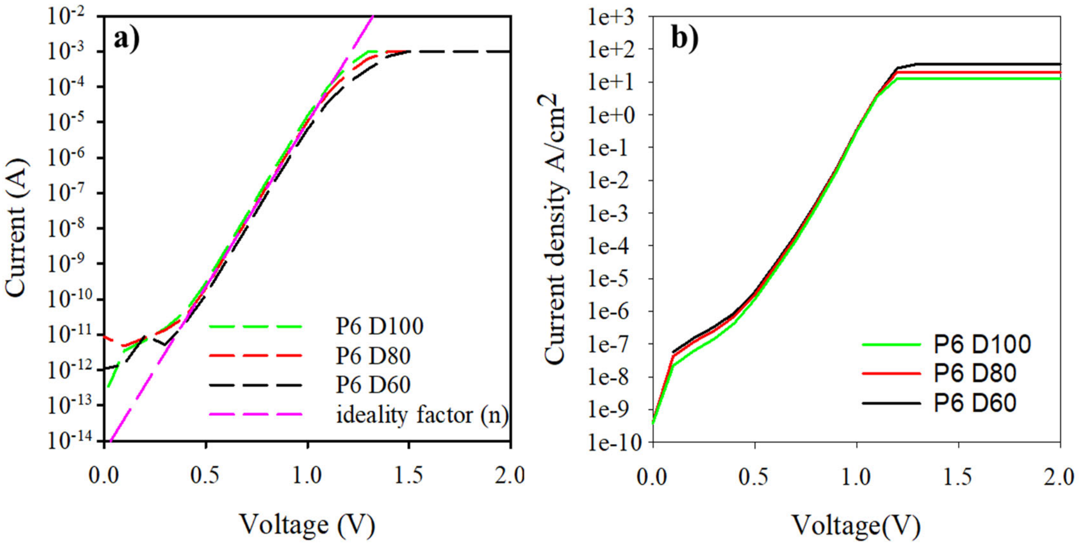

Figure 5.4: a) Forward dark current on P6 b) Forward dark current density on P6. (Pink dash line represents the ideality factor fitting)

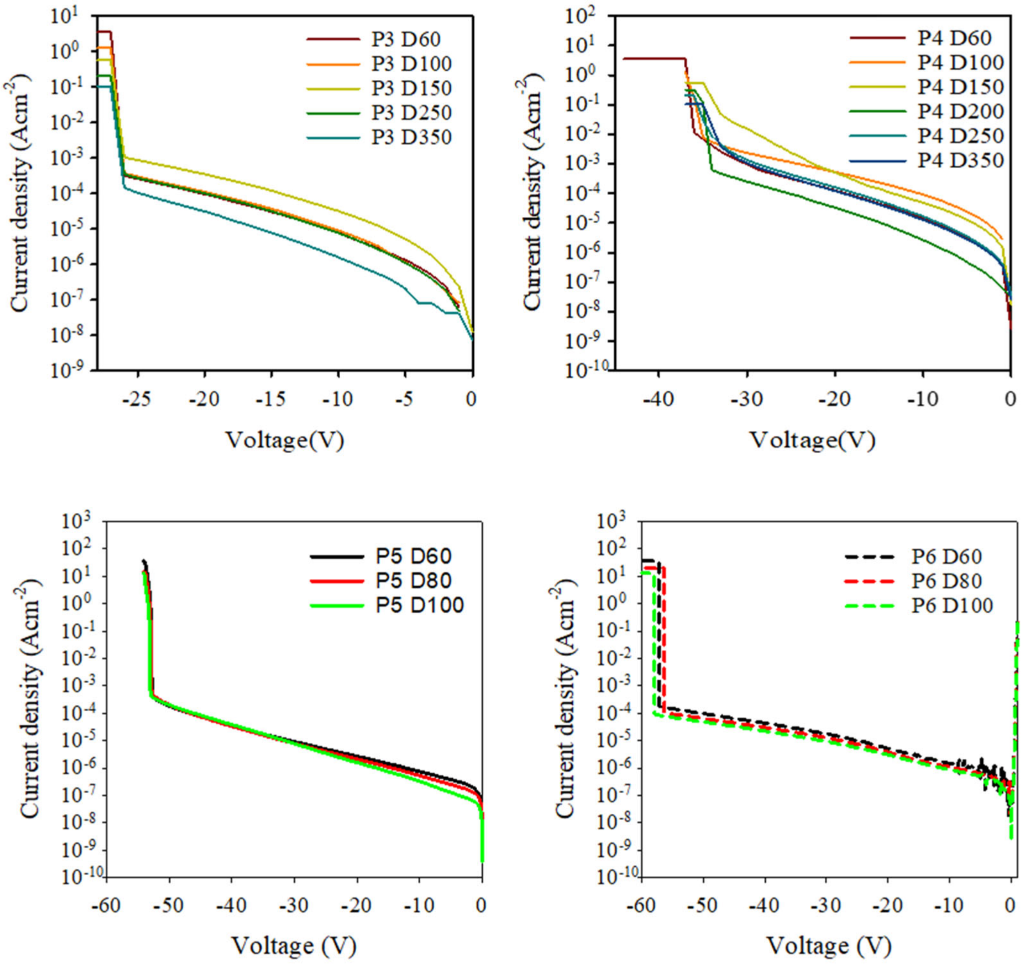

Figure 5.5: Reverse dark current measurements on P3-P6 with various sizes

Figure 5.5 and Figure 5.6 show measurements of dark reverse I-V for P3 to P4 and N3. From reverse dark current measurements, it shows a sharp breakdown in all structures except the P4 shows some variation due to edge breakdown. All layers show a certain level of surface leakage current because they do not scale with the area well except P5. The cause of surface leakage current is most likely due to the formation of Al oxide and Sb oxide during the device fabrication. The surface leakage current can be suppressed with some passivation technique during the fabrication[14], [15]. The reverse dark current in P5 scale with the area above 30V. However, the surface leakage current dominates the dark current below 30V. The dark current in P6 does not change much with device size, which suggests this is not true bulk dark current. Although AlGaAsSb has some surface leakage component, it still shows 10 times reduction in dark current compared to AlAsSb reported previously[16].

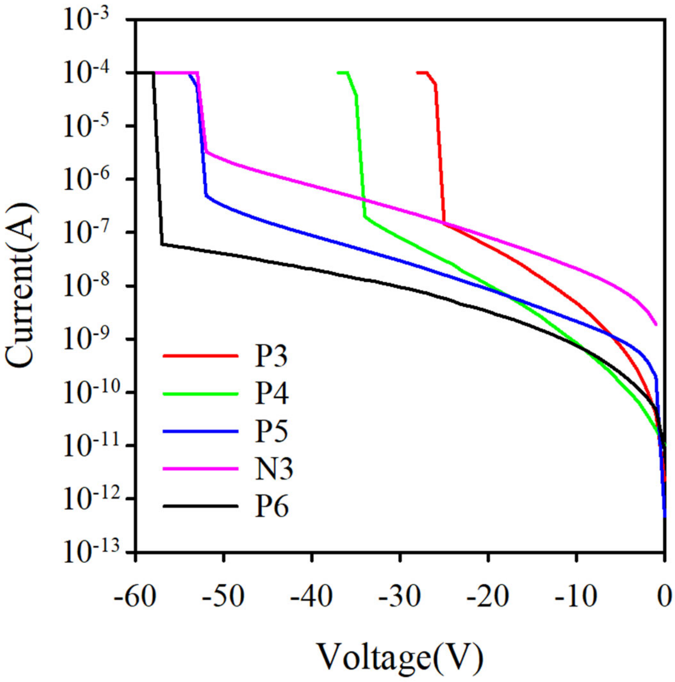

Figure 5.6: Typical room temperature reverse dark I-V for 200μm diameter devices for P3-P6 and N3.

The bulk dark current will also be multiplied in APD. The total dark current then can be defined as:

$$I_d = I_s + M \times I_b \tag{5.1}$$

Where I_d is the total dark current, M is the avalanche multiplication and I_b is the dark current.

Figure 5.7 shows some examples of the measured total dark versus multiplication. Equation 5.1 is used to fit the measured dark current, and extract I_s and I_b values for each layer. The I_s about 10 times higher than I_b in P5, whereas in P4 the surface leakage current is reduced and I_b is taking a larger portion of the total current. The surface leakage has been reduced by about 100 times compared to AlAsSb(2.13×10^{-6})[17]. The I_d can be rewritten into following:

$$I_d = A\pi D + B\pi D^2/4 \tag{5.2}$$

Where A is the surface dark current per unit length, B is the bulk dark current per unit area, and D is the diameter of the APD.

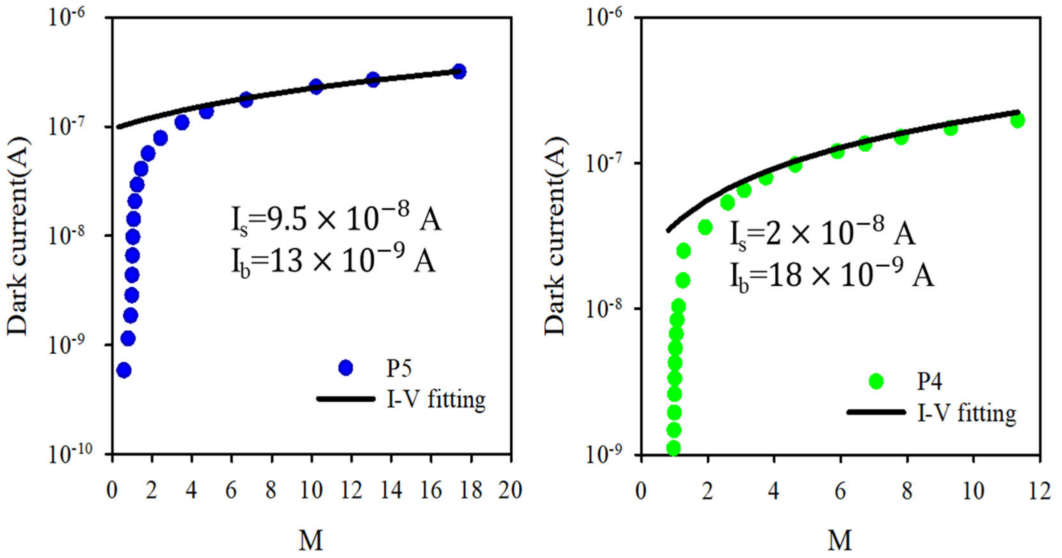

Figure 5.7: Measured I_d versus M at 450nm for P4 and P5 with 200μm diameter device

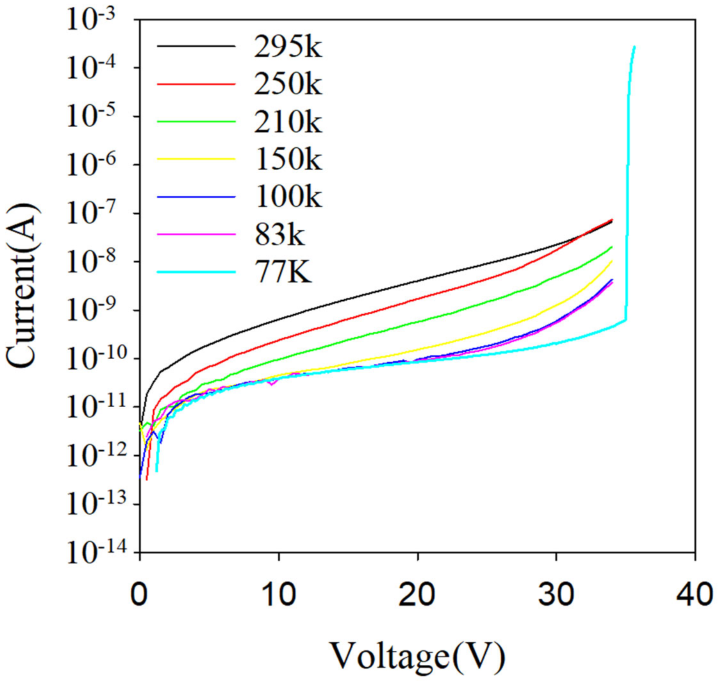

Figure 5.8: Temperature dependence reverse I-V for P4 with 200μm diameter device.

The temperature-dependent characteristics are carried out to prove that the surface leakage current dominates the dark current, as shown in Figure 5.8. The reverse dark current is reduced by 100 times as the temperature goes down. Dark current at each temperature is fitted with equation 5.1. It was found that surface dark current does not change with temperature significantly. This suggests the low-temperature dark current is higher than the actual bulk dark current and can be reduced more by optimizing the fabrication process and sidewall passivation.

5.5.1 Avalanche multiplication measurements

The photomultiplication measurements methods are described in Chapter 3. Different wavelength light (450nm,532nm,633nm and 780nm) are used on all the layers. A Lock-in amplifier is used to measure the relative change of the photocurrent on different devices with various diameters to ensure the repeatability of the results and the multiplication measurement is free from power dependence. The laser spot(<100μm) is focused on top of the 200μm diameter device to ensure most of the light is absorbed by the optical window instead of the mesa sidewalls. Due to the large conduction band offset, carriers generated in the top 20nm InGaAs do not contribute to the photocurrent. The absorption coefficient is demonstrated by Guo et al.[18], Figure 5.9 shows the absorption decay profile of different wavelengths. For 455nm wavelengths light with an absorption coefficient of 1.15×10^7 , 99% of the light is absorbed in the 300nm top $p^+(n^+)$ cladding layer and 780nm wavelength with an absorption coefficient of 4.1×10^4 is almost uniformly absorbed in a 1μm structure.

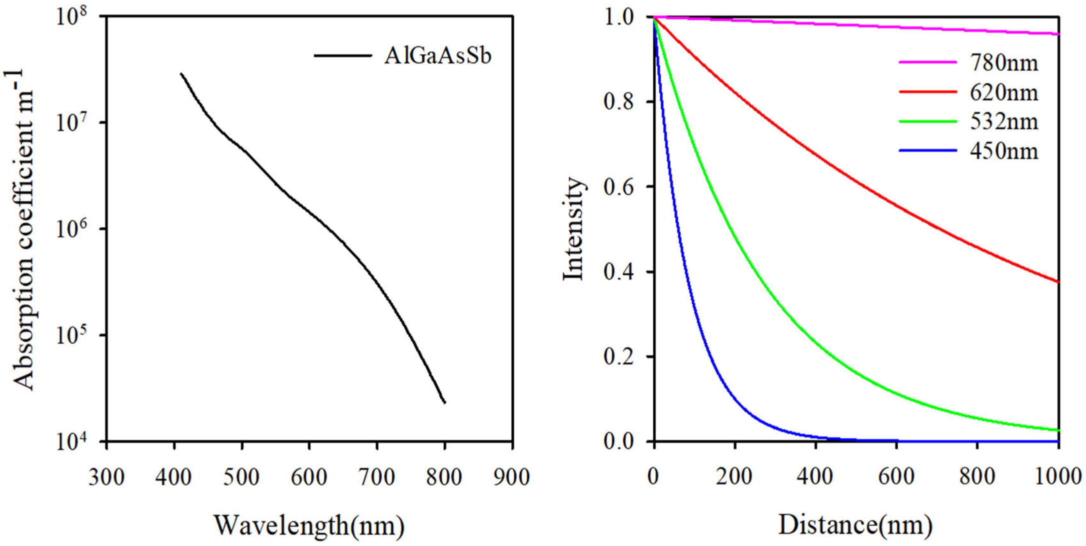

Figure 5.9: Absorption coefficients of AlGaAsSb[18] and absorption decay profile for different wavelengths.

The magnitude of the photocurrent output from the lock-in amplifier depends on the optical power of the light source, absorption profile and diffusion length. The multiplication in all measurements are determined by correcting the increase in photocurrent due to the movement of the depletion edge in the highly doped cladding layers [19]. Figure 5.10 shows an example of ‘cosh’ function correction (green dash line). This line defines the primary photocurrent increase with increasing in responsivity due to the depletion edge moving. The Woods’ correction requires complicated fitting with several parameters, including doping level and diffusion length. The simplified linear baseline (red line) in Figure 5.10 can closely agree with the Woods correction, Figure 5.10b shows negligible difference between Woods’ baseline and linear baseline correction. And linear baseline correction method is used in all other multiplication analysis.

The multiplication is obtained by calculating the ratio of total photocurrent (I_{ph}) in blue circle over the primary photocurrent (I_{pr}).

$$M = \frac{I_{ph}}{I_{pr}} \tag{5.10}$$

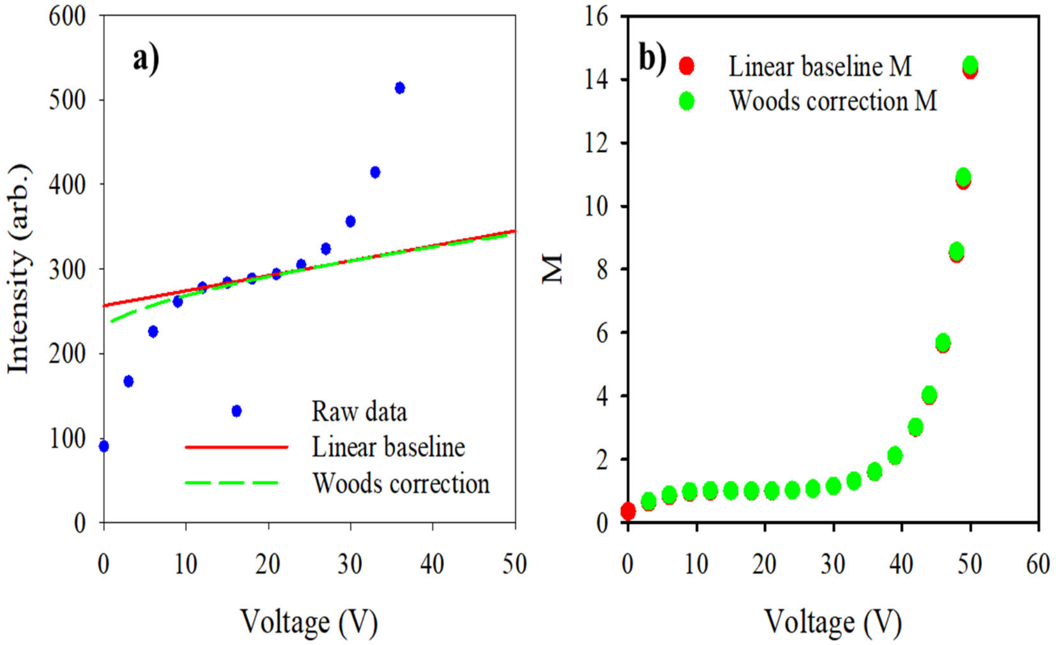

Figure 5.10: a) Example of baseline correction for avalanche multiplication) Corrected multiplication after different baseline correction.

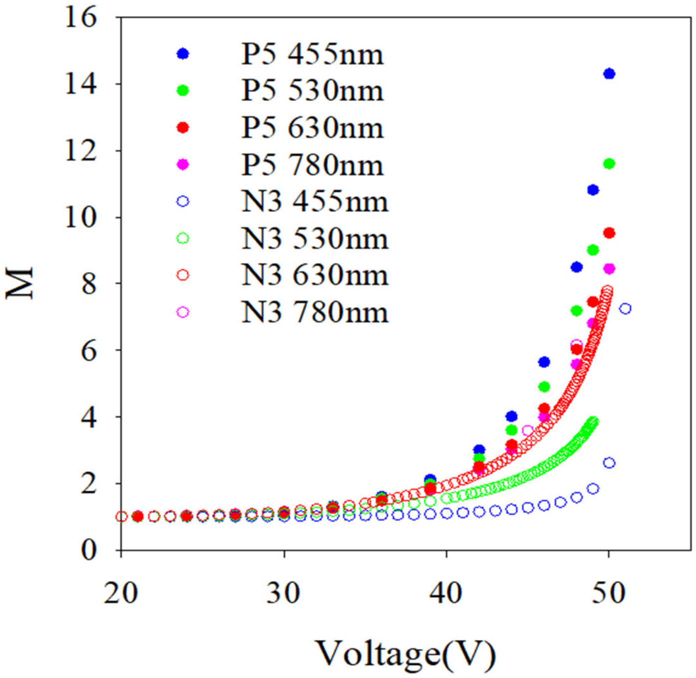

Figure 5.11: Example of corrected multiplication curve on P5 and N3 with different wavelengths on a 200µm diameter device.

Figure 5.11 shows some examples of a corrected multiplication curve on P5 and N3 with different injection profiles. It shows the multiplication goes up with an increase of voltages (electric field) exponentially. The rate of multiplication increase is slower as the wavelength goes longer from 450nm to 780nm. The opposite trend was observed in the complementary n-i-p structure. In the p-i-n structure, the injection profile shown in Figure 5.9 demonstrates the change from pure electron injection to mix carrier injection as the wavelength increase from 450nm to 780nm, which results in smaller multiplication values (M_e to M_{mix}). However, the n-i-p structures change from pure hole injection to mix carrier injection as the wavelength goes longer and results in larger multiplication (M_h to M_{mix}). This clearly indicates that the electron ionization coefficient is larger than the hole ionization coefficient($\alpha>\beta$) in AlGaAsSb because of $M_{mix} < M_e$ in the p-i-n structure and $M_{mix}>M_h$ in the n-i-p structures. In addition, there is hardly any avalanche multiplication measurable near breakdown voltage in N3 under pure hole injection conditions. Significant differences between P5 pure electron (M_e) and N3 hole multiplication (M_h) can be observed. All of this support the conclusion drawn from p-i-n structures the hole impact ionization event is extremely small at a low electric field and $\alpha>>\beta$ in AlGaAsSb.

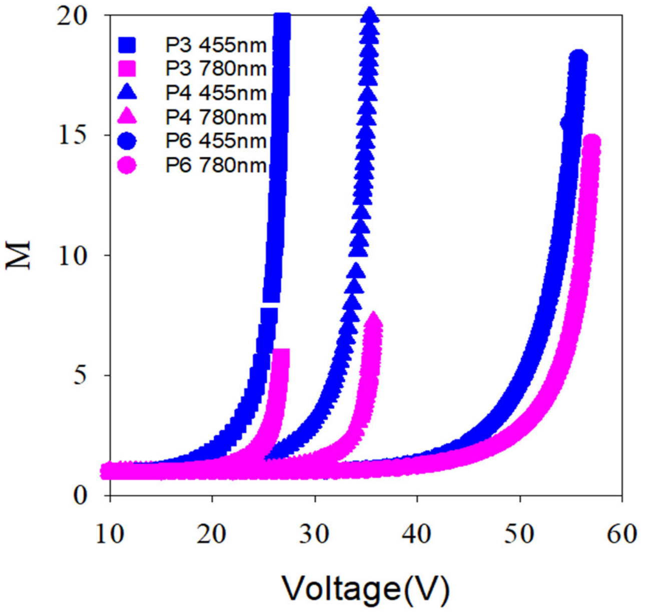

Figure 5.12: Avalanche multiplication for P3, P4 and P6 with 455nm and 780nm wavelength on 200µm diameter device.

Figure 5.12 shows the multiplication on three different thickness p-i-n structures. They all show some wavelength dependence characteristics. In theory, most III-V semiconductors have α and β approaching unity at high electric field[10], [20]. This effectively means the wavelength-dependent characteristic is supposed to be smaller as the avalanching region becomes thinner. The difference between M_e and M_{mix} is getting larger from 300nm i-region(P3) to 500nm i-region(P4) structure, but it shows a much smaller discrepancy in 1000nm structure(P6). The InAlAs buffer layers at the bottom can be the reason to address this issue. In P3 and P4, the direct bandgap InAlAs layer at the bottom has a reasonable absorption at 780nm, and the bandgap offset is small between AlGaAsSb and InAlAs. Holes generated at the bottom of InAlAs can travel back to the avalanche region, effectively making the multiplication more like M_h. But in P6, the large bandgap offset between the InGaAs and AlGaAsSb stops holes from crossing the barriers.

5.5.2 Impact ionization coefficients

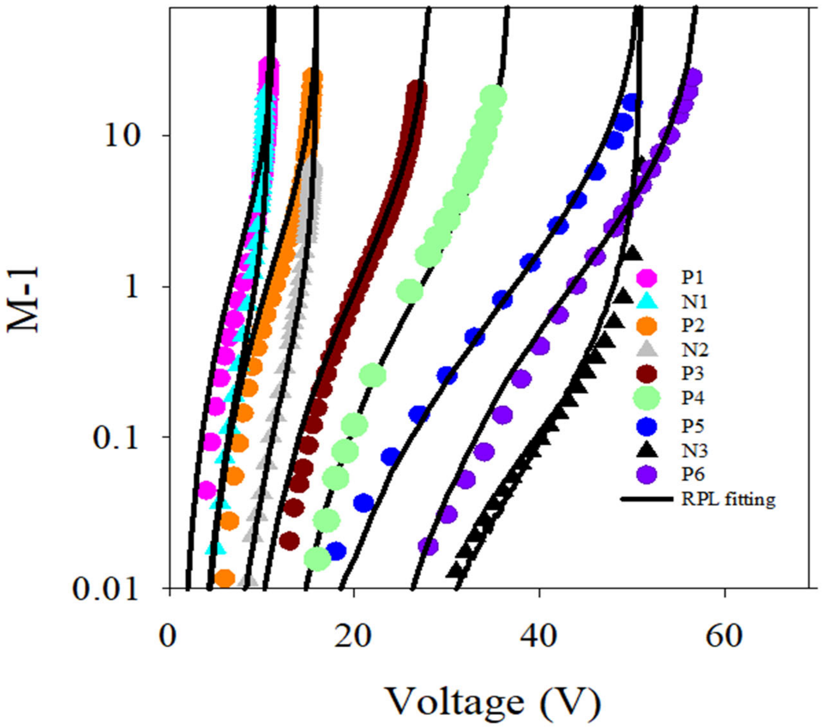

Figure 5.13:M-1 for P1-P6 and N1-N3 under pure injection conditions [6].

The impact ionization coefficients as a function of the electric field are determined using multiplication results shown in Figure 5.13. A numerical technique (RPL model)[9] is used to generate the multiplication curve from M=1.01 to 50 based on an accurate knowledge of the electric field profiles in the range of the structure investigated by using the trial and error fitting methods, which enable the best fit between the experimental data and simulation results. This model considers the tapered electric field profile but not the carrier history and dead-space effects[21]. This means the impact ionization coefficients are assumed to be a function only of the local electric field in the structures. The electric field as a function of the position is calculated based on the C-V results summarized in table 5.1.

The pure electron(p-i-n) and hole(n-i-p) initiated multiplication (M_e and M_h) are simulated using these impact ionization coefficients below with the RPL model for all eight structures. In Figure 5.13, it shows good agreement between the measured and simulated multiplication curve over three orders of magnitude. It also shows excellent agreements at the very low gain value of M=1.01. Although the measurable M_h is small in N3, the good agreements with the model down to M_h=1.01 also suggest the low electric field data for β is correct. The expression for impact ionization coefficients valid from 260-1000kV/cm for α and 200-1000kV/cm for β,

$$\alpha = \begin{cases} 5.5 \times 10^5 \exp\left(-\left(\frac{1.21\times10^6}{E}\right)^{1.43}\right) \text{cm}^{-1}, \\ \text{when } 260\text{kV/cm} < E < 500\text{kV/cm} \\ 8.0 \times 10^5 \exp\left(-\left(\frac{1.30\times10^6}{E}\right)^{1.43}\right) \text{cm}^{-1}, \\ \text{when } 500\text{kV/cm} < E < 1000\text{kV/cm} \end{cases}, \quad (5.11)$$

$$\beta = \begin{cases} 2.5 \times 10^5 \exp\left(-\left(\frac{1.70\times10^6}{E}\right)^{1.44}\right) \text{cm}^{-1} \\ \text{when } 200\text{kV/cm} < E < 500\text{kV/cm} \\ 4.5 \times 10^5 \exp\left(-\left(\frac{1.92\times10^6}{E}\right)^{1.38}\right) \text{cm}^{-1} \\ \text{when } 500\text{kV/cm} < E < 1000\text{kV/cm} \end{cases} \quad (5.12)$$

Where E is the electric field in kV/cm

The ionization coefficients as a function of the inverse electric field, AlGaAsSb α/β (solid black lines), reach 1000 at an electric field below 350kV/cm, as shown in Figure 5.14. The AlGaAsSb ionization coefficients were found to be very similar to AlAsSb at low electric field (<500 kV/cm). There is a slight change in bandgap between AlAsSb and AlGaAsSb, the X-valley bandgap change from 1.64eV to 1.56eV and the Γ-valley bandgap changes from 1.95 eV to 1.77 eV[22]. The similar electron impact ionization coefficients but not larger hole impact ionization coefficients observed in AlGaAsSb and AlAsSb is due to the small change in the bandgap. Similar studies were reported in

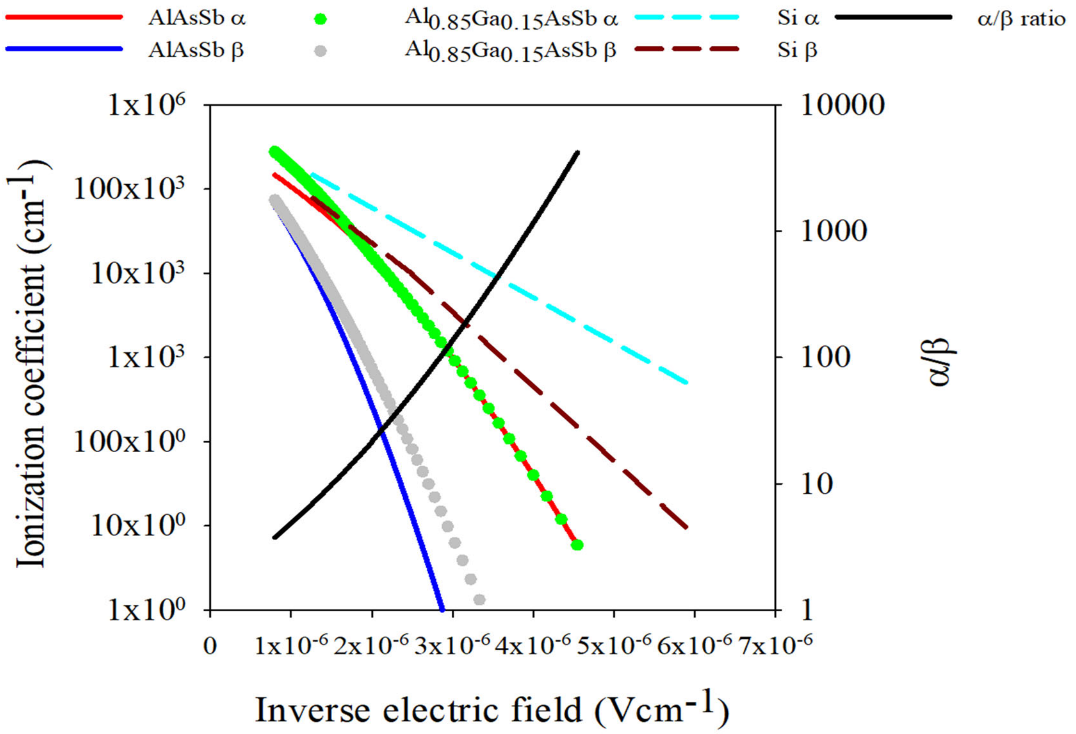

Figure 5.14:Impact ionization coefficients of electrons and holes for AlGaAsSb, AlAsSb[16], Si[1] and InAlAs[23].

$Al_xGa_{1-x}As$ and $(Al_xGa_{1-x})_{0.52}In_{0.48}P$ lattice matched to GaAs, which shows the breakdown voltage and impact ionization coefficients do not change much with Al composition variation when the Al composition is high[10]. It was found that α in AlGaAsSb, AlAsSb, InAlAs and InP (not shown for clarity) are very similar over a wide electric field range. At a given electric field of 350 kV/cm, the α in all materials are 1648 cm^{-1}, however, β shows large differences with β=3300cm^{-1} in InP, 167cm^{-1} in InAlAs, 19 cm^{-1} in AlGaAsSb and 1.5cm^{-1} in AlAsSb.

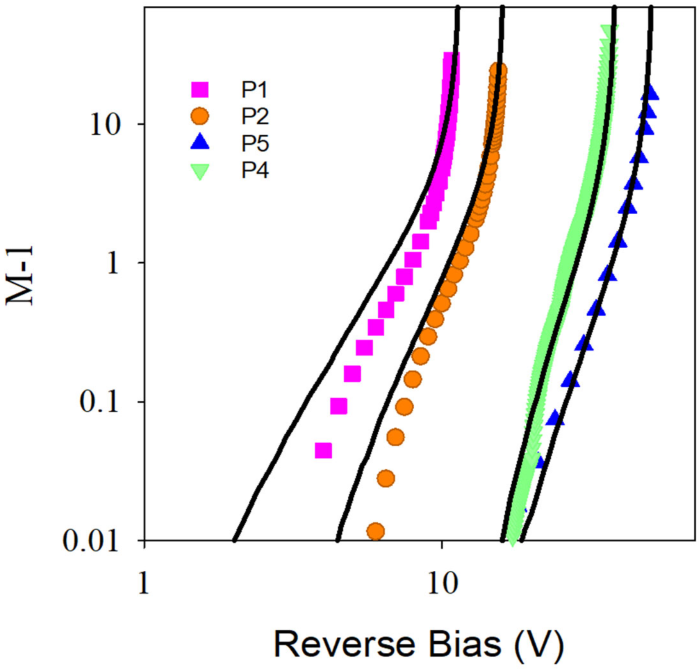

Figure 5.15:M-1 and simulated gain curve from the RPL model for P1,P2,P4 and P5 on log voltage scale axis.

Previously, the impact ionization coefficient shown in Figure 5.14 appeared capable of generating the avalanche multiplication in all devices listed in table 5.1, including those structures with very thin avalanche regions. Figure 5.15 shows an expanded scale at low values. It shows local model overestimated the electron-initiated multiplication (M_e) at low values of multiplication in P1 and P2. This strongly indicates the effect of 'dead-space', the minimum distance carriers need to travel in the avalanche region to be in equilibrium with the high electric field. The dead-space effect suppresses the onset electron ionization at low field multiplication in very thin structures. This is also observed in other structures, for example, AlGaAs[24]. This effect is more significant in thin structures. It becomes less critical when the avalanche region width is 600nm or larger because the dead space becomes a smaller portion of the total avalanche region width when it becomes the avalanche region gets thicker. Plimmer *et al.*[25] demonstrated an in-depth analysis of the avalanche multiplication on GaAs p-i-n structures with the local model. It shows the local model work well for structures with an i-region greater than 200nm after comparing the results with Monte Carlo Models.

5.6 Excess noise on AlGaAsSb

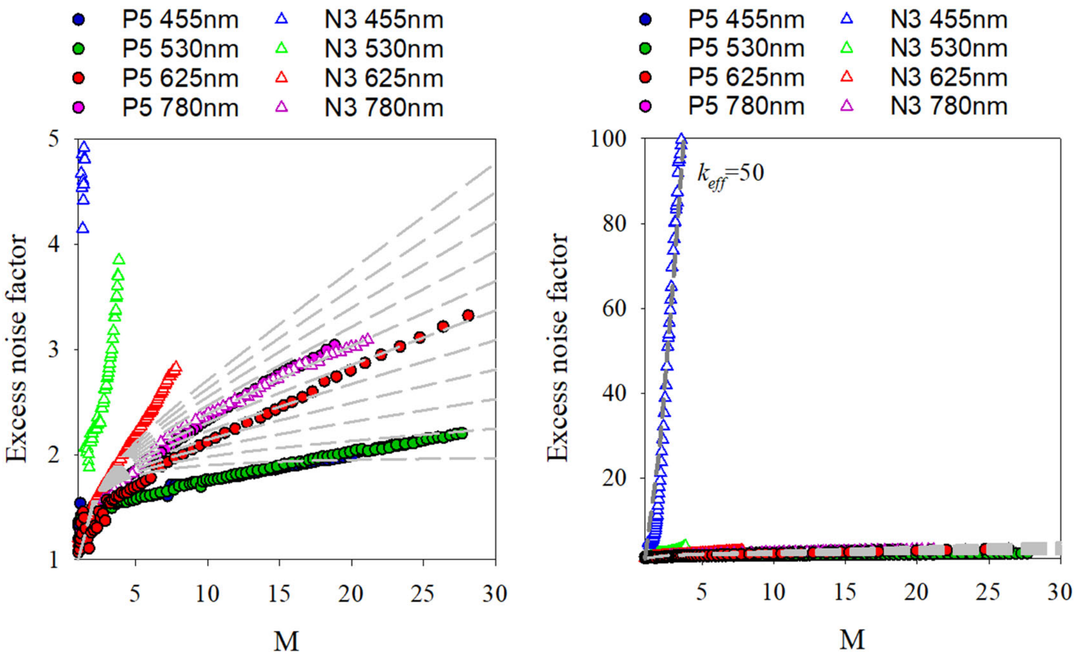

Figure 5.16: Excess noise data for the P5 and N3 with different injection conditions for a 200µm diameter device. Right: Rescaled plot to show the pure injection excess noise in N3. The grey dash lines are McIntyre lines from 0 to 0.1 in steps of 0.01.

The excess noise measurements set up is discussed in detail in chapter 3. This was performed at a centre frequency of 10Mhz±4Mhz circuit by Lau et al. [26]. A silicon p-i-n diode is used to calibrate and remove the effect of system noise. Photocurrent was measured using a trans-impedance amplifier of the noise measurements system, and avalanche multiplication is determined by linear baseline correction as discussed in the previous section. Different wavelength fibre-coupled LEDs are used to illuminate the device to avoid noise from the light source associated with lasers. In addition, LEDs are availability of a wide range of wavelengths and that the optical power doesn't drift. Gas laser can drift a little bit and result in laser power fluctuations. This makes the measurement more difficult since there is external noise source other than the APD noise. Same as the avalanche multiplication measurements, the different wavelengths are used to vary the injection profile and compare the difference in output excess noise characteristics at different multiplication values.

Figure 5.16 shows P3 and N3 excess noise measurements with different wavelengths on a 200µm diameter device. In the p-i-n structure, as the wavelength increases from 455nm to 780nm, the injection profile from pure injection to mix injection profile increases the excess noise factor. However, the opposite trend is observed in the n-i-p structures, noise decreases with increased wavelength. The excess noise factor in both p-i-n(P5) and n-i-p(N3) are very similar with a uniform injection profile(780nm). It is equivalent to k_{eff}=0.06 in McIntyre's local model. It is important to note that the pure injection excess noise factor in N3 is extremely high which is equivalent to k_{eff} =50 according to McIntyre's local model. This is reduced to k_{eff}=1 when the injection profile is slightly mixed(530nm). In the p-i-n structure, 530nm wavelength excess noise does not increase much compared to 455nm, this also suggest the electrons are dominating impact ionization process. All the observations indicate that $\alpha>>\beta$, and this conclusion is consistent with the results obtained with the avalanche multiplication and prior work[6].

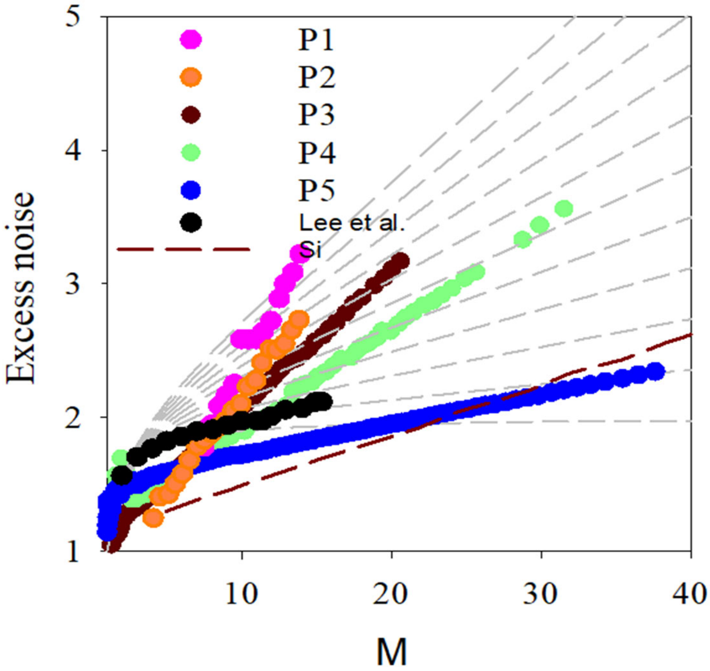

Figure 5.17: Excess noise data for different thickness RA AlGaAsSb p-i-n structures with pure injection profile(450nm) on a 200µm device. Black symbol from Lee et al.[27] Red dash line is commercial silicon APD[28]

Figure 5.17 shows the excess noise measurements in different avalanche region thicknesses with pure injection(450nm) profile. The increase in excess noise with decreased avalanche region width is likely due to the α and β converge at the high electric field region. Even with the benefits of the dead-space effect, the excess noise in P1 and P2 are much higher than for P6 structures. It is essential to optimize the structure's thickness to achieve high sensitivity and speed with large α/β ratio.

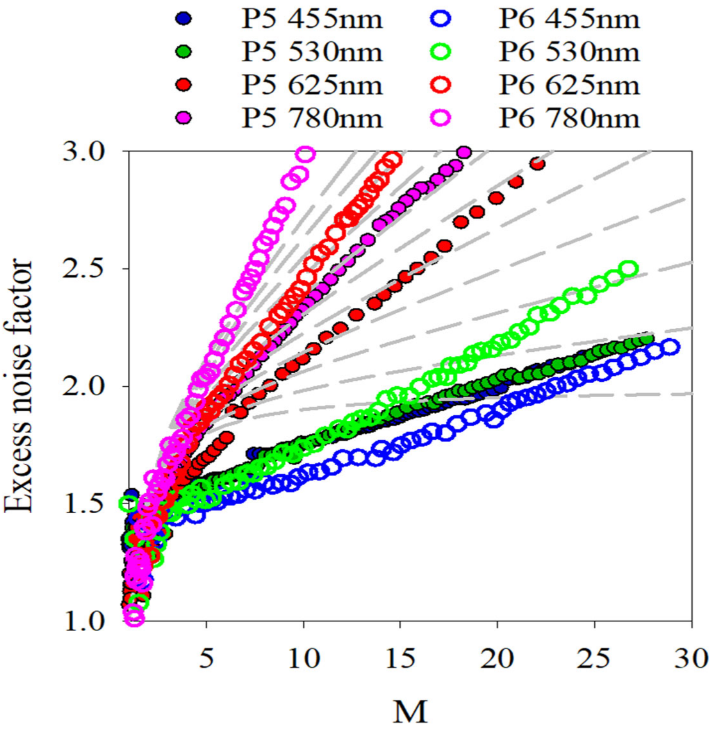

Figure 5.18: Excess noise measurement in P5(DA) and P6(RA) structures with various of wavelengths on a 200μm device. Grey dash lines represent McIntyre's local model for k_{eff} values of 0 to 0.1 in steps of 0.01.

Figure 5.18 shows the variation in excess noise for varying injection conditions in digital alloy and random alloy P5 and P6, respectively. The excess noise for RA measurements meets the k_{eff}=0 at the multiplication of 20 and k_{eff} =0.1 at the multiplication of 30. The excess noise is below k_{eff}=0 line when M<20 for both RA and DA. The pure injection excess noise is very similar in both RA and DA. The discrepancy could be due to the difference in i-region thickness and operating electric field. And the excess noise increases faster with the increase of wavelength in DA compared to RA.

5.7 Discussion on avalanche multiplication and excess noise

Figure 5.14 shows the large impact ionization coefficient ratio in AlGaAsSb. The electron ionization coefficient is similar to other materials like InAlAs, whereas the hole ionization coefficients have been significantly reduced. The presence of Sb atoms can lead to the reduction in hole ionization coefficient. In most semiconductor materials, Holes can gain energy rapidly until when ionize when holes gain energy and scatter from the heavier heavy/light hole bands. The split-off band was pushed down in the alloy band structure deeper into the valance band due to the spin-orbit coupling effect when the large group V Sb atoms present. Thus, the spin-orbit splitting energy($\triangle_{so}$) increase[29]. Because of the increased $\triangle_{so}$, it is unlikely for holes in the heavy/light hole bands scatter into the split-off band before reach the edge of Brillouin zone edge. As a result, this suppresses the hole ionization rate. This creates a large difference between α and β, leading to a low k_{eff} value observed in the excess noise measurements. Moreover, the excess noise in P6 is comparable to commercial Si APDs, as shown in Figure 5.17[30]. In Figure 5.19, this spin-orbit theory has been demonstrated recently in GaAsBi by Liu et al.[31] that large Bi atom has a strong spin-orbit effect on increasing $\triangle_{so}$ which makes it harder for holes to scatter from the heavy/light hole bands into the split-off band where most of the hole impact ionization happened, hence reducing the β.

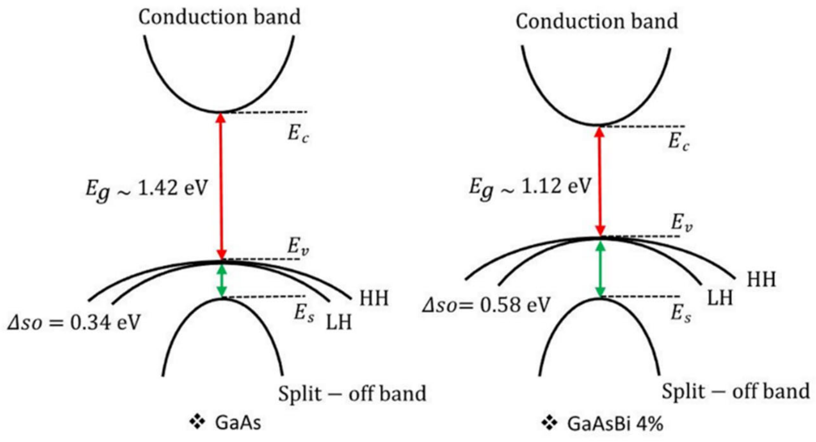

Figure 5.19: A schematic diagram to show the effect of adding Bi to GaAs in spin split-off energy[31].

Both avalanche multiplication and excess noise suggest no significant difference in impact ionization coefficients between DA and RA AlGaAsSb. However, there is a difference from the previous study of the impact ionization coefficient on InAlAs alloy[32]. The $\triangle_{so}$ is very similar in DA and RA, which are 0.45eV and 0.5eV, respectively. The $\triangle_{so}$ is much larger in this Sb-containing quaternary alloy than in other non-Sb-containing alloys (InP, InAlAs). Minigaps in DA can effectively compensate for the small difference because of these periodic structures that localize holes and prevent hole impact ionization from occurring [33]. Consequently, both DA and RA have similar α/β ratio and excess noise characteristics.

The excess noise results in P5 is different to those reported previously[27]. Despite the results that differ from McIntyre's local model predicted, this is expected to be true in an alloy once the effects of dead space are significant. The probability density function is not perfectly represented by an exponential decay. A lower proportion of electrons as primary charge carriers can overestimate the avalanche multiplication a lower noise, as is expected in an alloy where α is much greater than β. This may well explain the difference in noise measurements reported.

Thin structures (P1 and P2) show lower excess noise in low multiplication region because of dead space. However, F increase more quickly with multiplication than McIntyre's local model predicts because the α and β converge at the high electric field. In contrast, thicker structure can operate at an electric range where α and β are still reasonably large. The local model can then be more closely approximated as the dead space is smaller relative to the total width of the high field region, resulting in better performance in thick avalanche region structure.

It is important to choose an avalanche region that is appropriate for device applications. For an application such as Telecommunications, it only requires operating multiplication at M=10 or less, and then a thinner structure can be a good candidate since it has low excess noise at low multiplication region and also benefits from the higher operating bandwidth of a thinner structure. For an application like single photon detector (SPAD) which requires much higher gain(M>1000), a thicker structure is preferable since the excess noise increase slower with increase of multiplication. This can also provide more responsivity for better sensitivity.

5.8 Conclusion

In summary, both electrical and optical characteristics of AlGaAsSb have been measured in a series of structures with avalanching regions from 87nm to 1020nm. From these, surface leakage current has been reduced by 10 times from AlAsSb to AlGaAsSb, improving the noise equivalent power (NEP). The ionization coefficient extracted from avalanche multiplication measurements shows a large α/β ratio. Low excess noise measured in pure injection profile because of the presence of Sb atoms. No significant difference between the ionization coefficient between random alloy and digital alloy. The parameterized impact ionization coefficients can replicate the multiplication characteristic of avalanching region width >200nm. For thinner structure, it would require taking dead space into account to predict the low values of electron multiplication accurately. The demonstration of extremely low noise comparable with Silicon and sub-McIntyre behavior enables a significant improvement in useful multiplication in APD, hence sensitivity in receiver operating at a very high error bit rate. For an application such as Lidar, where bandwidth is not crucial, the much lower k_{eff} values should enhance the signal-to-noise ratio of AlGaAsSb-based APD over existing material systems. Optimizing the multiplication region width is important to achieve the lowest excess noise possible for the actual application. This provides useful information for further SACM designs.

5.9 References

[1] H. D. E. Man, “Measurement of the ionization rates in diffused silicon p-n junctions,” *Microelectron. Reliab.*, vol. 9, no. 6, p. 462, 1970, doi: 10.1016/0026-2714(70)90205-2.

[2] HAMAMATSU, “High-sensitivity Si APD for detection of light with a wavelength of 266 nm,” Ichino-cho, 2018. [Online]. Available: http://hamamatsu.com/resources/products/ssd/pdf/tech/si_apd_technical_information.pdf.

[3] M. E. Woodson, M. Ren, S. J. Maddox, Y. Chen, S. R. Bank, and J. C. Campbell, “Low-noise AlInAsSb avalanche photodiode,” *Appl. Phys. Lett.*, vol. 108, no. 8, 2016, doi: 10.1063/1.4942372.

[4] A. H. Jones *et al.*, “Room-temperature bandwidth of 2-µm AlInAsSb avalanche photodiodes,” *Opt. Express*, vol. 29, no. 23, p. 38939, 2021, doi: 10.1364/oe.439240.

[5] X. Yi *et al.*, “Extremely low excess noise and high sensitivity AlAs0.56Sb0.44 avalanche photodiodes,” *Nat. Photonics*, vol. 13, no. 10, pp. 683–686, 2019, doi: 10.1038/s41566-019-0477-4.

[6] L. L. G. Pinel *et al.*, “ Effects of carrier injection profile on low noise thin Al 085 Ga 015 As 056 Sb 044 avalanche photodiodes ,” *Opt. Express*, vol. 26, no. 3, p. 3568, 2018, doi: 10.1364/oe.26.003568.

[7] J. Taylor-Mew, V. Shulyak, B. White, C. H. Tan, and J. S. Ng, “Low Excess Noise of Al0.85Ga0.15As0.56Sb0.44Avalanche Photodiode from Pure Electron Injection,” *IEEE Photonics Technol. Lett.*, vol. 33, no. 20, pp. 1155–1158, 2021, doi: 10.1109/LPT.2021.3110123.

[8] J. D. Taylor-Mew, J. D. Petticrew, C. H. Tan, and J. S. Ng, “Simulation of Al0.85Ga0.15As0.56Sb0.44 avalanche photodiodes,” *Opt. Express*, vol. 30, no. 11, pp. 17946–17952, May 2022, doi: 10.1364/OE.458922.

[9] D. S. Ong, K. F. Li, G. J. Rees, J. P. R. David, and P. N. Robson, “A simple model to determine multiplication and noise in avalanche photodiodes,” *J. Appl. Phys.*, vol. 83, no. 6, pp. 3426–3428, Mar. 1998, doi: 10.1063/1.367111.

[10] H. I. J. Lewis *et al.*, “Impact Ionization Coefficients in (AlxGa1-x)0.52In0.48P and AlxGa1-xAs Lattice-Matched to GaAs,” *IEEE Trans. Electron Devices*, vol. 68, no. 8, pp. 4045–4050, 2021, doi: 10.1109/TED.2021.3086800.

[11] X. Jin *et al.*, “Temperature Dependence of the Impact Ionization Coefficients in AlAsSb Lattice Matched to InP,” *IEEE J. Sel. Top. Quantum Electron.*, vol. 28, no. 2, 2022, doi: 10.1109/JSTQE.2021.3099912.

[12] J. R. Pessetto and G. B. Stringfellow, “AlxGa1−xAsySb1−y phase diagram,” *J. Cryst. Growth*, vol. 62, no. 1, pp. 1–6, 1983, doi: https://doi.org/10.1016/0022-0248(83)90002-7.

[13] Silvaco Inc., “Atlas User’s Manual,” 2016. [Online]. Available: https://dynamic.silvaco.com/dynamicweb/jsp/downloads/DownloadManualsAction.do?req=silen-manuals&nm=atlas.

[14] H. Kim, R. M. Thompson, V. Tilak, T. R. Prunty, J. R. Shealy, and L. F. Eastman, “Effects of SiN passivation and high-electric field on AlGaN-GaN HFET degradation,” *IEEE Electron Device Lett.*, vol. 24, no. 7, pp. 421–423, 2003, doi: 10.1109/LED.2003.813375.

[15] A. Olziersky *et al.*, “Insight on the SU-8 resist as passivation layer for transparent Ga2O3–In2O3–ZnO thin-film transistors,” *J. Appl. Phys.*, vol. 108, no. 6, p. 64505, Sep. 2010, doi: 10.1063/1.3477192.

[16] X. Yi *et al.*, “Demonstration of large ionization coefficient ratio in AlAs0.56Sb0.44 lattice matched to InP,” *Sci. Rep.*, vol. 8, no. 1, pp. 8–13, 2018, doi: 10.1038/s41598-018-27507-w.

[17] X. Yi, “Impact ionization in AlAs0.56Sb0.44 photodiodes,” University of Sheffield, 2020.

[18] B. Guo *et al.*, “Optical constants of Al0.85Ga0.15As0.56Sb0.44 and Al0.79In0.21As0.74Sb0.26,” *Appl. Phys. Lett.*, vol. 119, no. 17, pp. 0–5, 2021, doi: 10.1063/5.0062035.

[19] M. H. Woods, W. C. Johnson, and M. A. Lampert, “Use of a Schottky barrier to measure impact ionization coefficients in semiconductors,” *Solid. State. Electron.*, vol. 16, no. 3, pp. 381–394, 1973, doi: https://doi.org/10.1016/0038-1101(73)90013-0.

[20] D. J. Massey, J. P. R. David, and G. J. Rees, “Temperature dependence of impact ionization in submicrometer silicon devices,” *IEEE Trans. Electron Devices*, vol. 53, no. 9, pp. 2328–2334, 2006, doi: 10.1109/TED.2006.881010.

[21] S. A. Plimmer, J. P. R. David, and D. S. Ong, “The merits and limitations of local impact lonization theory,” *IEEE Trans. Electron Devices*, vol. 47, no. 5, pp. 1080–1088, 2000, doi: 10.1109/16.841244.

[22] X. Zhou, S. Zhang, J. P. R. David, J. S. Ng, and C. H. Tan, “Avalanche Breakdown Characteristics of Al1-xGaxAs0.56Sb0.44 Quaternary Alloys,” *IEEE Photonics Technol. Lett.*, vol. 28, no. 22, pp. 2495–2498, 2016, doi: 10.1109/LPT.2016.2601651.

[23] Y. L. Goh *et al.*, “Avalanche Multiplication in InAlAs,” vol. 54, no. 1, pp. 11–16, 2007.

[24] B. K. Ng *et al.*, “Avalanche multiplication characteristics of Al/sub 0.8/Ga/sub 0.2/As diodes,” *IEEE Trans. Electron Devices*, vol. 48, no. 10, pp. 2198–2204, 2001, doi: 10.1109/16.954454.

[25] S. A. Plimmer *et al.*, “Investigation of impact ionization in thin GaAs diodes,” *IEEE Trans. Electron Devices*, vol. 43, no. 7, pp. 1066–1072, 1996, doi: 10.1109/16.502416.

[26] K. S. Lau *et al.*, “Excess noise measurement in avalanche photodiodes using a transimpedance amplifier front-end,” *Meas. Sci. Technol.*, vol. 17, no. 7, pp. 1941–1946, 2006, doi: 10.1088/0957-0233/17/7/036.

[27] S. Lee *et al.*, “Low noise Al0.85Ga0.15As0.56Sb0.44avalanche photodiodes on InP substrates,” *Appl. Phys. Lett.*, vol. 118, no. 8, pp. 0–5, 2021, doi: 10.1063/5.0035571.

[28] Hamamatsu, “Si APD S10341,” 2018. [Online]. Available: https://www.hamamatsu.com/content/dam/hamamatsu-photonics/sites/documents/99_SALES_LIBRARY/ssd/s10341_series_kapd1030e.pdf.

[29] A. Science, “A Multiscale Study of P-I-N Devices for Computing and Sensing Applications,” no. December, 2021.

[30] R. J. McIntyre, “Multiplication noise in uniform avalanche diodes,” *IEEE Trans. Electron Devices*, vol. ED-13, no. 1, pp. 164–168, 1966, doi: 10.1109/T-ED.1966.15651.

[31] Y. Liu *et al.*, “Valence band engineering of GaAsBi for low noise avalanche photodiodes,” *Nat. Commun.*, vol. 12, no. 1, 2021, doi: 10.1038/s41467-021-24966-0.

[32] Y. Yuan *et al.*, “Temperature dependence of the ionization coefficients of InAlAs and AlGaAs digital alloy: erratum,” *Photonics Res.*, vol. 7, no. 3, p. 273, 2019, doi: 10.1364/prj.7.000273.

[33] J. Zheng *et al.*, “Digital Alloy InAlAs Avalanche Photodiodes,” *J. Light. Technol.*, vol. 36, no. 17, pp. 3580–3585, 2018, doi: 10.1109/JLT.2018.2844114.

Chapter 6

GaAsSb/AlGaAsSb SACM APD at room temperature

6.1 Introduction

There is a significant growth in interest in Lidar systems for applications ranging from space-borne instruments for greenhouse gas emission monitoring to accurate 3D-sensing and mapping in urban environments for next-generation fully-autonomous vehicles[1], [2]. Avalanche photodiodes (APDs) are used in these photon-starved applications because they can provide high detection sensitivity due to their internal multiplication. However, due to the impact ionization process's stochastic nature, excess noise comes with multiplication while the signal is being amplified. McIntyre's local field theory describes the excess noise increase with multiplication as

$$F(M) = k_{eff}M + (1 - k_{eff})\left(2 - \frac{1}{M}\right) \tag{6.1}$$

where $k_{eff}=\beta/\alpha$ (hole ionization coefficient over electron ionization coefficient if $\alpha>\beta$).

The excess noise will limit the useful multiplication provided by the APD. It is important to select a material with a small k_{eff} so that the multiplication can be larger before the signal noise ratio gets reduced by excess noise, hence the sensitivity.

Silicon APD receivers are commonly used at 905nm in Lidar systems due to their high sensitivity, reliability, and low cost. However, the Lidar system's wavelength is limited by the bandgap (E_g) of Si (<1100nm), and these wavelengths are not considered eye safe. Recently, developing a lidar system that can operate at 1550nm is attracting a high level of interest because high laser power can be used since it is eye safe. It is less affected by the solar background radiation (1550nm has less solar noise than 905nnm by about 78%)[3].

The best commercially available APD at 1550nm is made of an InGaAs absorber and InP multiplier in a separate absorption, charge, and multiplication structure (SACM). The typical operating multiplication in these Hamamatsu-made APDs is M=30 with F>10 [5][6]. This limits the performance of APDs due to their high noise and low multiplication.

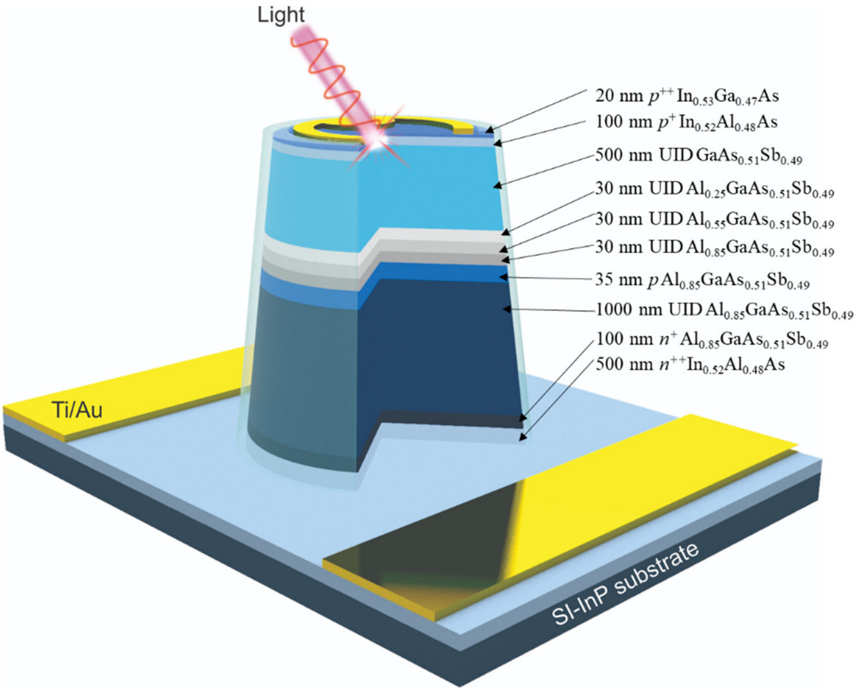

Figure 6.1: Heterostructure schematic of the GaAsSb/AlGaAsSb SACM APD grown by solid source molecular beam epitaxy (MBE)

The excess noise and multiplication characteristic of AlGaAsSb p-i-n diodes with different avalanche region thicknesses have been discussed in Chapter 5. As a conclusion, 1µm p-i-n structure shows low excess noise and is suitable for lidar application since it requires to operate at high multiplication value. In this work, an SACM architecture using a novel $GaAs_{0.5}Sb_{0.5}/Al_{0.85}Ga_{0.15}As_{0.56}Sb_{0.44}$ (GaAsSb/AlGaAsSb) structure is presented, which has significant improvements in multiplication and excess noise for operation at 1550nm. This structure is shown in Figure 6.1. In this design, the AlGaAsSb multiplier operates at high electric field (<600kv/cm) for carriers to gain energy and impact ionize, while the GaAsSb absorber operates at a low electric field (<200kV/cm) to reduce the effect of tunnelling leakage current as shown in Figure 6.2. There is a large conduction band offset between the

GaAsSb and the AlGaAsSb, a grading scheme changes the Al composition gradually can bridge the conduction band offset between the GaAsSb and AlGaAsSb. This SACM structure is designed based on results shown in the previous chapter and new work on the GaAsSb absorber.

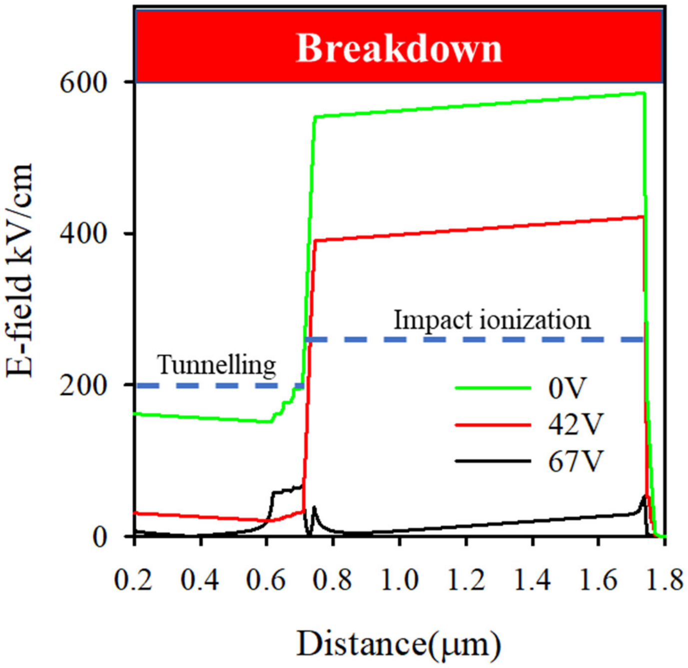

Figure 6.2: Modelled electric field profile of the structure showing the GaAsSb in the low field region below the tunnelling threshold(200kV/cm) and the AlGaAsSb multiplication region in the high field region to obtain large avalanche gain.

Using GaAsSb as an absorber instead of conventional InGaAs is one of the novelties of this SACM structure. There are only a few studies on GaAsSb for detector applications [7], [8]. The advantages of using GaAsSb over InGaAs are that the conduction and valance bands in the AlGaAsSb alloy can change continuously from the GaAsSb absorber to the AlGaAsSb multiplier without any large bandgap discontinuity. This grading scheme makes it easier for carriers to travel between heterojunction interfaces, minimizes carrier trapping, and improves the device’s speed. Additionally, it is easier to grade from GaAsSb to AlGaAsSb while maintaining lattice-matched growth as it is mainly the group III composition that needs to change. InGaAs to AlAsSb requires InAlGaAs and InAlAs grading layers [9]. This is because InGaAs and

AlGaAsSb has a type II band alignment which then results in a larger conduction band offset (~1eV) between the last layers of grading ($In_{0.52}Al_{0.48}As$) and the AlGaAsSb multiplication region[10]. Therefore, no comparably simple and efficient grading is possible with an InGaAs absorber.

6.2 Experimental details

The SACM APD was grown on a semi-insulating InP substrate using a random alloy growth technique. For group V cells, RIBER VAC 500 and Veeco Mark V valved crackers were used for As and Sb, respectively. Various calibration runs were performed by changing the growth rate, V/III bream equivalent pressure (BEP) ratio and growth temperature to achieve low background doping in the absorber and multiplication region. Be and Si are used as p type dopant and n type dopant respectively. Devices are fabricated with conventional photolithography and wet etching process to delineate a clear mesa shape of the devices. Mesa sidewalls are covered with SU-8 to passivate and reduce surface leakage current. To make ohmic contacts, Ti/Au was deposited on the bottom and top contact layers. The detail of the SACM structure is shown in Figure 6.1, and structures of other p-i-n diodes used in this work are shown in table 6.1.

Table 6.1: Summary of layers used in this study

Types	Material	Doping (cm^{-3})	Thickness (nm)
P7	GaAsSb	$p^{++}: 1\times10^{19}$	20
	AlInAs	$p^{+}: 2\times10^{18}$	150
	GaAsSb	UID	1000
	GaAsSb	$n^{+}: 2\times10^{18}$	100
	AlInAs	$n^{++}: 1\times10^{19}$	500
	Semi-insulating InP substrate		
P8	InGaAs	$p^{++}: 1\times10^{19}$	20
	AlInAs	$p^{+}: 2\times10^{18}$	150

	GaAsSb	UID	1800
	GaAsSb	$n^{+}: 2\times10^{18}$	100
	AlInAs	$n^{++}: 1\times10^{19}$	500
	Semi-insulating InP substrate		
P3	InGaAs	$p^{++}: 1\times10^{19}$	20
	AlGaAsSb	$p^{+}: 2\times10^{18}$	300
	AlGaAsSb	UID	390
	AlGaAsSb	$n^{+}: 2\times10^{18}$	100
	AlInAs	$n^{++}: 1\times10^{19}$	500
	Semi-insulating InP substrate		
P4	InGaAs	$p^{++}: 1\times10^{19}$	20
	AlGaAsSb	$p^{+}: 2\times10^{18}$	300
	AlGaAsSb	UID	590
	AlGaAsSb	$n^{+}: 2\times10^{18}$	100
	AlInAs	$n^{++}: 1\times10^{19}$	500
	Semi-insulating InP substrate		
P6	InGaAs	$p^{++}: 1\times10^{19}$	20
	AlGaAsSb	$p^{+}: 2\times10^{18}$	300
	AlGaAsSb	UID	1020
	AlGaAsSb	$n^{+}: 2\times10^{18}$	100
	InGaAs	$n^{++}: 1\times10^{19}$	500
	Semi-insulating InP substrate		

Note: All grown layers are nearly lattice-matched to InP substrates.

$In_{0.53}Ga_{0.47}As$ (InGaAs), $Al_{0.48}In_{0.52}As$ (AlInAs), $GaAs_{0.51}Sb_{0.49}$ (GaAsSb), $Al_{0.85}Ga_{0.15}AsSb$ (AlGaAsSb)

6.3 Results

6.3.1 Absorption in GaAsSb

Two p-i-n structures P7 and P8 (Details in table 6.1) were grown with different i-region thicknesses of 1000nm and 1800nm to examine the performance of the GaAsSb absorber, especially the external quantum efficiency (EQE). Figure 6.3 shows the capacitance-voltage measurement on P7 and P8. The actual avalanche region thickness and background doping are extracted by fitting the experimental (C-V) to an electric field solver based on Poisson's equation with a dielectric constant of 14.1[11] and details are given in table 6.1. The background doping concentrations in P7 and P8 are as low as 1×10^{15}.

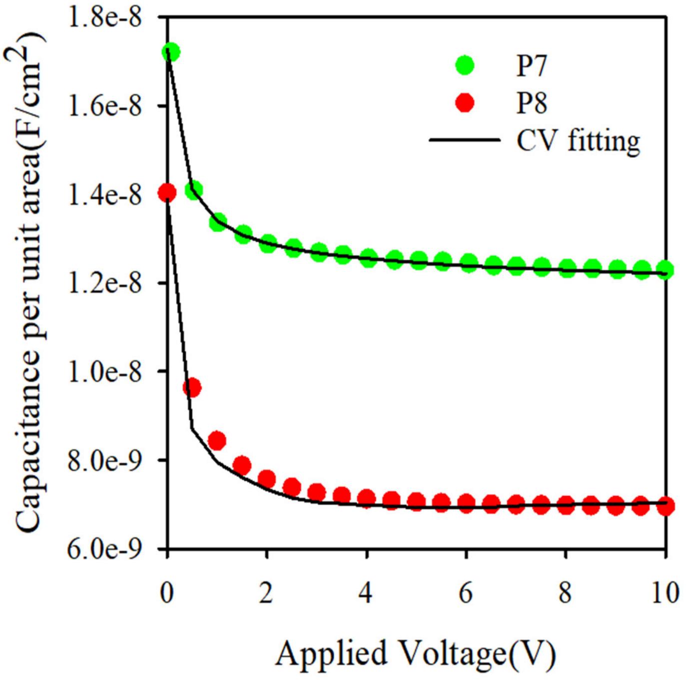

Figure 6.3: CV measurements on P7 and P8. Solid lines are fitting results based on Poisson's equations.

Figure 6.4 shows the spectra of measured EQE on P7 and P8 without anti-reflection coatings, which are 45% and 52.5% respectively at 1550nm. The cut-off (50% of EQE) in GaAsSb is estimated to be 1675nm. Figure 6.5 then shows the absorption coefficient abstracted from EQE measurements. P7 and P8 have a similar value in absorption coefficients, indicating high reproducibility of the growth and similar to those reported previously [12]. Figure 6.5 shows that the absorption between 1400nm and 1700m is slightly higher than the conventional InGaAs absorber [13], which then provides higher responsivity when integrated into a SACM structure. One of the important parameters for absorber material is the tunnelling threshold field which can limit the maximum useful multiplication in the SACM APDs. GaAsSb is assumed to have a similar tunnelling threshold field (about 200 kV/cm) as for an InGaAs absorber in designing our SACM APD because of their similar bandgaps and electron effective masses [14], [15].

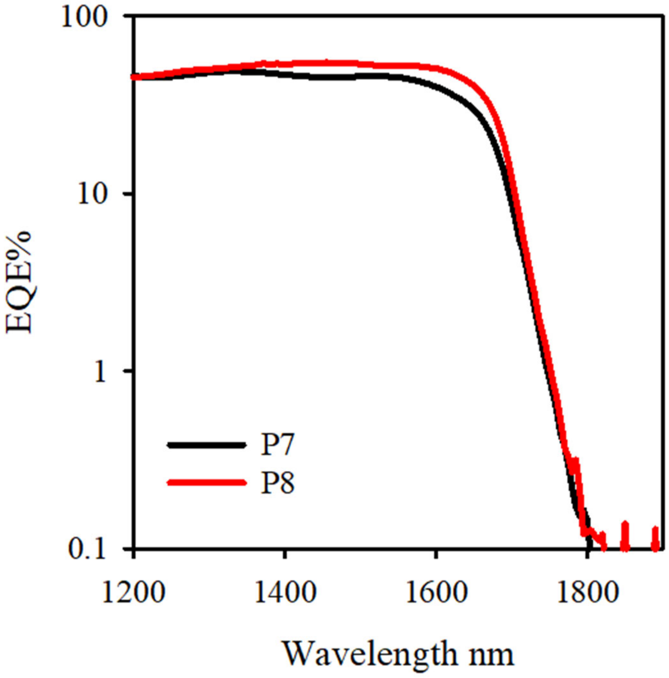

Figure 6.4: External spectral quantum efficiency (without anti-reflection coating) measured on P7 and P8

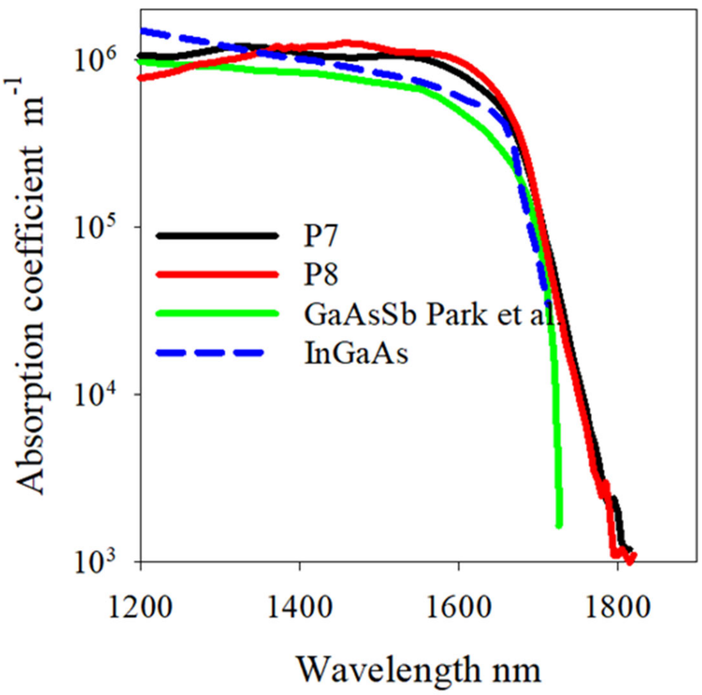

Figure 6.5: Absorption coefficients in GaAsSb in P7 and P8. Green line:GaAsSb reported by Park et al.[12] and Blue dash line InGaAs[13].

6.3.2 Multiplier optimization

The most important part of the SACM structure is the multiplier which determines the performance of the APD. In the previous chapter, the multiplication and excess noise characteristics of different avalanche region thicknesses (P3, P4, P6) are investigated to support determining the desired thickness of the multiplier in the SACM structure. These studies demonstrate the effect of avalanche region thickness on avalanche characteristics and enable the choice of the best thickness for multiplier in the SACM design, maximizing the useful multiplication while reducing the excess noise factor. A summary of the excess noise change with thickness is shown in Figure 6.6 at multiplication 10. It shows about ~1.5 times improvement in excess noise between P3 and P6. The improvements are much more prominent at high multiplication values, as shown in chapter 5. All the measurements were performed using a pure electron injection profile. This ensures that >99% of the light is absorbed in the cladding layer and only electrons travel to the high electric field by diffusion. Chapter 5 shows that as the thickness of the multiplication region increases, the experimental multiplication data approaches that of the theoretical value (β=0), indicating that the thicker the multiplication region, the more closely the device approximates single carrier impact ionization behavior. The excess noise results also suggest that the thickest structure outputs the lowest noise. All these results are in good qualitative agreement with the electric field dependent ionization coefficients extracted in chapter 5. This is because a structure with a thicker multiplication region can operate at a lower electric field, where the α/β ratio is large, giving a lower F. Interestingly, F versus M does not follow McIntyre's local model. This can be explained by previous theoretical work by Ong *et al.*[16] that non-local and dead-space effects can reduce the F in thick avalanche region structures. However, it is undesirable to use thicker avalanche reigons than those employed here, despite the fact that F may continue to decrease as the multiplication region width increases. This is because the operating voltage will become very large in a thicker structure. In addition, the operating speed and C_{bd} will become worse. Therefore, the optimum avalanche multiplier thickness was chosen to be 1000nm (P6), which can provide high multiplication (M=30) at a breakdown voltage of 56V and has a minimal excess noise factor (F=2.2 at M=30). This F value is much smaller than obtainable with an InP or even InAlAs multiplier and is similar to a Si APD [17].

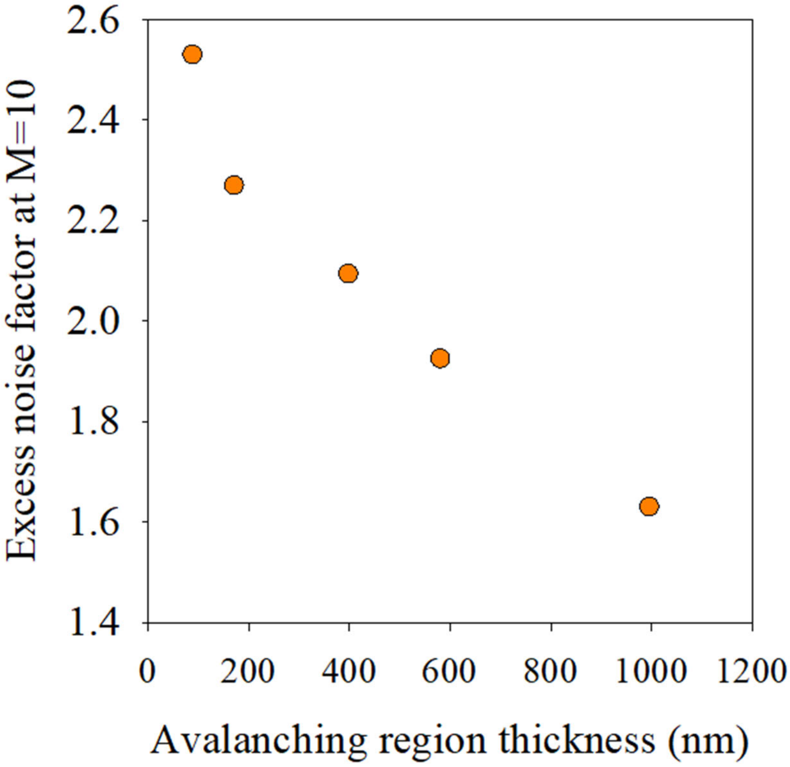

Figure 6.6: Excess noise at M=10 with different avalanching region thickness AlGaAsSb. The structure with 100 and 200nm avalanching regions is taken from the literature[18].

6.3.3 SACM APD characteristics

Several trials were performed on the growth of GaAsSb/AlGaAsSb SACM APDs to optimize the thickness and doping of the grading and charge layers. It was found that a charge layer with 35nm width and a p-type background doping of 6×10^{17} cm^{-3} ensures the electric distribution in the structure, as shown in Figure 6.2.

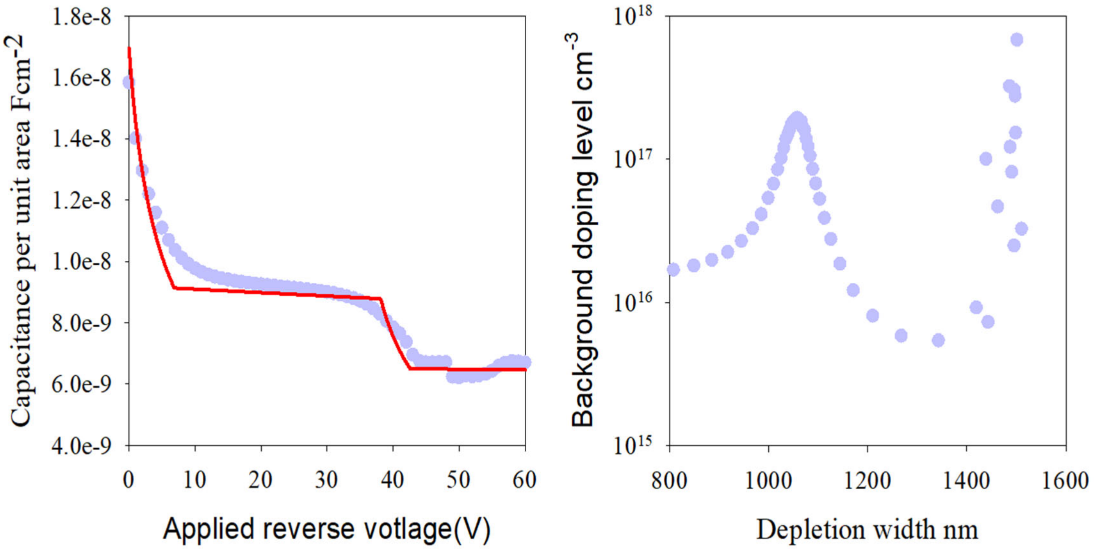

Figure 6.7: Measured C-V results of the SACM APD and doping profile. The solid red line is the C-V fitting result.

Figure 7 shows the C-V of the GaAsSb/AlGaAsSb SACM APD measurements and the doping profile. The red solid line shows the C-V fitting on the measurement data based on Poisson's electric field solver with Matlab. The capacitance gradually decreases with the increase of reverse bias voltage. Then there is a sudden drop at around 42V, indicating the punch-through of the electric field into the absorption layer. C-V modelling based on Poisson's electric field solver precisely shows the doping level and thickness of each section in the structure. The difference is marginal between the actual structure and the designed structure. The thickness of the absorber and multiplication region were found to be 460nm with doping levels of 5×10^{15} cm^{-3} and 1100nm with doping levels of 1×10^{16} cm$^{-3,}$ respectively. The charge sheet is found to be 35nm with 5×10^{17} cm^{-3} *p*-type doping. The doping profile in Figure 6.7 shows that the doping level in the charge sheet is lower than the nominal designed value, likely due to Be dopant diffusion during material growth. However, the total charge under the charge sheet peak is almost identical to the designed value of 2.1×10^{12} cm^{-2}.

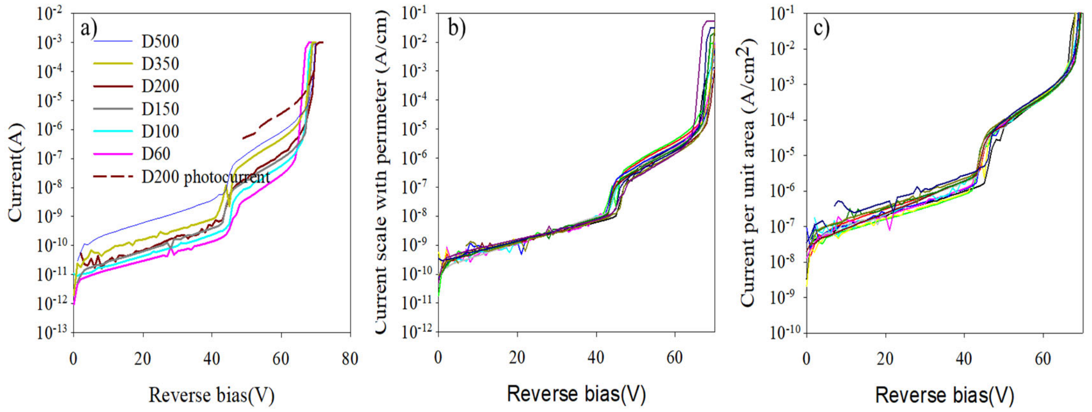

Figure 6.8: **a)** Bias-dependent dark current for different device sizes and photocurrent (I_{ph}) for 200μm diameter device at room temperature **b)** Dark current per unit distance with different devices size **c)** Dark current per unit area with different device size

The dark current of SACM APD with different devices is shown in Figure 6.8. It was found that the dark current scales with perimeter (Fig 8b) before punch-through and scale with area after punch-through (Fig 8c). This indicates that dark current is generated by carriers crossing the charge barrier with generation and recombination mechanisms in small bandgap GaAsSb. Because the generation and recombination process are the variation of the doping concentration or thickness in the charge layer across the wafer can contribute to the small deviation of the punch-through voltage between simulated results and experimental measurements.

The photocurrent (I_{ph}) continues to increase after punch-through due to the avalanche multiplication process until avalanche breakdown (70V). The step around 53V is probably due to the grading layers that impede electron transport. The phenomenon can be mitigated by optimising the bandgap offset with linear grading.

Accurate determination of the multiplication as a function of reverse bias requires knowledge of the gain at a particular bias. Photocurrent below 54V fluctuated, making the value unreliable because carrier may trap at the interface at low electric field. All analyses on the M versus F used data from 54V onward. It is essential to determine the value of multiplication at 54V since the device is fully depleted and the electric field in the multiplication region is high enough to give rise to some multiplication. The electric field profile and impact ionization coefficients obtained previously are used in the random path length (RPL) model to calculate the multiplication of the SACM APD, as shown in Figure 6.9a. This gives a multiplication of 3.6 at 54V, which was used to normalise the photocurrent shown in Figure 6.8a into a bias-dependent multiplication. The modelled multiplication at voltages>54V agrees well with the measured photocurrent results, as shown in Figure 6.9a.

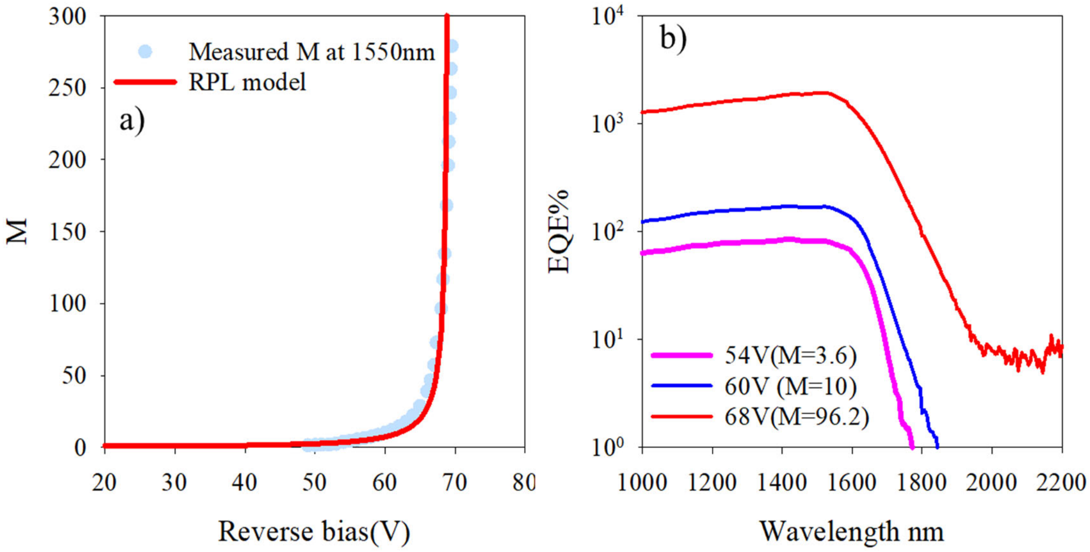

Figure 6.9: a) Multiplication measurements on SACM APD at 1550nm illumination normalized at 54V and the solid red line is RPL model fitting. b) Measured QE spectra of the SACM APD at various reverse bias voltages.

In Figure 6.9, the maximum multiplication measurable is 278, which is about 10 times higher than that of commercial 1500 nm APDs. The measured QE spectra of the SACM APD as a function of wavelength at various reverse biases and hence multiplication values. Comparing the value of the photocurrent at 54V using 1550nm in the SACM APD to those in the P7 and P8 at unity gain further corroborated the *M* value of 3.6. Due to the thin absorber thickness (460nm), the measured QE in the SACM at unity gain is relatively low at 21.35 % but can still achieve 5935.3% (Responsivity of

7418A/W) with the effect of multiplication. The cut-off wavelength is extended to a longer wavelength (~1900nm) as the applied reverse voltage increases because of the Franz-Keldysh effect [19], [20]. This can be helpful for other applications including detection of methane(1650nm), hydrogen chloride(1742nm), nitrogen oxide(1814nm) and water vapor(1845nm, 1877nm)[21].

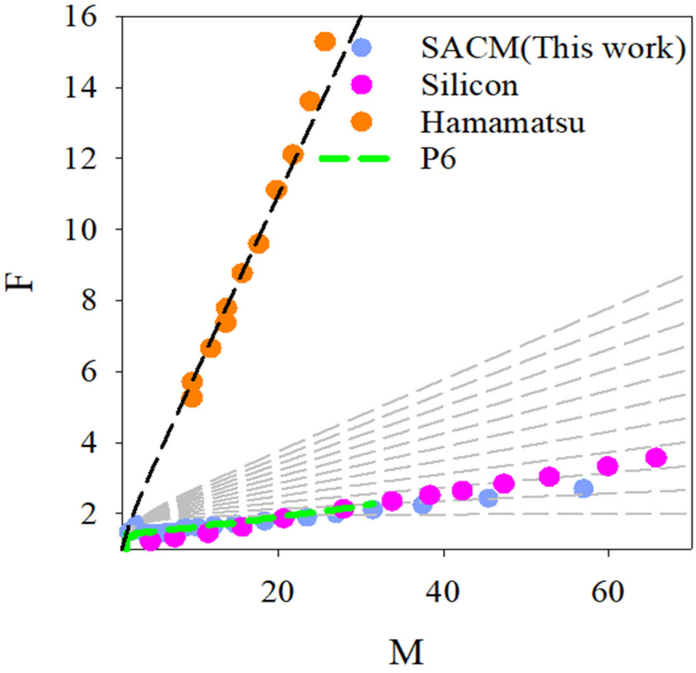

Figure 6.10: Excess noise measurements on SACM compared with commercial Si[22] and Hamamatsu 1550nm APD[5]. Grey dash lines are McIntyre local field lines from k_{eff}=0 to 0.1 in steps of 0.01. The black dash line is McIntyre local field line of k_{eff}=0.5

The measured excess noise of the SACM structure is shown in Figure 6.10. The excess noise is low until the multiplication of 70. It does not follow McIntyre's local theory, and the noise is 10 times lower at M=30 than Hamamatsu 1550nm APDs[5]. In addition, it is encouraging that this device has comparable excess noise characteristics and is even lower than a commercial Si APD [22] for M>25. As discussed previously, the performance of the SACM is mainly dependent on the multiplier region material. The excess noise is very similar to P6. The small difference could be due to the small change in avalanche region thickness.

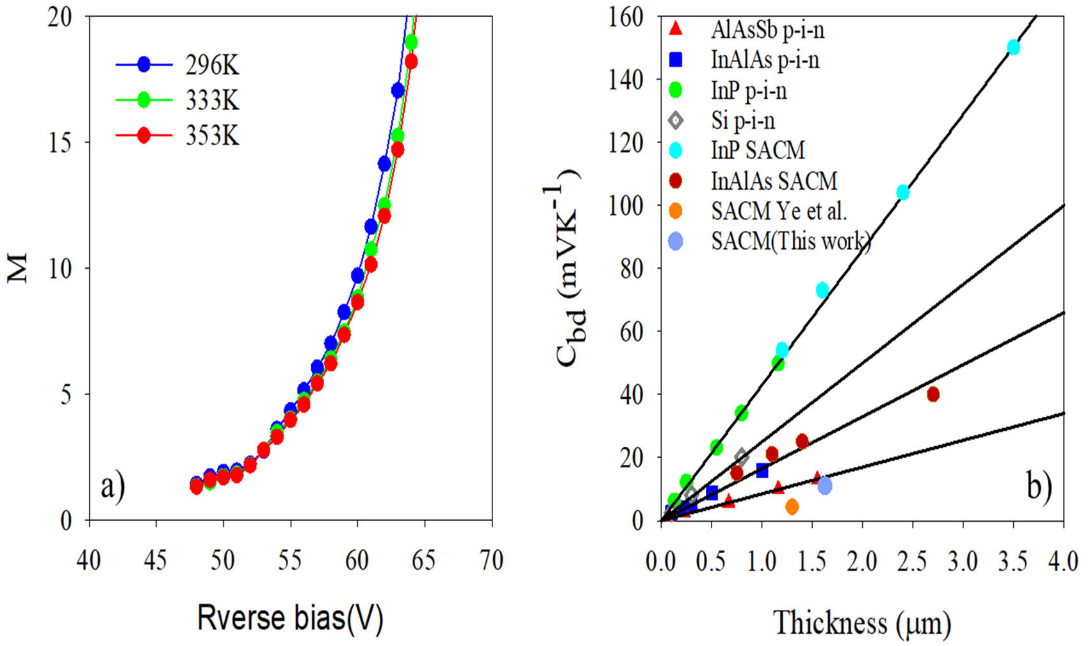

Figure 6.11: a) Temperature dependence multiplication of SACM structure. b) C_{bd} versus total depletion region thickness for different material APDs, InP[23], Si[24], InAlAs[23], AlAsSb[25], [26] and AlGaAsSb[8].

One crucial Figure of merit in APDs is the temperature dependence coefficient of breakdown voltage (C_{bd}) which has been discussed in detail in Chapter 4. It was found that breakdown voltage decreases with temperature decrease. This is because the ionization coeffcients increase with less phonon scattering effects at low temperature. This can then affect the multiplication significantly, hence the sensitivity. Especially for the multiplication region made of materials such as InP[23] and Si[24]. Chapter 4 described details about temerpature dependent meausrments, a similar method was used to measure the C_{bd} in SACM APD. Multiplication at various temperatures 296K,333K and 353K, are shown in Figure 6.11a. The change in voltage with the temperature at M=20 was used rather than at breakdown, as this should give similar results without the risk of catastrophic damage to the devices. The junction temperature is monitored by measuring the forward current as described by Jin et al. [26], and the C_{bd} is ~11.8mV/K, which is 10 times lower than the Hamamatsu device (C_{bd}=100mV/K)[27].

Figure 6.11b compares AlGaAsSb SACM with other materials as a function of total depletion thickness. In this work, the SACM APD shows significantly lower C_{bd} compared to other materials including InP[23], Si[24], InAlAs[23], AlAsSb[26], AlGaAsSb[8]. Ong et al.[28] The alloy disorder potential was responsible for the large differences in the C_{bd} of different semiconductors and the Monte Carlo modelling by Jin et al.[26] showed that the increased alloy scattering relative to the phonon scattering in the Sb-based alloys reduces the temperature dependence of the ionization coefficients, resulting in a much smaller C_{bd}. The advantage of small C_{bd} materials is that they do not need extra temperature stabilization, which makes the device size more compact and potentially eliminates the need for a cooling subsystem.

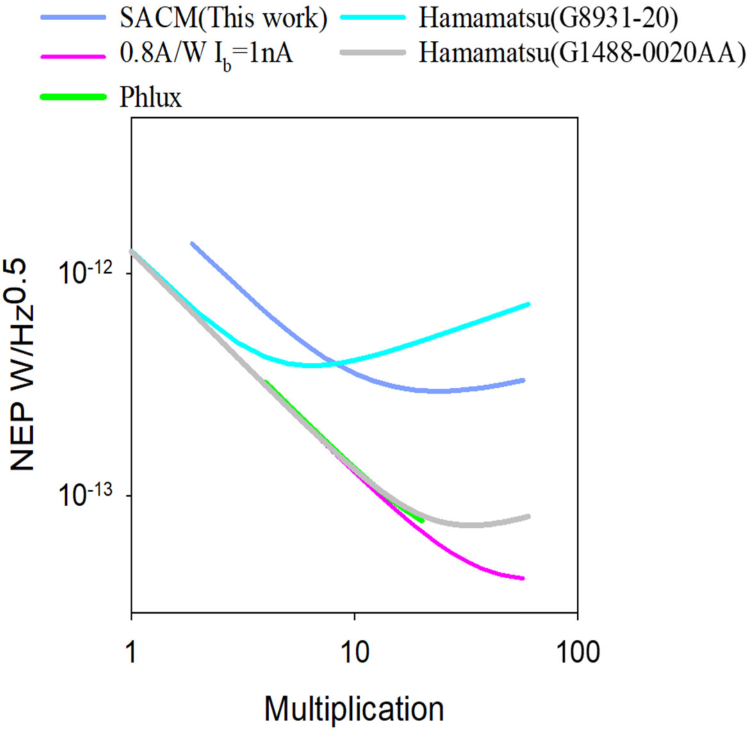

Figure 6.12: Noise-equivalent power (NEP) of SACM APD and other commercial 1550nm APDs. A solid pink line is assumed with SACM APD with 0.8A/W responsivity and 1nA dark current at punch-through. Solid green line:InGaAs/AlGaAsSb 1550nm APD[29].

Noise equivalent power (NEP) is a common parameter to quantify a detector’s sensitivity. NEP is the lowest input power that outputs a signal-to-noise ratio(S/R) of 1 in a 1Hz output bandwidth.

$$NEP = \frac{1}{R}\left(\sqrt{2q(I_{\text{surface}} + I_{bulk}M^2F) + n_{amp}^2}\right) \tag{6.1}$$

Where R is the responsivity and n_{amp} is the noise spectral density of an external amplifier.

For APDs, the NEP expresses the sensitivity of the device and is given in Watt per Hertz[30]. Therefore, it is desirable to have a NEP as low as possible. As shown in equation 6.1, it is important to have a device with low dark current and excess noise but high responsivity to achieve the lowest NEP possible. APDs with low capacitance can reduce the TIA amplifier noise, gain peaking and improve the TIA amplifier stability. The NEP of the SACM APD is compared with other commercially available APDs with different dark currents and excess noise factors (Details can be found in Table 6.2 in a later section). The NEP of this SACM APD (3×10^{-13} A/Hz$^{0.5}$) is higher than a Hamamatsu((G1488-0020AA) APD and an InGaAs/AlGaAsSb SACM APD structure reported by Phlux[31]. This is only due to the unoptimized dark current and thin absorber thickness. However, the excess noise and dark current contribution from the APD becomes the dominant component in the NEP when the multiplication is high. Any further increase in multiplication does not benefit the signal-to-noise ratio. Because of the low excess noise factor observed in this structure, it can extend the useful multiplication range to a higher value. The NEP in this work can be optimized by having a thicker absorber region to increase the responsivity and reduce the dark current by improving the growth quality. The optimized structure NEP is shown as pink line in Figure 6.12. The optimized SACM can reach to a NEP value of 4.3×10^{-14} A/Hz$^{0.5,}$ which is comparable to the best commercial 1550 APD.

6.4 Discussion

Table 6.2: Comparison of this work with the commercial device by Hamamatsu

Parameters	**Excelitas (C30662)**	**Hamamatsu (G8931-20)**	**Hamamatsu (G14858-0020AA)**	**This work (GaAsSb/AlGaAsSb)**
Device diameter	200 µm	200 µm	200 µm	200 µm
Spectral Range	~ 1.7 µm	~ 1.7 µm	~ 1.7 µm	~ 1.7 µm
Capacitance @ Max Depletion	2.5pF	1.5pF	2 pF	2 pF
Breakdown Voltage	50V	55V	65 V	70 V
C_{bd}	140mV/K	110 mV/K	100 mV/K	**11.83** mV/K
Bandwidth	0.85GHz	0.9GHz	**0.9** GHz	0.7 GHz
Max Multiplication	~20	~30	~30	**~278**
Excess noise @ *M* = 25	3.4@*M*=10	~13	~13	**~2**
Dark current @ *M* = 25	4.5nA@*M*=10	2280nA	20nA	480nA

Table 6.2 compares the unoptimized GaAsSb/AlGaAsSb SACM APD with other commercially available 200µm diameter InGaAs APDs to benchmark the device's performance. The most significant advantage of this work is that it can achieve a multiplication of 278, which is much higher than others. The excess noise factor at *M*=25 is about 6.5 times lower than those Hamamatsu ones with similar bandwidth. The C_{bd} is ~10 times lower, which saves extra bulk temperature compensation equipments. Because of the 460nm GaAsSb absorber, the EQE at unity gain is 21.35% which is lower than the Hamamatsu InGaAs APD. The only limiting factor is the dark

current in this SACM structure. It is ~24 times higher than Hamamatsu(G14858-0020AA) but still better than the old model(G8931-20). Due to the lack of data regarding the Excelitas device, no fair comparison can be made at *M*=10, but this work shows advantages in most of the metrics. This work can be optimized by increasing the absorber thickness to 2μm and using an AR coating. The performance of this SACM APD can be improved dramatically. EQE can reach to 87% at unity gain and potentially a maximum multiplied EQE of 24186%. However, C_{bd} will increase to ~24 mV/K if the total thickness is doubled, but it will still be much lower compared to these commercial InGaAs APDs.

In the recent years, Sb containing materials demonstrate low excess noise and large *α/β* ratio on InP substrate, for example, AlGaAsSb[32][33], AlAsSb[34][35] and AlInAsSb[33]. Their noise is smaller than those P- and As-bearing materials with some subMcintyre behaviours. All of these suggest that the impact ionization process may

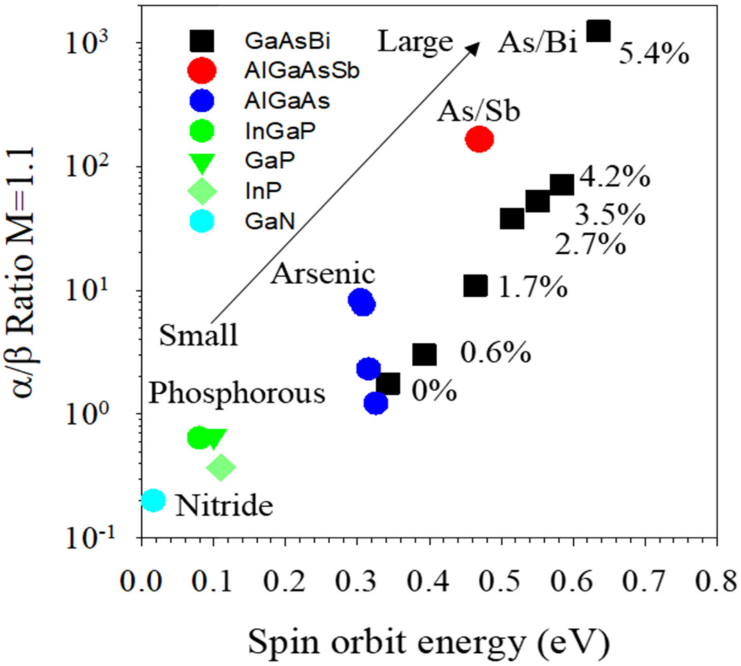

Figure 6.13:*α/β* ratio at M=1.1 versus spin orbit energy for various material including GaN[36][37], GaP[38][39], InGaP[40][41], InP[26][42], AlGaAs[43][44][45] and GaAsBi[46]. The spin orbit energy of AlGaAsSb was theoretically calculated using a 14 bands *k*p* method.

be different in large group V atoms (Sb, Bi) compared to small atoms like P and As. Oguzman et al. showed that the hole ionization process was largely initiated from the split-off band in GaAs [47]. An increase of spin orbit split($\triangle so$) makes it more difficult for holes to transfer from the heavy and light hole bands into the split-off band. Hence the hole ionization is much reduced. This has been demonstrated by Liu et al. in the GaAsBi system [46]. Since excess noise is primarily dependent on the α/β ratio, Figure 6.13 shows various material system α/β ratios (at the electric fields corresponding to M=1.1 in 1µm p-i-n diodes) as a function of $\triangle so$. It is clear that the α/β ratio decreases with the decrease of $\triangle so$. This is related to the size of the group V atoms in the alloys (N, P, As, As/Sb,As/Bi). The $\triangle so$ can reach up to 0.6eV, resulting in a larger α/β ratio with only 5.4% incorporation of Bi. The electron ionization coefficients in InP, InAlAs and AlAsSb are very similar, but the hole ionization coefficients decrease with increasing $\triangle so$. Similarly, in GaAsBi, α changes slightly whereas β decreases significantly with increasing Bi incorporation [48]. Engineering the valence band can be an effective way to alter the hole ionization coefficient, and therefore the α/β ratio, and reduce excess noise.

6.5 Conclusion

In summary, this work demonstrated the optical properties of GaAsSb and was found to be very similar to InGaAs in absorption coefficient and cut-off. It shows the feasibility of using GaAsSb as an absorber in the SACM design. This work demonstrates a high gain, extremely low excess noise SACM APD with GaAsSb/AlGaAsSb on InP comparable to Si and other commercially available InGaAs APDs for 1550nm detection. This work can be further improved by reducing the bulk dark current and increasing the absorber’s thickness to reduce the NEP. These characteristics will provide significant performance enhancements in Lidar systems and other applications requiring high sensitivity and fast response time APDs.

Because of the spin-orbit splitting energy, Sb-containing materials show very low excess noise and a large *α/β* ratio. Engineering the valence band can be used to alter the $\triangle so$ and reduce the excess noise.

6.8 References

[1] U. N. Singh *et al.*, "Feasibility study of a space-based high pulse energy 2 \$µ\$m CO2 IPDA lidar," *Appl. Opt.*, vol. 56, no. 23, pp. 6531–6547, Aug. 2017, doi: 10.1364/AO.56.006531.

[2] Paul F. McManamon, *LiDAR Technologies and Systems*. SPIE, 2019.

[3] C. A. Gueymard, "Parameterized transmittance model for direct beam and circumsolar spectral irradiance," *Sol. Energy*, vol. 71, no. 5, pp. 325–346, 2001, doi: https://doi.org/10.1016/S0038-092X(01)00054-8.

[4] D. Chu, S. Aboujja, and D. Bean, "1550nm Triple Junction Laser Diode Outshines 905nm in Automotive LiDAR Eye safe level of 905nm and 1550nm," pp. 1–7.

[5] Hamamatsu, "High Speed InGaAs APD," Ichino-cho, 2019.

[6] P. Yuan *et al.*, "Impact ionization characteristics of III-V semiconductors for a wide range of multiplication region thicknesses," *IEEE J. Quantum Electron.*, vol. 36, no. 2, pp. 198–204, 2000, doi: 10.1109/3.823466.

[7] K.-S. Hyun and C.-Y. Park, "Breakdown characteristics in InP/InGaAs avalanche photodiode with p-i-n multiplication layer structure," *J. Appl. Phys.*, vol. 81, no. 2, pp. 974–984, Jan. 1997, doi: 10.1063/1.364225.

[8] Y. Cao, T. Osman, E. Clarke, P. K. Patil, J. S. Ng, and C. H. Tan, "A GaAsSb/AlGaAsSb Avalanche Photodiode with a very small Temperature Coefficient of Breakdown Voltage," *J. Light. Technol.*, vol. PP, no. c, p. 1, 2022, doi: 10.1109/JLT.2022.3167268.

[9] S. Xie *et al.*, "InGaAs/AlGaAsSb avalanche photodiode with high gain-bandwidth product," *Opt. Express*, vol. 24, no. 21, p. 24242, 2016, doi: 10.1364/oe.24.024242.

[10] Y. Xiao, Z. Li, and Z. S. Li, "Modeling of InGaAs/AlGaAsSb APDs with high gain-bandwidth product," in *Proc.SPIE*, Aug. 2020, vol. 11498, p. 114980R, doi: 10.1117/12.2568197.

[11] Silvaco Inc., “Atlas User’s Manual,” 2016. [Online]. Available: https://dynamic.silvaco.com/dynamicweb/jsp/downloads/DownloadManualsAction.do?req=silen-manuals&nm=atlas.

[12] M.-S. Park and J. H. Jang, “GaAs0.5Sb0.5 lattice matched to InP for 1.55 µm photo-detection,” *Electron. Lett.*, vol. 44, pp. 549–551, 2008, doi: 10.1049/el:20083433.

[13] D. Hahn, O. Jaschinski, H.-H. Wehmann, A. Schlachetzki, and M. Von Ortenberg, “Electron-concentration dependence of absorption and refraction in n-In0.53Ga0.47As near the band-edge,” *J. Electron. Mater.*, vol. 24, no. 10, pp. 1357–1361, 1995, doi: 10.1007/BF02655448.

[14] I. Vurgaftman, J. R. Meyer, and L. R. Ram-Mohan, “Band parameters for III-V compound semiconductors and their alloys,” *J. Appl. Phys.*, vol. 89, no. 11 I, pp. 5815–5875, 2001, doi: 10.1063/1.1368156.

[15] P. Devlin, H. M. Heravi, and J. C. Woolley, “Electron effective mass values in GaAsxSb1−x alloys,” *Can. J. Phys.*, vol. 59, no. 7, pp. 939–944, 1981, doi: 10.1139/p81-123.

[16] D. S. Ong, A. H. Tan, K. Y. Choo, K. H. Yeoh, and J. P. R. David, “Weibull-Fréchet random path length model for avalanche gain and noise in photodiodes,” vol. 55, no. 6, p. 65105, Nov. 2021, doi: 10.1088/1361-6463/ac31f0.

[17] HAMAMATSU, “High-sensitivity Si APD for detection of light with a wavelength of 266 nm,” Ichino-cho, 2018. [Online]. Available: http://hamamatsu.com/resources/products/ssd/pdf/tech/si_apd_technical_information.pdf.

[18] L. L. G. Pinel *et al.*, “ Effects of carrier injection profile on low noise thin Al 085 Ga 015 As 056 Sb 044 avalanche photodiodes ,” *Opt. Express*, vol. 26, no. 3, p. 3568, 2018, doi: 10.1364/oe.26.003568.

[19] M. J. Sun, K. H. Nichols, W. S. C. Chang, R. O. Gregory, F. J. Rosenbaum, and C. M. Wolfe, “Gallium arsenide electroabsorption avalanche photodiode waveguide detectors,” *Appl. Opt.*, vol. 17, no. 10, pp. 1568–1578, May 1978, doi: 10.1364/AO.17.001568.

[20] T. E. Van Eck, L. M. Walpita, W. S. C. Chang, and H. H. Wieder, “Franz–Keldysh electrorefraction and electroabsorption in bulk InP and GaAs,” *Appl. Phys. Lett.*, vol. 48, no. 7, pp. 451–453, Feb. 1986, doi: 10.1063/1.96527.

[21] Z. Li, “Quantitative Hydrogen Chloride Detection in Combustion Environments Using Tunable Diode Laser Absorption Spectroscopy with,” vol. 76, no. 2, pp. 207–215, 2022, doi: 10.1177/00037028211060866.

[22] Hamamatsu, “Si APD S10341,” 2018. [Online]. Available: https://www.hamamatsu.com/content/dam/hamamatsu-photonics/sites/documents/99_SALES_LIBRARY/ssd/s10341_series_kapd1030e.pdf.

[23] L. J. J. Tan *et al.*, “Temperature dependence of avalanche breakdown in InP and InAlAs,” *IEEE J. Quantum Electron.*, vol. 46, no. 8, pp. 1153–1157, 2010, doi: 10.1109/JQE.2010.2044370.

[24] D. J. Massey, J. P. R. David, and G. J. Rees, “Temperature dependence of impact ionization in submicrometer silicon devices,” *IEEE Trans. Electron Devices*, vol. 53, no. 9, pp. 2328–2334, 2006, doi: 10.1109/TED.2006.881010.

[25] S. Xie and C. H. Tan, “AlAsSb avalanche photodiodes with a Sub-mV/K temperature coefficient of breakdown voltage,” *IEEE J. Quantum Electron.*, vol. 47, no. 11, pp. 1391–1395, 2011, doi: 10.1109/JQE.2011.2165051.

[26] X. Jin *et al.*, “Temperature Dependence of the Impact Ionization Coefficients in AlAsSb Lattice Matched to InP,” *IEEE J. Sel. Top. Quantum Electron.*, vol. 28, no. 2, 2022, doi: 10.1109/JSTQE.2021.3099912.

[27] Hamamatsu, “InGaAs APD,” 2010.

[28] J. S. L. Ong, J. S. Ng, A. B. Krysa, and J. P. R. David, “Temperature dependence of avalanche multiplication and breakdown voltage in Al0.52In0.48P,” *J. Appl. Phys.*, vol. 115, no. 6, pp. 0–6, 2014, doi: 10.1063/1.4865743.

[29] X. Collins *et al.*, “Low-noise AlGaAsSb avalanche photodiodes for 1550nm light detection,” vol. 1199709, no. March, p. 16, 2022, doi: 10.1117/12.2608842.

[30] C. M. O’Sullivan and J. A. Murphy, “Noise Equivalent Power,” *F. Guid. to Terahertz Sources, Detect. Opt.*, pp. 30–30, 2012, doi: 10.1117/3.952851.ch27.

[31] X. Collins *et al.*, “Low-noise AlGaAsSb avalanche photodiodes for 1550nm light detection,” vol. 1199709, no. May, p. 16, 2022, doi: 10.1117/12.2608842.

[32] S. Lee *et al.*, “Low noise Al0.85Ga0.15As0.56Sb0.44avalanche photodiodes on InP substrates,” *Appl. Phys. Lett.*, vol. 118, no. 8, pp. 0–5, 2021, doi: 10.1063/5.0035571.

[33] B. Guo *et al.*, “Impact Ionization Coefficients of Digital Alloy and Random Alloy Al0.85Ga0.15As0.56Sb0.44 in a Wide Electric Field Range,” *J. Light. Technol.*, vol. 40, no. 14, pp. 4758–4764, 2022, [Online]. Available: http://opg.optica.org/jlt/abstract.cfm?URI=jlt-40-14-4758.

[34] X. Yi *et al.*, “Extremely low excess noise and high sensitivity AlAs0.56Sb0.44 avalanche photodiodes,” *Nat. Photonics*, vol. 13, no. 10, pp. 683–686, 2019, doi: 10.1038/s41566-019-0477-4.

[35] X. Yi *et al.*, “Demonstration of large ionization coefficient ratio in AlAs0.56Sb0.44 lattice matched to InP,” *Sci. Rep.*, vol. 8, no. 1, pp. 8–13, 2018, doi: 10.1038/s41598-018-27507-w.

[36] L. Cao *et al.*, “Experimental characterization of impact ionization coefficients for electrons and holes in GaN grown on bulk GaN substrates,” *Appl. Phys. Lett.*, vol. 112, no. 26, p. 262103, Jun. 2018, doi: 10.1063/1.5031785.

[37] A. Wolos *et al.*, “Electron spin resonance and Rashba field in GaN-based materials,” *Phys. B Condens. Matter*, vol. 406, no. 13, pp. 2548–2554, 2011, doi: https://doi.org/10.1016/j.physb.2011.03.060.

[38] R. A. Logan and A. G. Chynoweth, “Charge Multiplication in GaP p-n Junctions,” *J. Appl. Phys.*, vol. 33, no. 5, pp. 1649–1654, May 1962, doi: 10.1063/1.1728804.

[39] S. E. Stokowski and D. D. Sell, “Reflectivity and $\frac{(\frac{\mathrm{dR}}{\mathrm{dE}})}{R}$ of GaP between 2.5 and 6.0 eV,” *Phys. Rev. B*, vol. 5, no. 4, pp. 1636–1639, Feb. 1972, doi: 10.1103/PhysRevB.5.1636.

[40] C. H. Tan, R. Ghin, J. P. R. David, G. J. Rees, and M. Hopkinson, “The effect of dead space on gain and excess noise in In0.48Ga0.52P p+in+ diodes,” *Semicond. Sci. Technol.*, vol. 18, no. 8, pp. 803–806, 2003, doi: 10.1088/0268-1242/18/8/314.

[41] R. G. Alonso, A. Mascarenhas, S. Froyen, G. S. Horner, K. Bertness, and J. M. Olson, “Polarized piezomodulated reflectance study of spontaneous ordering in GaInP2,” *Solid State*

Commun., vol. 85, no. 12, pp. 1021–1024, 1993, doi: https://doi.org/10.1016/0038-1098(93)90158-J.

[42] J. Peretti, H.-J. Drouhin, D. Paget, and A. Mircéa, “Band structure of indium phosphide from near-band-gap photoemission,” *Phys. Rev. B*, vol. 44, no. 15, pp. 7999–8008, Oct. 1991, doi: 10.1103/PhysRevB.44.7999.

[43] M. E. Levinshtein and S. L. Rumyantsev, “SILICON (<inline-formula><roman>Si</roman></inline-formula>),” in *Handbook Series on Semiconductor Parameters*, WORLD SCIENTIFIC, 1996, pp. 1–32.

[44] S. Sheffield, “Ionization coefficients in Al x Ga 1 − x As (x = 0 – 0 . 60),” vol. 15, pp. 692–699, 2000.

[45] B. K. Ng *et al.*, “Avalanche multiplication characteristics of Al/sub 0.8/Ga/sub 0.2/As diodes,” *IEEE Trans. Electron Devices*, vol. 48, no. 10, pp. 2198–2204, 2001, doi: 10.1109/16.954454.

[46] Y. Liu *et al.*, “Valence band engineering of GaAsBi for low noise avalanche photodiodes,” *Nat. Commun.*, vol. 12, no. 1, 2021, doi: 10.1038/s41467-021-24966-0.

[47] İ. H. Oğuzman, Y. Wang, J. Kolník, and K. F. Brennan, “Theoretical study of hole initiated impact ionization in bulk silicon and GaAs using a wave-vector-dependent numerical transition rate formulation within an ensemble Monte Carlo calculation,” *J. Appl. Phys.*, vol. 77, no. 1, pp. 225–232, Jan. 1995, doi: 10.1063/1.359374.

[48] K. Alberi, O. D. Dubon, W. Walukiewicz, K. M. Yu, K. Bertulis, and A. Krotkus, “Valence band anticrossing in GaBixAs1−x,” *Appl. Phys. Lett.*, vol. 91, no. 5, p. 51909, Jul. 2007, doi: 10.1063/1.2768312.

Chapter 7

Conclusion and further plans

7.1 Conclusions

In this thesis, temperature dependence characteristics were studied. The avalanche multiplication measurements were performed on both p-i-n and n-i-p structures. The breakdown voltage can be not determined accurately on materials with large α/β ratio. Instead, a numerical model (RPL) is used with temperature dependence ionization coefficients to estimate the breakdown voltage hence the C_{bd}. It was found that both α and β are decreasing with similar rate from 210K to 335K as the temperature increase. The multiplication is less sensitive with temperature at high electric field compared to low electric field due to the carrier transportation process. AlAsSb shows its unique advantage in low C_{bd} value compared to other conventional APD materials such as InAlAs and InP. This is favorable since it can avoid using bulk equipment to stabilize the temperature. AlAsSb exhibits small variation in multiplication with temperature because its large alloy disorder potential. And in addition, MC model suggest that the large alloy scattering process is also responsible for the temperature insensitive characteristic. New Figure of merit *P*, which was defined as the temperature dependence coefficient, a material parameter to describe C_{bd} change with total avalanche region width. This can provide more straight forward comparison between material on their temperature dependence characteristic.

The avalanche multiplication in AlGaAsSb is investigated using a series of p-i-n and n-i-p structures with nominal *i*-region thickness from 87nm to 1020nm. It shows the reduction in surface leakage dark current compared to AlAsSb while maintaining large α/β ratio. The local ionization coefficients are extracted from the multiplication measurements. RPL model simulated multiplication with extracted ionization coefficients can agree well with the measured multiplication over three orders of magnitude down to 0.01 while dead space effect or history of the carrier are not taken into consideration. The α and β are found to converge at high electric field but show reasonable large α/β ratio at low electric field. Excess noise measurements were performed on a series of p-i-n and n-i-p structures with different thickness. AlGaAsSb demonstrate the submcintyre behavior and extreme low excess noise (k_{eff}=0 at M=30) which is comparable with Silicon. Both multiplication measurements and excess noise measurements shows that $\alpha >> \beta$ in AlGaAsSb. The presence of Sb atoms pushes down the split-off band in the alloy band structure deeper into the valance band, suppress the hole ionization, hence reduce the excess noise. The avalanching region thickness are optimized for different applications. Since the AlGaAsSb dark current is reduced by a order of magnitude and also have low excess noise, it makes this material a good candidate for SACM structure that used in telecommunication and lidar.

For the first time, GaAsSb/AlGaAsSb on InP is demonstrated that can achieve high multiplication(M=278), high sensitivity, extremely low excess noise and low temperature dependence (C_{bd}=11.87mV/K). The optical properties of GaAsSb were found to have similar absorption coefficients and cut-off as InGaAs. Despite the thin absorber thickness make the unity gain EQE low compared to other commercially available InGaAs APD, it is still outperformed in other metrics. The advantage of this SACM APD comes from the low excess noise multiplier and that is due to the $\triangle_{so}$ presented in this alloy system.

7.2 Further plans

There is considerably more scope for further research on this topic that a new PhD student could undertake. These can be broken down to work undertaken on existing devices and samples, and new growth of novel structures. With the **existing** series of AlGaAsSb p-i-n diodes and the SACM-APD structures, we can undertake a series of further experiments, assuming that the material and devices have not degraded significantly.

In chapter 4, temperature dependence of the p-i-n diodes has only been undertaken over a limited temperature range due to the limitations of the Janis probe station. By packaging the devices onto a TO5 header, we can mount them in a closed cycle cryostat and take the temperature down to 12K. The dark currents should be reduced significantly, and the onset of the avalanche multiplication can be determined more accurately at lower electric fields. We can also confirm that the C_{bd} that was measured at higher temperatures also hold true across a wider temperature range.

Reverse bias measurements on the SACM-APD with 1450nm light can be used to determine the conduction band offsets between the absorber region and the multiplication regions accurately. This needs to be done over a temperature range of 12K – 400K and the activation energy determined. We can undertake wavelength dependent photocurrent measurements to determine how the absorption coefficient of the GaAsSb changes with temperature and with bias. This will also tell us how the bandgap changes with temperature and how well it follows the Varshni expression. By undertaking avalanche multiplication measurements in a closed cycle cryostat, we can extract the C_{bd} of the SACM-APD over a wider temperature range. We also have a number of SACM-APD structures that did not work well at RT due to their charge sheet or grading layer designs being slightly wrong. These may show better performance at lower or higher temperatures.

We can investigate the performance of the SAM-APD at low temperatures. The dark currents should be reduced significantly and this will enable us to determine the minimum number of photons we can detect at high gain in linear mode. The extremely low excess noise of the AlGaAsSb system should allow us to see if these APDs can work like CMT for single or few photon detection at high gains.

With **new devices** of AlGaAsSb p-i-n diodes and SACM-APD structures, there are a wide variety of experiments we can do. By having a series of different Al:Ga compositions in p-i-n and n-i-p configurations, we can map out how the band-gap changes from a direct to indirect bandgap alloy. We can also see if the large α/β ratio is maintained at lower Al compositions, and how the tunnelling dark currents will change as we go from an indirect to direct bandgap alloy. Comparing these parameters with those of other Al:Ga alloys such as AlGaAs and AlGaInP will give us some insight into how the band structure affects the impact ionization properties. We can also design SACM-APD structures with a more optimised excess noise property and also ensure that the grading layers are chosen to minimise the effects of carrier trapping. An optimised SACM-APD should enable us to achieve a much higher multiplication with lower excess noise, raising the possibility of a linear mode APD that is capable of detecting a few (or single) photons. Such an APD could be demonstrated in a system for LiDAR applications or for free space optical communications. We can compare the performance of a ranging system using a commercial InGaAs based APD with one of our AlGaAsSb based APDs, and thereby quantify how the performance will improve if we could operate with a higher avalanche gain.

With **new p-i-n and n-i-p layer** structures with different Al:Ga compositions, we can also look at how the dark currents can be kept low by undertaking etching experiments using different wet and dry etching recipes. Reducing the surface leakage component can also be attempted by using different techniques for passivating the etched surface, say for example by using BCB or SU8. Oxidisation of the Al:Ga surface is likely to be a problem in any mesa devices. Understanding how sensitive the different Al:Ga compositions are to this process would also be useful.

The performance of the devices shown in Chapter 6 can be further improved by changing the structure. It is useful to redesign this structure with thicker multiplication region to ensure at least 0.8A/W responsivity at unity gain. At the same time, the dark current is actually an important factor that can degrade the signal to noise ratio. Currently, the dark current is about 20 times higher than Hamamatsu devices. It requires some efforts to reduce the bulk dark current by improving the growth quality. It is important to demonstrate the benefits of using this device on system levels and compare the enhancement when it integrated into a receiver module. At the moment, there only InGaAs/InP planar structure have developed[1]. The next step is to develop the planar structure since it provides higher reliability than the mesa structure. And see the possibility for this structure to work as Single photon detector (SPAD) and compare the performance with InGaAs/InP.

There is also growing interest in gas detection that requires long wavelength detectors. For example, methane(1650nm), nitrogen oxide(1814nm) and water vapor (1877nm) [2]. These are the wavelengths that InGaAs or GaAsSb is not capable to detect. Type-II super lattice can be a potential good absorber for further SACM configuration to cover up to 4µm. InGaAs/GaAsSb type II superlattices (T2SL) can be grown on InP substrate using conventional III-V growth technique. The cut-off wavelength can be engineered by tailoring the superlattice well (InGaAs) and barrier(GaAsSb) thicknesses and compositions. Since the AlGaAsSb already demonstrated its low noise characteristics, type II/AlGaAsSb can be used for gas detection with proper design of charge sheet and grading layers.

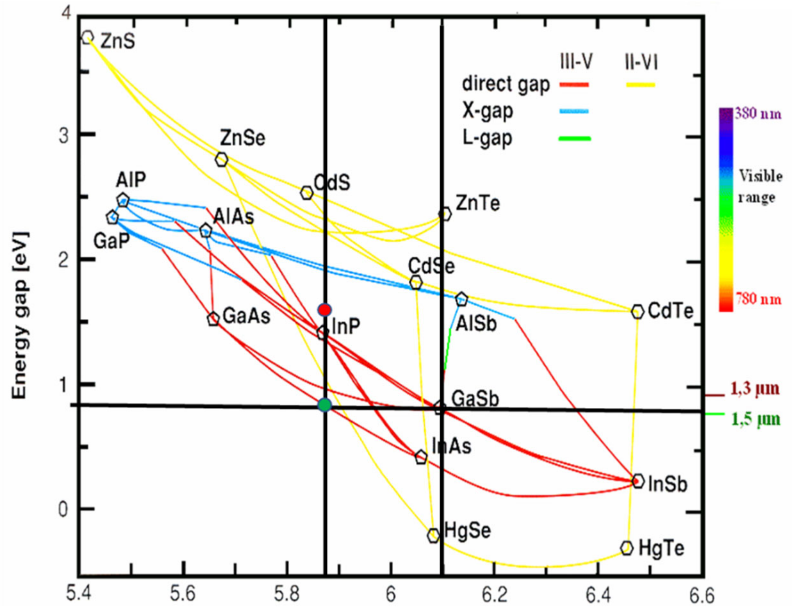

Figure 7.1: Lattice match diagram for different materials[3].

As an alternative to AlGaAsSb on InP, AlInAsSb can also grow on InP as shown in Figure 7.1. Recently, Jones et al.[4] has demonstrated the AlInAsSb SACM structure that can detect up to 2µm on GaSb substrate. However, the doped substrate reduces the bandwidth because of the capacitance and high cost GaSb susbtrate make this configuration commercially unfeasible. Kodati et al. [5] shows AlInAsSb grown InP also have low excess noise characteristics, it is interesting to investigate the optical properties and multiplication region properties of AlInAsSb on InP. And fully characterize this alloy system in term of QE, avalanche multiplication, excess noise, speed, and temperature dependence.

7.3 References

[1] M. A. Itzler, C. S. Wang, S. McCoy, N. Codd, and N. Komaba, “Planar bulk InP avalanche photodiode design for 2.5 and 10 Gb/s applications,” in *24th European Conference on Optical Communication. ECOC ’98 (IEEE Cat. No.98TH8398)*, 1998, vol. 1, pp. 59–60 vol.1, doi:

10.1109/ECOC.1998.732435.

[2] Z. Li, “Quantitative Hydrogen Chloride Detection in Combustion Environments Using Tunable Diode Laser Absorption Spectroscopy with,” vol. 76, no. 2, pp. 207–215, 2022, doi: 10.1177/00037028211060866.

[3] G. Brill, “New Material System for 3rd Generation IR Applications New Material System for 3 rd Generation IR Applications by Gregory Brill and Yuanping Chen,” no. May, 2014.

[4] A. H. Jones, Y. Yuan, M. Ren, S. J. Maddox, S. R. Bank, and J. C. Campbell, “Al_xIn_1-xAs_ySb_1-y photodiodes with low avalanche breakdown temperature dependence,” *Opt. Express*, vol. 25, no. 20, p. 24340, 2017, doi: 10.1364/oe.25.024340.

[5] S. H. Kodati *et al.*, “AlInAsSb avalanche photodiodes on InP substrates,” *Appl. Phys. Lett.*, vol. 118, no. 9, p. 91101, Mar. 2021, doi: 10.1063/5.0039399.

Appendix A

Capacitance-voltage modelling

In this section, it derives the expression for simulating the CV profile in a p-i-n structure within a depletion approximation. Figure 1 shows a p-i-n structure with an i-region width of *w*. It assumes that the p-n junction is abrupt and the doping level in each layer is uniform with values of N_p, N_i and N_n for the p, i and n regions respectively. The electric field gradient in each region expressed as follows according to Poisson's equation[1]:

$$G_p = \left.\frac{d\xi}{dx}\right|_p = \frac{qN_p}{\varepsilon} \tag{B.1}$$

$$G_i = \left.\frac{d\xi}{dx}\right|_i = \frac{qN_i}{\varepsilon} \tag{B.2}$$

$$G_n = \left.\frac{d\xi}{dx}\right|_n = \frac{qN_n}{\varepsilon} \tag{B.3}$$

Where ξ is the electric field, q is the elementary electronic charge and ε is the permittivity of the semiconductor.

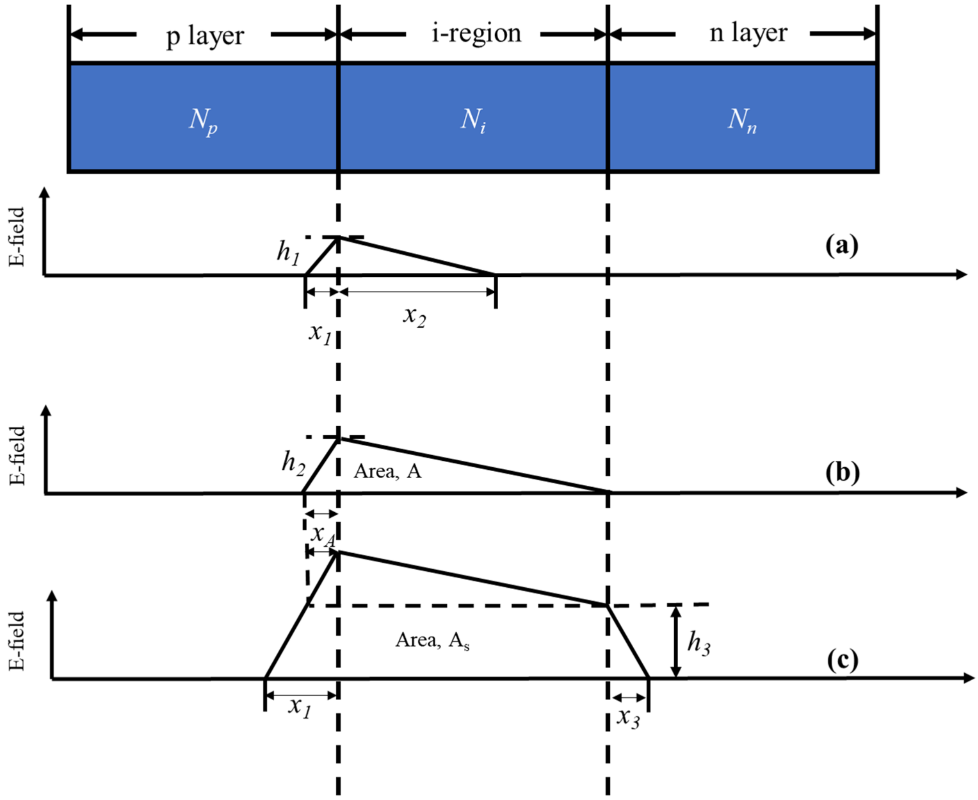

Figure B.1: A schematic diagram of a p-i-n diode and electric field profile under reverse biased condition.

As shown in Figure B.1, the i-region can either be partially depleted(a), just depleted(b) and fully depleted with the electric field depletion in the n region(c). The area under the electric field profile for which the i-region is depleted is given as following:

$$A = 0.5H_2(x_A + w) \tag{B.4}$$

$$H_2 = w\left.\frac{d\xi}{dx}\right|_i = wG_i \tag{B.5}$$

$$x_A = \frac{H_2}{G_p} \tag{B.6}$$

By substituting equation B.5 and B.6 into B.4, the expression become

$$A = 0.5wG_i\left(w\frac{G_i}{G_p} + w\right) = 0.5w^2G_i\left(\frac{G_i}{G_p} + 1\right) \text{ and } x_A = w\frac{G_i}{G_p} \tag{B.7}$$

The total reverse bias voltage V_t is the sum of applied reverse bias voltage (V_r) and built in voltage V_{Bi}, therefore $V_t = V_r + V_{Bi}$.

Case 1: $V_t < A$, the i-region is either partially depleted (or just) depleted and the total depletion width is given by

$$w_t = x_1 + x_2 \tag{B.8}$$

As shown in Figure B.1.and B.1.b, in this case,

$$H_1 = x_1G_p = x_2G_i \tag{B.9}$$

$$V_t = 0.5H_1(x_1 + x_2) \tag{B.10}$$

By using equation B.9 and B.10, solving for x_1 and x_2,

$$x_1 = \sqrt{\frac{2V_t}{G_p\left(1+\frac{G_p}{G_i}\right)}} \text{ and } x_2 = x_1\frac{G_p}{G_i} \tag{B.11}$$

Case 2: $V_t < A$, as shown in Figure B.1.c, the area is given by

$$A_s = V_T - A = 0.5H_3(2w + x_1 + x_3 + x_A) \tag{B.12}$$

$$x_1 = \frac{H_3}{G_p} + x_A \tag{B.13}$$

$$x_3 = \frac{H_3}{G_n} \tag{B.14}$$

By substituting equation B.13 and B.14 into equation B.12,

$$0.5\left(\frac{1}{G_p}+\frac{1}{G_n}\right)H_3^2+(w+x_A)H_3+(A-V_T)=0 \qquad \text{(B.15)}$$

Since H3 is always positive, the solution for this quadratic equation is simply.

$$H_3=\frac{-(w+x_A)+\sqrt{(w+x_A)^2+2\left(\frac{1}{G_p}+\frac{1}{G_n}\right)(V_T-A)}}{\left(\frac{1}{G_p}+\frac{1}{G_n}\right)} \qquad \text{(B.16)}$$

And the total depletion width is

$$w_{\mathrm{T}}=w+x_A+H_3\left(\frac{1}{G_p}+\frac{1}{G_n}\right) \qquad \text{(B.17)}$$

The capacitance of the p-i-n diode within the depletion approximation is calculated using the following equation.

$$C=\frac{\varepsilon A_D}{w_T} \qquad \text{(B.18)}$$

Where A_D is the area of the device under test.